On the origin of seismic signals recorded on Stromboli volcano

Dissertation

zur Erlangung des
naturwissenschaftlichen Doktorgrades
der Bayrischen Julius-Maximilians-Universität
Würzburg

vorgelegt von

Thomas Braun

aus Frankfurt am Main

Würzburg

November 2008

Eingereicht am: 17. November 2008

bei der Philosophischen Fakultät I für Geographische Wissenschaften

1. Gutachter der Dissertation:	Prof. Dr. Bernd Zimanowski
2. Gutachter der Dissertation:	Prof. Dr. Steve McNutt
1. Prüfer:	Prof. Dr. Bernd Zimanowski
2. Prüfer:	Prof. Dr. Ulrich Schüßler
Tag der mündlichen Prüfung:	21. Januar 2009

Zusammenfassung

Hauptaufgabe der Vulkanseismologie ist die qualitative and quantitative Beschreibung einer oder mehrerer unbekannter seismischer Quellen, die sich in einer unbekannten Tiefe unter dem Vulkan befinden. Auch wenn viele Vulkane der Erde ähnliche Signalcharakteristiken aufweisen, war es bis heute nicht möglich, für Vulkane ein seismisches Standard-Quellmodel zu finden, analog dem *double-couple* in der Erdbebenseismologie. Kontinuierlich tätige Vulkane, wie z.B. Stromboli (Italien), stellen für den Vulkanseismologen ein ideales natürliches Feldlabor dar, diese Fragestellung zu untersuchen.

Die vorliegende Arbeit untersucht auf Stromboli registrierte Explosionsbeben und vulkanischen Tremor in einem breiten Frequenzband und behandelt die Frage nach der Lage und dem Mechanismus der seismischen Quelle(n).

Seismische und Infraschallmessungen von strombolischen Explosionsbeben zeigen, dass sich eine Hochfrequenz-Phase mit einer Geschwindigkeit von etwa 330 m/s fortbewegt. Die seismische Quelle kann durch eine Explosion am oberen Ende der Magmasäule erklärt werden, die durch aufsteigende Gasblasen verursacht wird. Sowohl die seismische P-Welle, als auch die Luftwelle werden zum gleichen Zeitpunkt an ein und demselben Ort generiert. Die verschiedenen Laufwege und Geschwindigkeiten der seismischen und der Luftwelle resultieren in einem Laufzeitunterschied Δt, der zur Bestimmung des Magmenstandes und der Schallgeschwindigkeit in der Eruptionssäule im Schlotinnern genutzt werden kann.

In Kraternähe installierte Stationen zeigen, dass Infraschall- und seismische Messungen des kurzperiodischen Tremors ($> 1\ Hz$) den gleichen Frequenzgehalt und ähnliche Fluktuationen der seismischen Energie aufweisen. Daher wird der kurzperiodische vulkanische Tremor auf Stromboli durch das kontinuierliche Aufsteigen und Platzen kleiner Gasblasen im oberen Teil der Magmasäule verursacht.

Das Spektrum des auf Stromboli registrierten langperiodischen Tremors besteht hauptsächlich aus drei Maxima bei 4.8 s, 6 s und 10 s, deren Spektralamplitude mit der jeweiligen Wettersituation variieren. Sie werden daher nicht von einer lokalen vulkanischen Quelle erzeugt, sondern durch Meeresmikroseismik (MMS). Der Durchzug eines lokalen Tiefdruckgebietes scheint die Ursache für Spektralenergie bei 4.8 s and 10 s, die jeweils die *Doppelte* bzw. die *Primäre Frequenz* der MMS darstellen. Als Ursache des spektralen Maximums bei 6 s könnte ein Tief nahe der Britischen Inseln in Frage kommen.

Seismische Daten, die von dem ersten auf Stromboli installierten Breitband-Array registriert wurden, zeigten überraschend einfache Wellenformen, die einen anfänglich kontraktierenden Quellmechanismus anzeigen. Die Analyse der Partikelbewegung und die Anwendung seismischer Arraytechniken ermöglichten eine Lokalisierung der seismischen Quelle in Oberflächennähe.

Die Anwendung verschiedener Inversionsmethoden gestattete es, Eruptionsparameter und Charakteristiken der seismischen Quelle während der Strombolieruption am 5. April 2003 abzuschätzen. Als Ergebnis kann festgehalten werden, dass der paroxystische Ausbruch durch eine langsame Überschiebungsdislokation mit einer Momentenmagnitude von $M_w = 3.0$ verursacht wurde, ausgelöst durch einen vorher durch *Dike*-Intrusion verursachten Bruch. Während des Paroxysmus konnte in den seismischen Signalen mindestens eine *Blow-out* Phase mit einer Momentenmagnitude von $M_w = 3.7$ identifiziert werden. Diese kann durch einen vertikalen linearen Vektordipol, zwei schwächere horizontale lineare Dipole in entgegengesetzter Richtung, zuzüglich einer Vertikalkraft repräsentiert werden.

Seismische Messungen, die während kontrollierter und reproduzierbarer *Blow-out* Experimente unter Verwendung von einem in einer Basaltschmelze eingeschlossenen Gasvolumen durchgeführt wurden, ergaben folgende Ergebnisse: Monochromatische Signale sind Anzeiger für einen *Blow-out* in einem duktilen Regime, wohingegen ein breitbandigerer Frequenzgehalt auf einen Sprödbruch hinweist. Je grösser die Länge des Schmelztiegels ist, desto schwächer sind die seismischen Signale. Ein grösser Gasdruck bewirkt eine stärkere Fragmentation des Magmas, aber keine höhere Austrittsgeschwindigkeit des Magmapropfens und auch keine grössere seismische Amplitude. Auch wenn die langperiodischen Signale, wie beispielsweise Tilt, im Labor nicht simuliert werden konnten, sind die *Blow-out* Experimente überraschend gut in der Lage, die am Vulkan Stromboli registrierten kurzperiodischen seismischen Signale zu reproduzieren.

Abstract

The main purpose of volcano-seismology concerns the qualitative and quantitative description of one or more unknown seismic source(s) located at some unknown depth beneath a volcano. Even if many different volcanoes show similar seismic signal characteristics, up to now it was not possible to find a standard seismic source model for volcanoes, as the *double-couple* in earthquake seismology. Volcanoes with a continuous activity, like Stromboli (Italy), represent for the volcano seismologist a perfect natural laboratory to address this question.

This thesis treats the study of explosion-quakes and volcanic tremor recorded on Stromboli in a broadband frequency range, and discusses the location and the possible mechanisms of the seismic source(s).

Seismic and infrasonic recordings of explosion-quake from Stromboli showed that the high-frequency phase propagates with a velocity of approximately 330 m/s. The seismic source can be explained as an explosion at the top of the magma column generated by rising gas bubbles. The seismic P-wave and the air-wave are both generated in the same point at the same time. The different path lengths and velocities for the seismic wave and the air-wave result in a difference in arrival times Δt, that could be used to deduce the magma level and sound speed in the eruption column inside the conduit.

Stations installed near the active crater reveal that infrasonic and seismic recordings of the short-period tremor ($> 1\ Hz$) share the same spectral content and show similar energy fluctuations. Therefore, the short-period volcanic tremor at Stromboli originates from the continuous out-bursting of small gas bubbles in the upper part of the magmatic column.

The spectrum of the long-period tremor recorded at Stromboli consists of three main peaks with periods at 4.8 s, 6 s and 10 s, and amplitudes varying with the regional meteorological situation. Hence, they are not generated by a close volcanic source but rather by ocean microseisms (OMS). The passage of a local cyclone seems to be the seismic source for spectral energy at 4.8 s and 10 s, which represent the *Double Frequency* and the *Primary Frequency* of the OMS, respectively. Concerning the 6 s peak, a cyclone near the British Isles could act as a seismic source.

Seismic data from the first broadband array deployed on Stromboli showed surprisingly simple waveforms, indicating an initially contracting source mechanism. The analysis of particle motion and the application of seismic array techniques allowed the location of a seismic source in the shallow part of the volcano.

Eruption parameters and seismic source characteristics of the April 5, 2003 Stromboli eruption have been estimated using different inversion approaches. The paroxysm was triggered by a shallow slow thrust-faulting dislocation event with a moment magnitude of $M_w = 3.0$ and possibly associated with a crack that formed previously by dike extrusion. At least one blow-out phase during the paroxysmal explosion could be identified from seismic signals with an equivalent moment magnitude of $M_w = 3.7$. It can be represented by a vertical linear vector dipole and two weaker horizontal linear dipoles in opposite direction, plus a vertical force.

Seismic measurements performed during controlled and reproducible blow-out experiments with a gas volume entrapped in basaltic melt revealed the following: Monochromatic seismic signals suggest a blow-out in a more ductile regime, whereas broader frequency content indicates rupture in a more brittle environment. The longer the crucible, the weaker the seismic signals. An increase in pressure results in a stronger fragmentation, but not in a higher ejection velocity of the plug neither in a higher seismic amplitude. Even if the very long period observations like the tilt signal could not be simulated in the laboratory, the blow-out experiments simulate very well the short-period seismic signals recorded at Stromboli volcano.

Acknowledgements

Contents

List of Figures

List of Tables

Chapter 1

Motivation and overview

What does a seismologist do on a volcano, and why does (s)he do it? A volcano-seismologist installs seismic instruments on the volcano's flank and tries to infer from the registrations the physical process inside the volcano.

The original idea came from the Italian Scientists Luigi Palmieri and Giuseppe Mercalli. Palmieri recorded continuous tremor on Mt. Vesuvius before the 1861 eruption by a self constructed electromagnetic seismograph, and in 1907 Mercalli observed at Stromboli volcano ripples on the surface of a Mercury vessel, some seconds before a typical strombolian eruption (*Sieberg* (1914)).

Once the existence of the physical phenomenon was discovered, the developments in seismometry and the successful application of seismological methods to volcanoes inspired seismologists to carry their portable instruments to the active volcanoes of the world. Its sensitivity and its easy handling made the seismometer the perfect instrument to monitor and forecast volcanic eruptions.

Chapter 1.1 summarizes the history of volcano seismology up to the end of the 1980s. Section 1.2 continues the description of the rapid development of volcano seismology from the 1990s on. Exactly at this *historical moment* the first contributions for the present thesis have been collected. *Historical moment*, because at that time portable broadband seismometers became available and digital 24 *bit* data acquisition became standard. Because of this, data quality improved significantly and allowed to improve also the existing source models.

1.1   Volcano seismology until the nineties

Omori (1911) reported pulsatory oscillations and earthquakes associated with the eruptive activity of Asama-yama volcano (Japan) in the years 1911 – 1912. *Sassa* (1935) published a micro-seismometric study on Aso volcano (Japan) and proposed as source model the opening-closing mode of a fluid filled crack. *Imbò* (1945) reported seismic signals during the Vesuvius eruption of 1944. *Omer* (1950) proposed a tremor model, where he attributed the tremor to the quasi free vibration of solid

1

layers forming the shallow part of the volcano. Finally, *Minakami* (1960) published the first classification of seismic signals (A/B-type event).
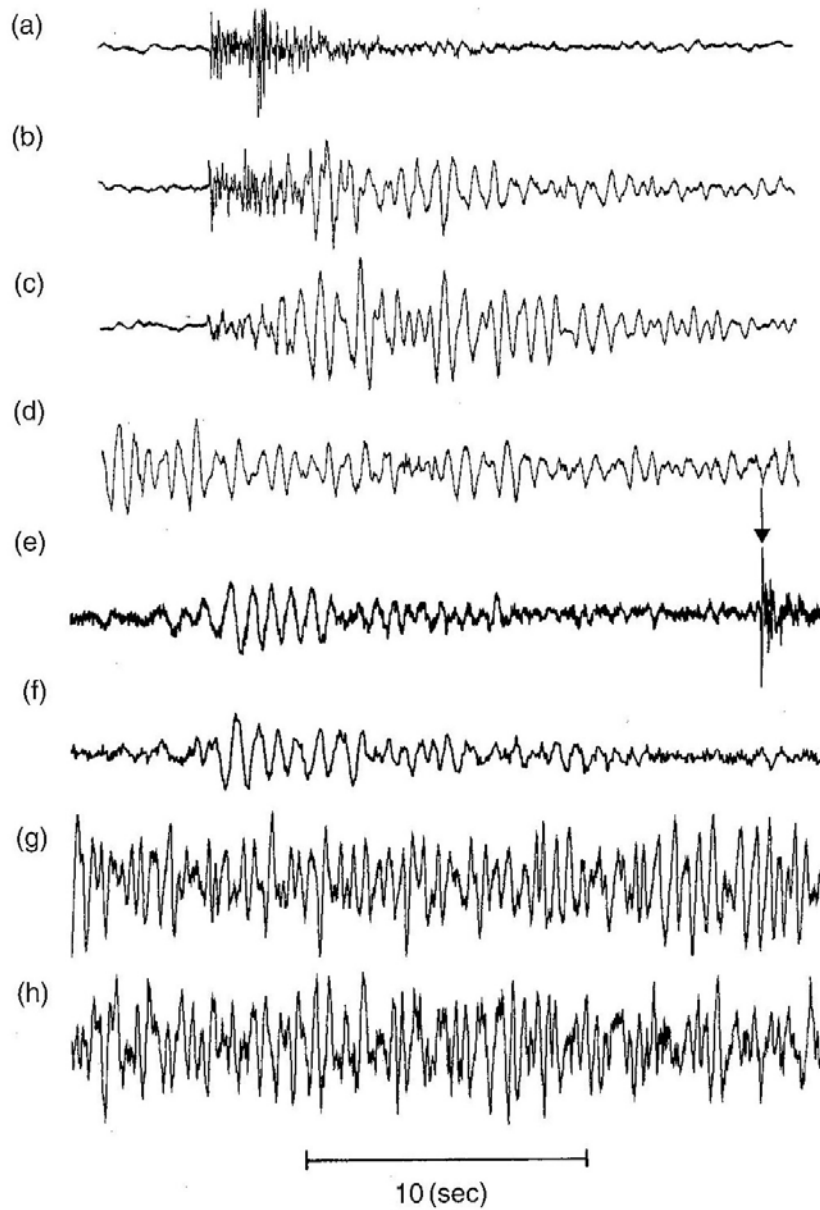
Figure 1.1: *Classification of volcano-seismic signals after McNutt (2002). (a) high-frequency event, (b) hybrid event, (c) low-frequency event, (d,g,h) volcanic tremor, (e) explosion-quake + air wave, (f) explosion-quake without air-wave.*

Concerning the origin of volcanic tremor, *Schick and Riuscetti* (1973) interpreted the relatively stable frequency peaks in the continuous seismic signals as resonating frequencies of the conduits, and derived a model for the geometry of the magma feeding system. For Stromboli it was first *Fadeli* (1984), and later *Mohnen and Schick* (1996), who derived the conduit geometry from the short-period volcanic tremor.

One of the interesting features of volcanic seismic recordings was that signals like tremor or low-frequency events showed similar characteristics for many volcanoes *all over the world*. *McNutt* (2002) summarized some exemplary signal characteristics (figure 1.1). This inspired volcanologists to propose the following models for a common seismic source model. Some of them are listed below:

- solid – solid: opening of tensile/shear cracks (*Schick* (1981))

- fluid – solid: unsteady fluid flow in conduits (*Koyanagi et al.* (1987); *Ferrick et al.* (1982)); opening and vibration of tensile fluid filled cracks (*Sassa* (1935); *Aki et al.* (1977); *Chouet* (1988))

- fluid – gas – solid: eigenvibration of magma and gas filled chamber (*Crosson and Bame* (1985)); self sustained feed back pressure fluctuations (*Steinberg and Steinberg* (1975); modified by *Schick* (1988))

- two phase flow: the flow velocity of the magma exceeds the sound speed of the magma-gas mixture *Martinelli* (1991)

While the debate about the physical model of volcanic tremor remains an open question, the envelope of the volcanic tremor's amplitude (RMS) has become an important indicator used to successfully forecast eruptions, as e.g. in the case of the large Pinatubo eruption in 1991 (*PVOT - Pinatubo Volcano Observatory Team* (1991)).

1.2   Introduction to the present work

The main question in volcano-seismology concerns the qualitative and quantitative description of the source that radiates seismic energy during volcanic explosions. Many ideas have been proposed in the past (chapter 1.1), but up to now it was not possible to find a standard model, similar to the *double-couple* in earthquake seismology. Solutions for this problem can be approached, if the number of parameters describing the complexity of volcano-seismic recordings are reduced, and contributions of source, path, site and instrument effect, are separated.

Two main approaches were followed to address this deconvolution problem: (i) reduction of the recording distance and (ii) extension of the recording frequency band to lower frequencies.
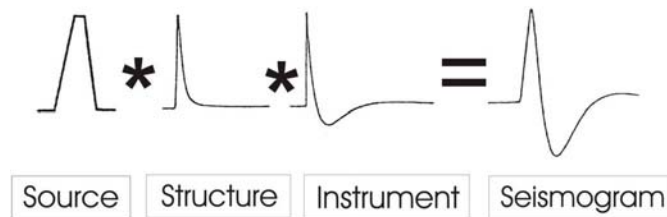
Figure 1.2: *Separation of source, path, site, instrument effect.*

Volcanoes like Stromboli represent a perfect natural laboratory for studying the volcanic seismicity and for modelling its explosion dynamics. Its continuous and persistent *strombolian activity* with relatively frequent summit explosions (every 15 – 30 min) and the easy access to the active craters makes Stromboli the perfect *playground* for volcanologist from all over the world.

The present thesis represents the result of many years of continuous study of the volcano-seismic signals recorded at Stromboli. The first measurements have been collected at the beginning of the 1990s, exactly when a new era of volcano seismology started. Except for chapters 1, 6 and 9, this thesis is a compendium of reviewed papers, published in international scientific journals:

- chapter 2: T. Braun & M. Ripepe (1993)

- chapter 3: M. Ripepe & T. Braun (1994)

- chapter 4: M. Ripepe, P. Poggi, T. Braun & E. I. Gordeev (1996)

- chapter 5: T. Braun, J. Neuberg & M. Ripepe (1996)

- chapter 7: J. Neuberg, R. Luckett, M. Ripepe & T. Braun (1994)

- chapter 8: S. Cesca, T. Braun, E. Tessmer & T. Dahm (2007)

The following tries to summarize briefly the chronology of the most important campaigns at Stromboli and their results.

The first contribution for the present thesis comes from the first near-field measurements, performed in 1991. This allowed the first time, to distinguish discrete phases in the strombolian seismograms: the P-phase and a second air-wave phase (*Braun and Ripepe* (1993), chapter 2). Distinct air-phases had already been recognized in explosion-quake seismograms from other volcanoes, e.g. Pavlof volcano/Alaska (*McNutt* (1986)). With respect to Stromboli, on Pavlof volcano the recording distances are larger, facilitating the discrimination of the air-phase. Possible derivations for volcanic activity parameters from this observation were discussed in *Ripepe and Braun* (1994) (chapter 3). To better study the air-wave,

we installed an infrasonic network and discovered that the short-period volcanic tremor at Stromboli volcano originates from continuous out-bursting of small gas bubbles in the upper part of the magmatic column (*Ripepe et al.* (1996)) (chapter 4). In the same period *Kedar et al.* (1996) reported similar observations from Old Faithful Geyser and *Benoit and McNutt* (1997) and *Hagerty et al.* (1997) assumed that gas bubble ascent is responsible for the harmonic volcanic tremor recorded on Arenal volcano (Costa Rica).

In 1992 *Brüstle et al.* (1993) installed the first STS-2 seismometer at 1900 m distance from the crater and reported low-frequency seismic observations of explosion-quakes for the first time. *Dreier et al.* (1994) used this data and stacked similar seismograms to distinguish two different fundamental types of seismograms, possibly generated by different craters.

In this period, the first array measurements were realized at Stromboli volcano. After the installation of a short-period seismic array in May 1992, consisting of 180 seismometers (*Chouet et al.* (1998a)), *Neuberg et al.* (1994) installed in November 1992 the first seismic broadband array, using two different configurations. This led to new findings on the origin of the long-period volcanic tremor (*Braun et al.* (1996)) (chapter 5), that have been further studied in chapter 6 by using additional seismic, meteorological and mareographic data.

Concerning the origin of explosion-quakes on Stromboli, it was the first broad-band array installation on Stromboli volcano (*Neuberg et al.* (1994)) that provided new insights of the dynamics of explosion-quakes and constrained the source location in the upper part of the volcano (chapter 7). *Wassermann* (1997) used seismic data from a 4 km aperture array installation on Stromboli and applied beam-forming on diffraction hyperboloids to locate explosion-quakes. He confirmed the shallow source location ranging from $0.2 - 0.7$ km above sea level. *Saccorotti et al.* (1998) applied a method based on the Bayesian inversion of the slowness vector and estimated the source region to be located between $100 - 300$ m below the craters. *Chouet et al.* (1998a) and *Chouet et al.* (1998b) used data from a short-period seismic array and determined the source region of volcanic tremor and explosion-quakes at a depth shallower than 200 m, with occasional bursts of energy originating from sources extending to a depth of 3 km.

Chouet et al. (2003) estimated the source mechanisms of explosions at Stromboli volcano from moment-tensor inversion (MTI) of very-long-period data. *Auger et al.* (2006) applied the MTI-algorithm for a real-time monitoring of Stromboli by an automatic inversion of source parameters of very long-period seismic signals. On April 5, 2003 a paroxysmal eruption occurred on Stromboli volcano, the largest one since the September 11, 1930 eruption. It is one of the rare cases worldwide, where a large volcanic explosion was recorded by near-field seismic broadband recordings. Chapter 8 describes for the first time, the estimation of the eruption parameters and the seismic source characteristics of a paroxysm, applying different inversion approaches (*Cesca et al.* (2007)).

Chapter 9 describes a completely different approach, i.e. the realization of laboratory experiments for the simulation of strombolian eruptions. The study of gas slug ascent in an equivalent *cold* fluid with known physical parameters was already performed by *Jaupart and Vergniolle* (1988), *Jaupart and Vergniolle* (1989), *Seyfried and Freundt* (2000), *Ripepe et al.* (2001) and *James et al.* (2006). The new approach presented here was to perform laboratory experiments on the fragmentation and expansion of magmatic melt using volcanic rock at magmatic temperatures.

To complete the picture it may be noted that two further papers have been published, that have not been included in the present thesis, namely: (i) Ocean bottom seismometers deployed in Tyrrhenian Sea, by *Dahm et al.* (2002), which reports interesting seismic recording with tremor-like signal characteristics, and (ii) a contribution in German, by *Braun and Ripepe* (1995), which summarizes the most important results of *Braun and Ripepe* (1993), *Ripepe and Braun* (1994) and *Ripepe et al.* (1996).

Chapter 2

Interaction of seismic and air-waves 1

Abstract   Explosion-quake seismograms recorded at Stromboli show that seismic phases with a high-amplitude and high-frequency content propagate with a velocity of approximately 330 m/s – the sound speed. The analysis of seismograms, recorded at a distance of 500 m from one of the three active vents, shows for the first onset a low-frequency and a particle motion characteristic of a p-wave, which loses its longitudinal polarization with the onset of the air-wave. Recording the explosion-quakes simultaneously with a microphone we could ascertain that the high-frequency onset coincided with the airwave's. In order to better understand the seismic wave field generated by the atmospheric pressure, we performed a controlled source experiment at Stromboli using a seismic gun. Seismograms with the same two phases and particle motions comparable with the volcano-seismic data were obtained. A second experiment demonstrated, that the air-wave propagates at least in the upper 1 m of the ground. We suggest that the seismic source of the corresponding seismograms is an explosion at the top of the magma column and conclude that the p- and air-waves are both generated in the same point at the same time.

2.1 Introduction

One of the main characteristics of Stromboli volcano (Sicily) is its continual explosive activity with lava fountains up to 250 m, which can be visually observed from the summit. The persistence of the "Strombolian activity" provides a large amount of data enabling volcanic activity to be carefully studied from a seismic point of view.
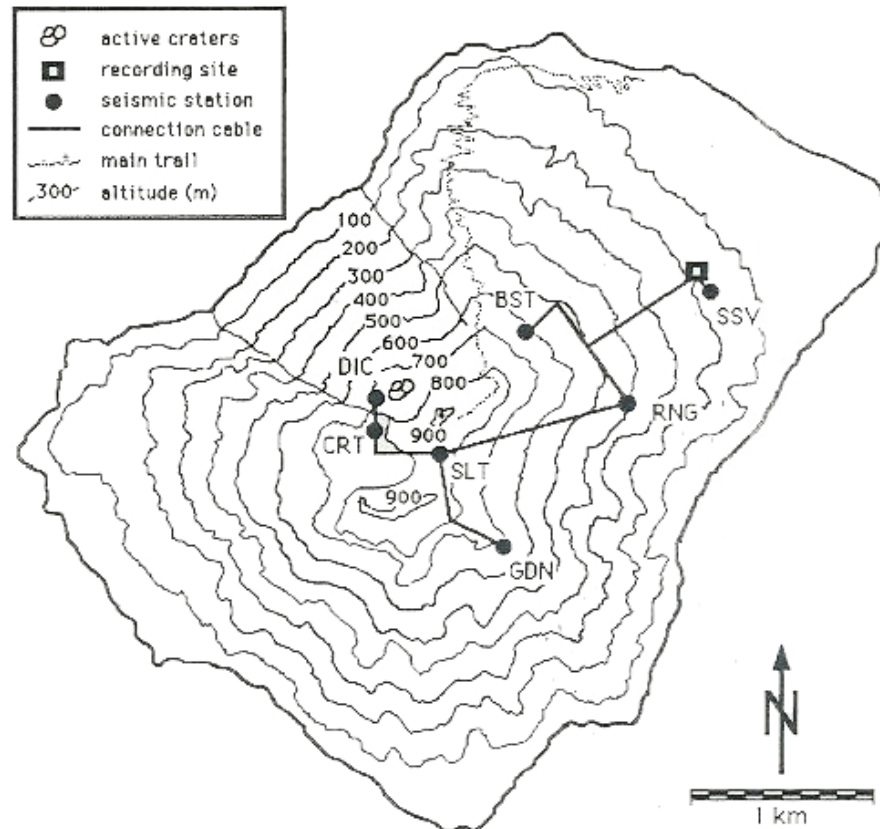
Figure 2.1: *Sketch map of the seismic network installed at Stromboli.*

The Department of Earth Sciences of the University of Florence has been running a permanent seismic network on Stromboli since 1989, consisting of six stations equipped with short-period seismometers (Mark-L4, 1 Hz), one of which (SLT) is a 3-component station (Figure 2.1). Besides, seismic surveys were temporarily carried out at Stromboli, as those by *Del Pezzo et al.* (1974), *Lo Bascio et al.* (1973), *Ntepe and Dorel* (1990), *Schick* (1981). Altogether, three different types of explosion quakes have been distinguished at Stromboli: low-frequency events (1 − 2 Hz), high-frequency events (> 5 Hz), and a third mixed type which shows a high-frequency signal following a low-frequency phase. The similarity be-

tween the spectral content of the volcanic tremor and the low frequency part in the explosion-quake seismograms has led previous investigators (*Lo Bascio et al.* (1973)) to interpret the low-frequency signal as due to magma oscillations in the volcanic conduit, whereas the signals with a high-frequency content of $5-8\ Hz$ have been related to the explosive dynamics (*Ntepe and Dorel* (1990)).

Our results differ substantially from this interpretation, which relates the two phases to different dynamical processes. We actually propose new results to clarify the nature of the observed mixed-type seismic signals: the low-frequency phases are of different physical nature, but are generated at the same instant by the same source mechanism.

2.2   Analysis of explosion-quake seismograms

In order to define the depth of the explosions, an additional vertical seismometer (DIC, Figure 2.1) was placed as close as $70\ m$ from the rim of one of the major active vents at Stromboli, inside the *Torrione Crater*. The recordings lasted only
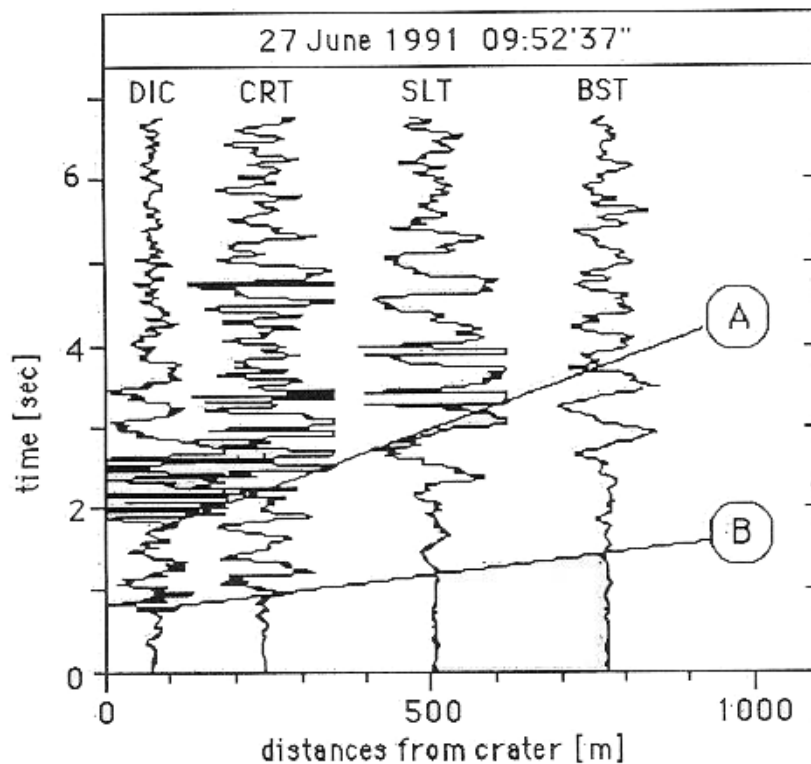
Figure 2.2: *Seismograms of an explosion-quake that occurred in the Torrione crater. The low-frequency phase (B) can be clearly observed up to a distance of 800 m.*

one day, because a sudden increase of the explosivity destroyed part of the connection cables. Nevertheless, more than 200 very peculiar seismograms were recorded. Figure 2.2 shows one of these typical seismograms produced by explosions inside the Torrione Crater. Many seismic signals were characterized by a first weak phase (A) and a clear, strong second phase (B) with higher frequency.

These seismic signals with a high-frequency second phase can be clearly observed not only near the craters, but also over the whole network (Figure 2.3). The amplitude of the high-frequency phase decays rapidly with distance from the source.
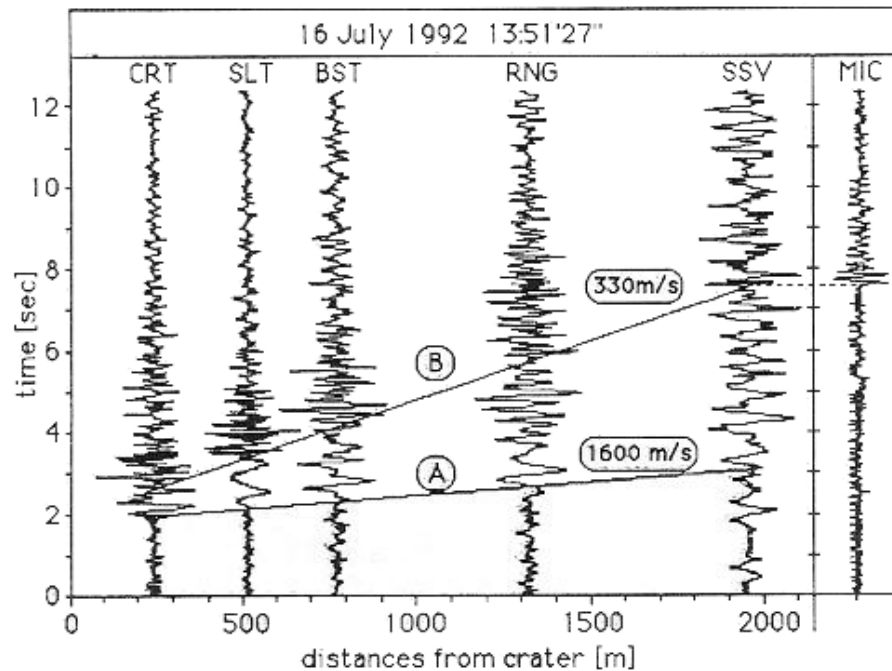
Figure 2.3: *Seismograms and pressure signal (MIC) of an explosion-quake that occurred in the Torrione crater. The group velocity of the high-frequency onsets (B) is approximately 330 m/s; the apparent velocity of the first arrivals (A) is 1600 m/s. The onset of the volcanic air-wave (MIC), recorded at a distance of 1950 m, coincides clearly with the high frequency onset of the correspondent seismogram (SSV).*

To understand the seismic nature of the low- and high-frequency phase, the particle motion was reconstructed for several explosion-quake seismograms recorded at the 3-component station SLT. Figure 2.4 shows a close-up of the first part of one of these explosion quakes. Window A outlines the first onset of the seismogram and shows a clear longitudinal polarization in the N-E and Z-R planes, away from the crater. This behaviour has been interpreted as typical for a p-wave which is

produced by an explosive shock. Window B outlines the second onset: the directional character of the particle motion is lost and became chaotic in the N-E and Z-R planes.
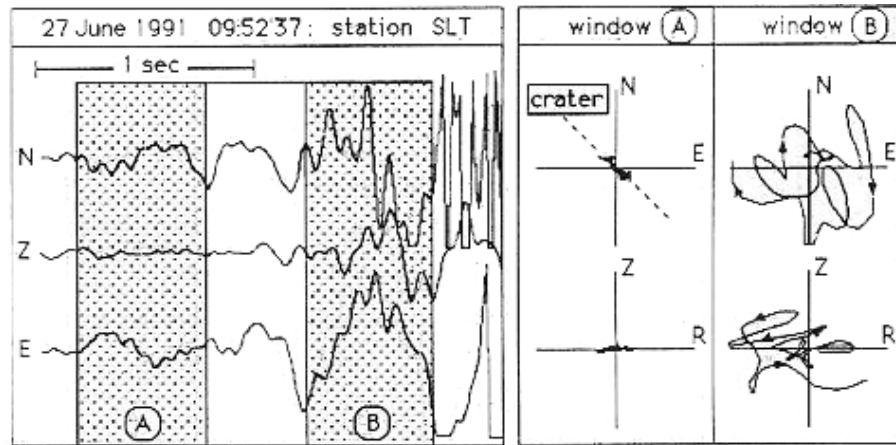
Figure 2.4: *Seismograms (left) and particle motion plots (right) of the explosion-quake in Figure 2.2. The low-frequency part (window A) shows a clear longitudinal polarization towards the active Torrione Crater, whereas the particle motion becomes chaotic with the onset of the air-wave (window B).*

In order to study the propagation of such waves, a travel-time representation was used. It is well known that the main problem in building up travel-time graphs is the determination of the focus-to-station distance. This problem was solved by two separate considerations: first, we used only those seismometers which were produced by the visually observed volcanic explosions. In this way the distances were estimated with a precision of 30 m. The second consideration concerns the hypocentral source position, which is located in 90% of the cases in the uppermost portion of the magmatic conduits (*Ntepe and Dorel* (1990); *Del Pezzo et al.* (1974), at an elevation between 650 m and 700 m *Mariotti* (1978)). Therefore we calculated the focus-to-station distances measured along the scope of the volcano.

The analysis of several explosion-quakes with well known foci shows that the two clearly evident phases in the seismograms were travelling with apparent velocities of respectively 1600 m/s (A in Figure 2.3) and 330 m/s (B in Figure 2.3). We conclude, that the second phase with a velocity of 330 m/s is the air-wave produced by the explosion and detected by the seismometers as a high-frequency signal. This interpretation is confirmed by the registration of the volcanic air-wave with an independent non-seismic method. The explosion-quakes were simultaneously recorded by the seismic network and by a non-dynamic microphone with a very low-frequency response (from 0.1 Hz to 15 Hz). The sensor was installed

inside the *Semaforo San Vincenzo* recording site near the stations SSV (Figure 2.1), at a distance of 1950 m from the craters.

In Figure 2.3 the pressure signal (MIC) is plotted beside the seismogram of station SSV in order to compare the arrival times of both recordings. Figure 2.3 clearly shows that the air-wave onset in the pressure signal coincides exactly with the high-frequency onset in the SSV seismogram. This result confirms the high-frequency phase in strombolian explosion-quake seismograms as being due to an atmospheric pressure signal, generated by the volcanic explosion.

2.3   Seismic gun experiments

The way the air-wave propagates into the ground is not completely clear; very few studies have concentrated on this, as that by *Press and Oliver* (1955). Therefore, in order to get more experience on the mode of propagation of the air-wave and its interaction with the seismic signals recorded in the near-field, we carried out two simple experiments near the recording site at Stromboli (Figure 2.1). We generated artificial explosions with a small seismic gun, normally used in seismic prospecting. Each explosion was recorded by two 3-component stations at different distances from the shot-point, using the same seismometer type (Mark L4) and the same acquisition system operating for the Stromboli network. The shots were set at different distances and the origin times were measured by an additional seismometer placed close to the shot-points. The waveforms recorded were comparable to those of the volcanic explosions. After the p-wave onset, a phase with higher amplitude was recorded. Unlike the natural phenomenon, a sharp difference in terms of frequency is not clearly detectable. This behaviour appears to be reasonable when we consider the nature of the two different sources: volcanic activity generates seismic signals within a low-frequency band, while seismic guns are known to be a high frequency seismic source.

The group velocity of 330 m/s confirms the air-wave nature of the second onset in the seismogram, a well known phenomenon in seismic prospecting. The particle motion, produced by the air-wave and recorded at a distance of 100 m from the shot-point, was reconstructed in order to compare it with the ground motion of the explosion-quakes (Figure 2.5). After a p-wave longitudinal polarization towards the source (Window A), the air-wave onset produces an apparent chaotic pattern (Window B). In the horizontal plane (N-E), the particle motion describes ellipses typical of Love type surface waves, and in the meantime the movement becomes retrograde elliptic in the vertical plane (Z-R) – typical of Rayleigh waves.

The second experiment was carried out in order to verify how the air-wave propagates in the geological media, and whether the latter introduce some distortion in the signal recorded by the seismometers. The experiment was performed by recording a gunshot with three vertical seismometers dug in a depth of 1 m,
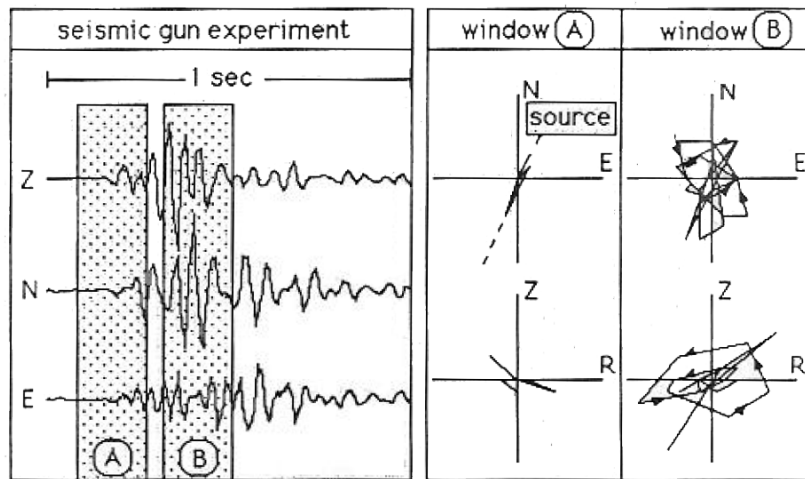
Figure 2.5: *Seismograms (left) and particle motion plots (right) of a seismic gun experiment. After the arrival of the longitudinally polarized p-wave (window A), the polarization is lost with the air-wave onset (window B).*

0.3 m, and eventually on the free surface. The shot-point was at a distance of 190 m. The records for the three vertical seismometers with the same gain-factors showed amplitudes and waveforms very well correlated for the various depths. Thus indicating that the air-waves propagates, at least in the uppermost metre of the ground, with the same group velocity as in the air. We conclude that the sound pulse produced by the volcanic explosion travels in the air and pushes on the ground as it travels. The small contrast of acoustic impedance between the air and the soft volcanic ground favours a strong energy transmission. Besides, strong seismic energy absorption of the soft pyroclastic material prevents formation of a new faster wave field inside the ground. The combination of these two factors is a surface wave that apparently travels into the ground with the air-wave velocity.

2.4   Discussion and conclusions

Distinct air-pressure signals generated by volcanic activity have already been observed by author authors (*McNutt* (1986); *Okada et al.* (1990); *Yuan et al.* (1984)). At Stromboli volcano the occurrence of a high-frequency phase after a low-frequency first onset has often been described, but never interpreted as air-wave phase. As already mentioned these two phases have always been related to different dynamical processes. The similar spectral content of tremor and explosion-quakes induced *Ntepe and Dorel* (1990) to interpret the 2 Hz and 6 Hz first and second phases in the explosion-quakes as being caused by two distinct

oscillation modes of the system. In addition they assumed the model of *Jaupart and Vergniolle* (1988), concluding that the low-frequency part of the seismogram could be due to the collapse of a foam layer, exciting the magma chamber, whereas the high-frequency phase could be related to the excitation of the terminal conduit by the explosion of a slug. *Lo Bascio et al.* (1973) interpreted the initial low-frequency phase as due to magma oscillations caused by rapid volume changes and the following high-frequency phase as being related to vibrations of the vent walls during ejections.

In contrast to these possible interpretations, we believe, that the two phases are of different nature but generated at the same time and related to one single mechanism. The nature of the high frequency signal is undoubtly confirmed as an air-pressure wave by the microphone recordings. In order to support this hypothesis we reproduced – by means of artificial explosions – waveforms with evidence of the same two phases as in the natural phenomena.

Therefore we suggest that the correspondent volcano-seismic source is an explosion at the top of the magma column, generated by rising gas bubbles reaching the magma surface. At the explosion instant, energy is emitted partly in the solid ground as seismic waves, and partly in the air as a pressure wave. This air-wave can be clearly observed only if the explosive source mechanism is short and impulsive, as that generated by a single gas bubble. If the explosions are produced by more complex source-functions, such as a consecution of rising gas bubbles, the seismic signals show a high-frequency content (*Ripepe et al.* (1993)) and the air-wave onset is hidden in the more complex wave package. The seismic waves travel to the seismograph through the ground; the air-waves runs up the vent first and then above the surface to the instrument, and thus its path is longer. The different path lengths in addition to the different wave velocities of p- and air-wave could explain the large time differences Δt between both phases we observed, even at the nearest stations to the crater (Figure 2.6). The time delay Δt is not steady in time, but varies rapidly from 0.25 s to 2.4 s. If we assume the source mechanism described above, Δt could be used as an indicator for the level of the magma column in the conduit: the deeper the magma surface, the larger the difference between the p- and air-wave paths and consequently the larger the amount of Δt. The level of the magma surface calculated on this basis resulted very deep – up to 700 m under the crater terrace. This result, together with the rapid change of Δt, appears as not reliable.

Additional parameters should be taken into account, as being responsible for the Δt-variation: the sound speed in a two phase flow is not only a function of temperature and pressure, but also depends on the amount of gas and on the radius of the gas bubbles (*Kieffer* (1977)). A slight increase in the percentage of gas in the magma-gas mixture reduces the sound speed drastically. Assuming lower values for the sound speed inside the conduit (down to 70 m/s), the variation of Δt leads to small fluctuations of a shallow source, in agreement with the hypocentral
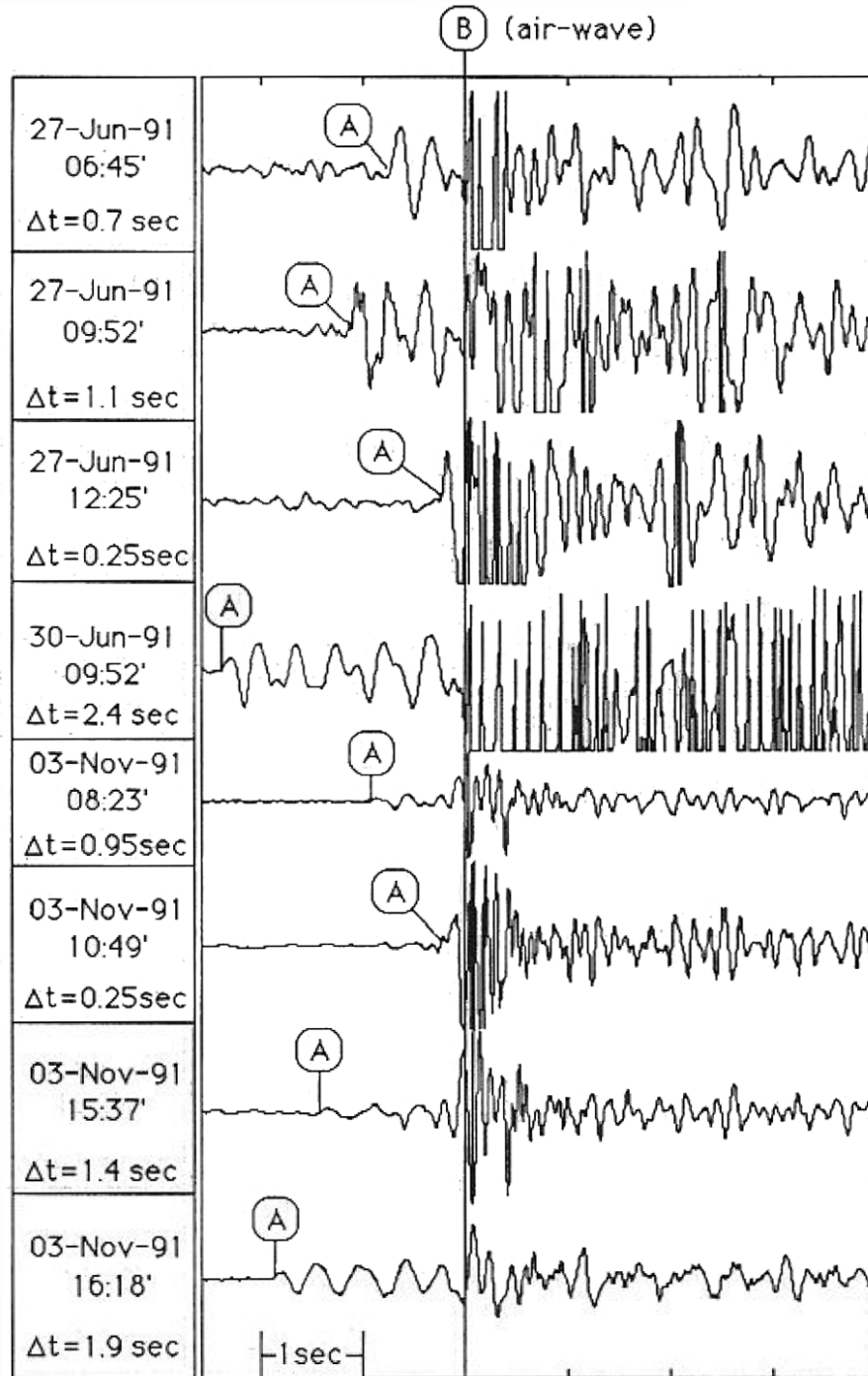
Figure 2.6: *Examples of the variability of the delay time Δt between the p-wave (A) and the air-wave (B), as recorded at the CRT vertical station (Figure 2.1).*

determinations.

However, if we consider the magma level to be stable, at least for a short period of time (one day), the drastic fluctuations of Δt would reflect the variations of the sound speed inside the conduit. According to this, Δt could provide important information on the amount of gas involved in the explosive process. Nevertheless the interpretation of the variation of Δt is still subject to speculation and requires further investigations.

Chapter 3

Interaction of seismic and air-waves 2

Abstract   Many explosion-quake seismograms recorded near the active craters at Stromboli are dominated by two distinct onsets: a first low-frequency phase and a second high-frequency one. Particle-motion diagrams show a P-wave characteristic for the low-frequency-phase, whereas in the high-frequency onset the longitudinal polarization is lost and the pattern becomes chaotic in the horizontal as well as in the vertical plane. The air-pressure pulse generated by the volcanic explosion is detected by the seismometer as a high-frequency signal, and we assume as source mechanism an explosion at the top of the magma column, generated by rising gas bubbles. The different path lengths and velocities for the seismic wave and the air-wave are the reasons for the difference in arrival times Δt between the low-frequency and the high-frequency onset. We tried to deduce the magma level and gas velocity in the conduit, from observed Δt values. If the velocity of the pressure pulse inside the conduit is assumed to be lower $(30 - 70\ m/s)$ than the sound speed, the magma level remains reasonable stable, even for large changes of Δt.

3.1   Introduction

One of the main interests in volcanology is to understand the internal physical process that generates seismic waves from a seismological point of view.   This

purpose has induced scientists to classify their seismograms according to different signal characteristics (*Sassa* (1935); *Minakami* (1960); *Schick* (1981); *Okada et al.* (1990)). Since these characteristics depend on a multitude of factors, e.g. the state of the activity of the volcano, the viscosity of the magma, the percentage of gas involved in the explosion, and many others, it has not been possible to merge the interpretations of these features in a general model until today.

The volcanic activity of Stromboli (Sicily) has the peculiarity of being in a persistent explosive phase and its seismic activity is generally dominated by transient signals with an emergent onset and a duration shorter than 30 *s*. Since most of these signals can be associated with the visible volcanic explosions (*Del Pezzo et al.* (1974); *Mariotti* (1978); *Fadeli* (1984); *Schick and Müller* (1988); *Ntepe and Dorel* (1990)), these events are often called "explosion quakes".

One attempt to recognize the number of different dynamical processes is by grouping together seismic signals into "families" with a similiar form. In terms of internal dynamics, several classifications for the strombolian explosion-quakes have been proposed (*Cardaci and Lombardo* (1988); *Falsaperla and Pellegrino* (1988); *Falsaperla et al.* (1989); *Lo Bascio et al.* (1973); *Ntepe and Dorel* (1990)). These classifications are based on the frequency content of the seismic signals. Generally three different types of signals of volcanic shocks have been distinguished in the seismograms: low-frequency events ($1-3\ Hz$), high-frequency events ($5-10\ Hz$) and signals with a first low-frequency onset followed by a high frequency phase.

In this paper we present new interpretations of characteristic features in explosion-quake seismograms recorded at Stromboli, that could be interesting if extended to other volcanoes showing strombolian activity. From this new evidence we speculate on the explosive dynamics and physical characteristics of the source.

3.2 Data acquisition

The Department of Earth Sciences of the University of Florence (DESUF) has been running a permanent seismic network on Stromboli since 1989 (*Napoleone et al.* (1993)). The network consists of short-period seismic stations (Mark-L4, 1 Hz), which are connected via cable to the recording site Semaforo San Vincenzo (fig. 3.1). The software program *MicroNet*, developed at the DESUF and installed on a MacIntosh II computer, manages the recordings of up to 16 channels. Since the main interests of the DESUF are the transient strombolian events, *MicroNet* generally operates as an amplitude trigger system, but the acquisition system can be also set in continuous recording mode. The sampling rate is 100 Hz, with an antialising filter at 25 Hz, while amplifications vary between 40 dB to 80 dB, depending on the distance from the craters. Since July 1990, five vertical seismometers (SSV, CRT, BST, GDN, RNG) and one 3-component station (SLT) have been recording volcano-seismic signals (fig. 3.1).
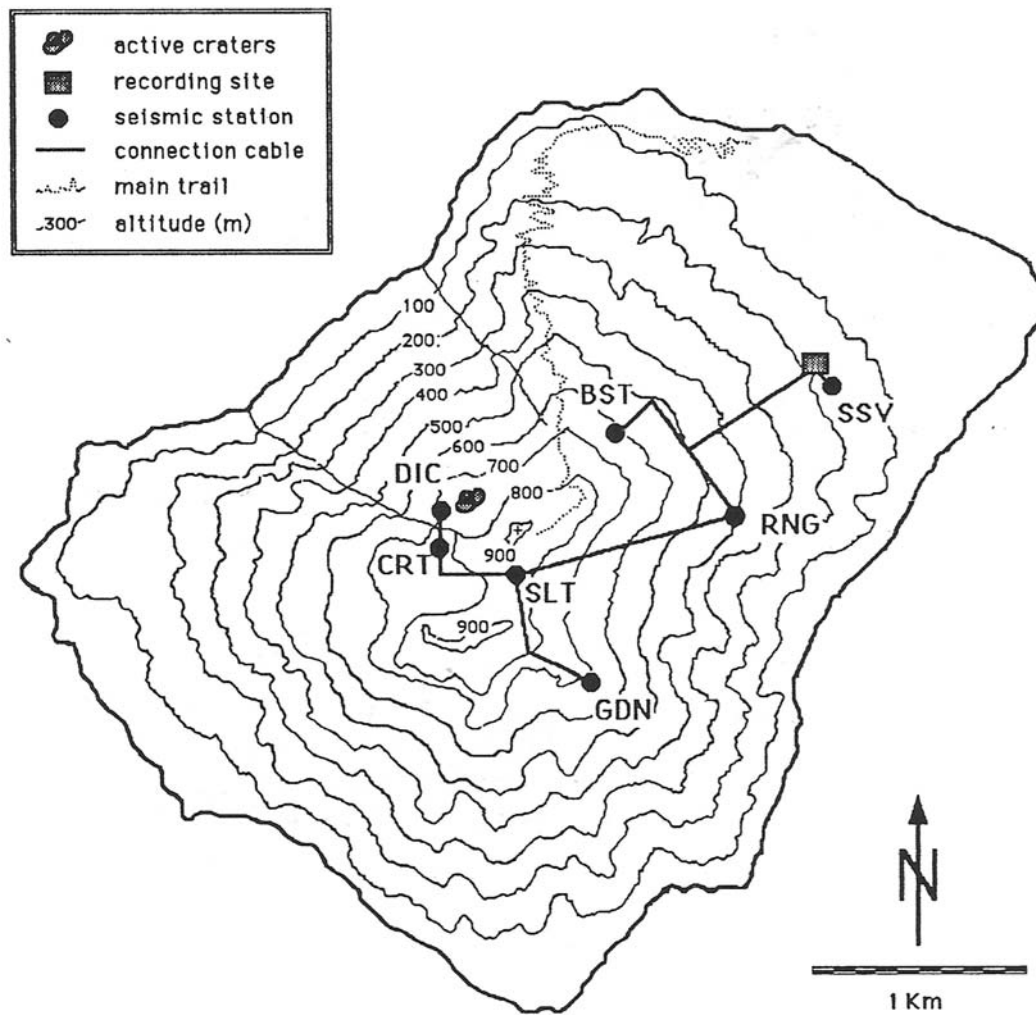
Figure 3.1: *Sketch map of Stromboli and the seismic network of the University of Florence.*

The network has been made flexible enough to allow experiments and to be easily set in new configurations. The data we present have been collected during two experiments in June 1991, and May 1992, when we installed a pressure sensor near the crater.

3.3   Explosion-quake seismograms

As introduced above, a clear correlation of the various explosive dynamics with different volcano-seismic signals at Stromboli, could not be realized today. In order to have an idea of the possible explosive mechanisms, the explosion-quakes have been classified in three types, according to their frequency content: low-frequency (fig. 3.2a), high-frequency (fig. 3.2b), and mixed-type (fig. 3.2c). The efforts to correlate these different types to visible explosions have not been successful over a long time interval.
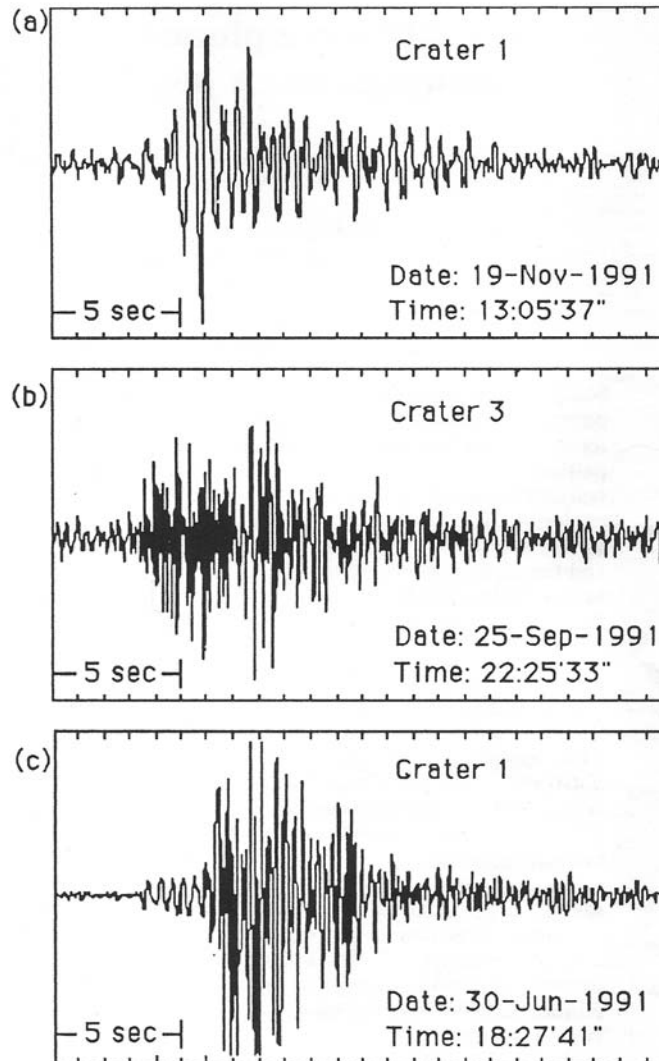
Figure 3.2: *Different types of explosion-quake seismograms: (a) low-frequency event, (b) high-frequency event, (c) mixed-type event*

Nevertheless, with non-seismic measurements, like the image processing of infrared pictures (*Ripepe et al.* (1993)), a correlation between the source dynamics and the seismic signal could be found. Large amount of ejected mass can be correlated to seismic signals with low spectral amplitude and high frequency content, whereas explosions with smaller mass quantity are characterized by higher spectral amplitudes and lower frequency content. If we figure the volcanic structure as an open system, it seems evident, that the source radiates the energy in the ground as seismic waves and in the air as kinetic energy of the explosion.

Moreover, by using multichannel recordings of the seismic network, we noticed that the interpretation of the volcano-seismic source by seismograms depends particularly on the distance from the vent, even on a small volcano like Stromboli (fig. 3.3). The influence of the propagation medium on the waveform seems to be very strong. In order to reduce the path effect, we installed a vertical seismic station (DIC) close to the *Torrione crater* at a distance of 70 m. This station lasted only for one day, because a sudden change in the volcanic activity damaged most of the connection cables. Nevertheless, almost 200 events were recorded and in many of them we noticed a very sharp high-frequency phase after an emergent onset (fig. 3.4).
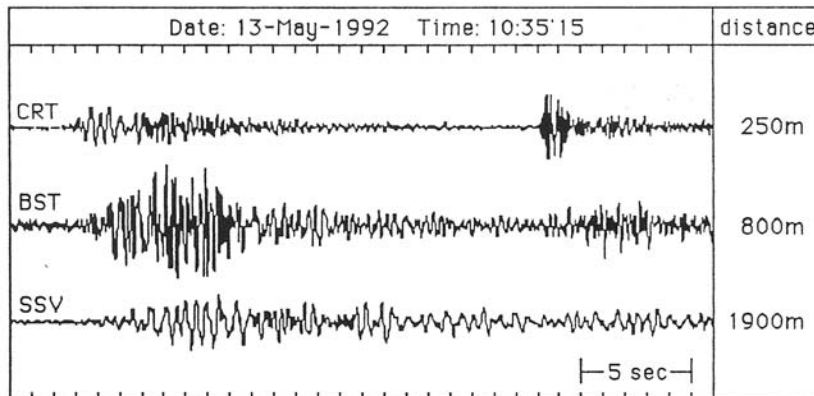
Figure 3.3: *Seismogram of an explosion-quake recorded at different distances. While at a distance of 250 m from the vent (CRT) a "mixed-type event" is followed after about 20 s by a "high-frequency event", this distinction becomes more difficult at increasing recording distances (BST, SSV). The seismogram of station SSV (1900 m from the vent) shows only one event with a "low-frequency event".*

On a travel-time representation of the seismic signals, we determined the velocities for the two dominant phases: 1600 m/s for the first low-frequency onset and 330 m/s – the sound speed – for the second high-frequency phase (fig. 3.5). The particle motion at station SLT (500 m from the vent) shows for the low-frequency

part of the seismogram a longitudinal polarization towards the crater (fig. 3.6, window A), while for the high-frequency onset the motion becomes chaotic (fig. 3.6, window B).
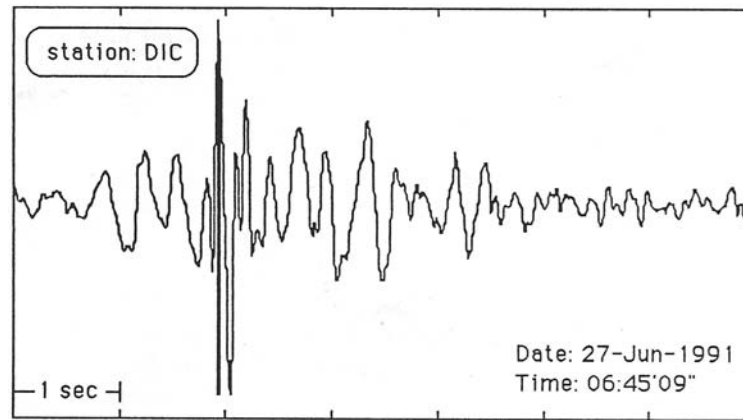
Figure 3.4: *Explosion-quake seismogram recorded at station DIC (distance of 70m from the vent).*
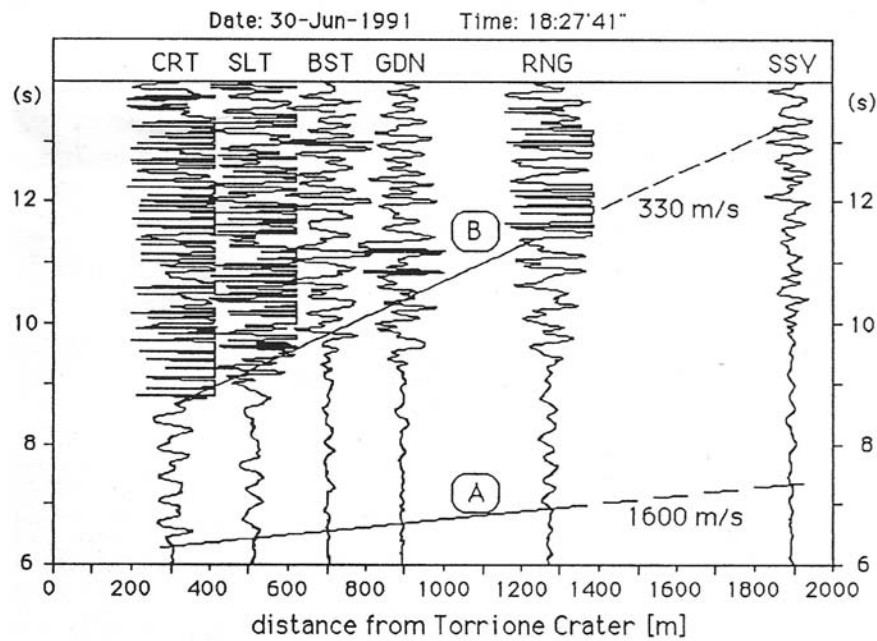
Figure 3.5: *Travel-time representation of an explosion-quake seismogram.*
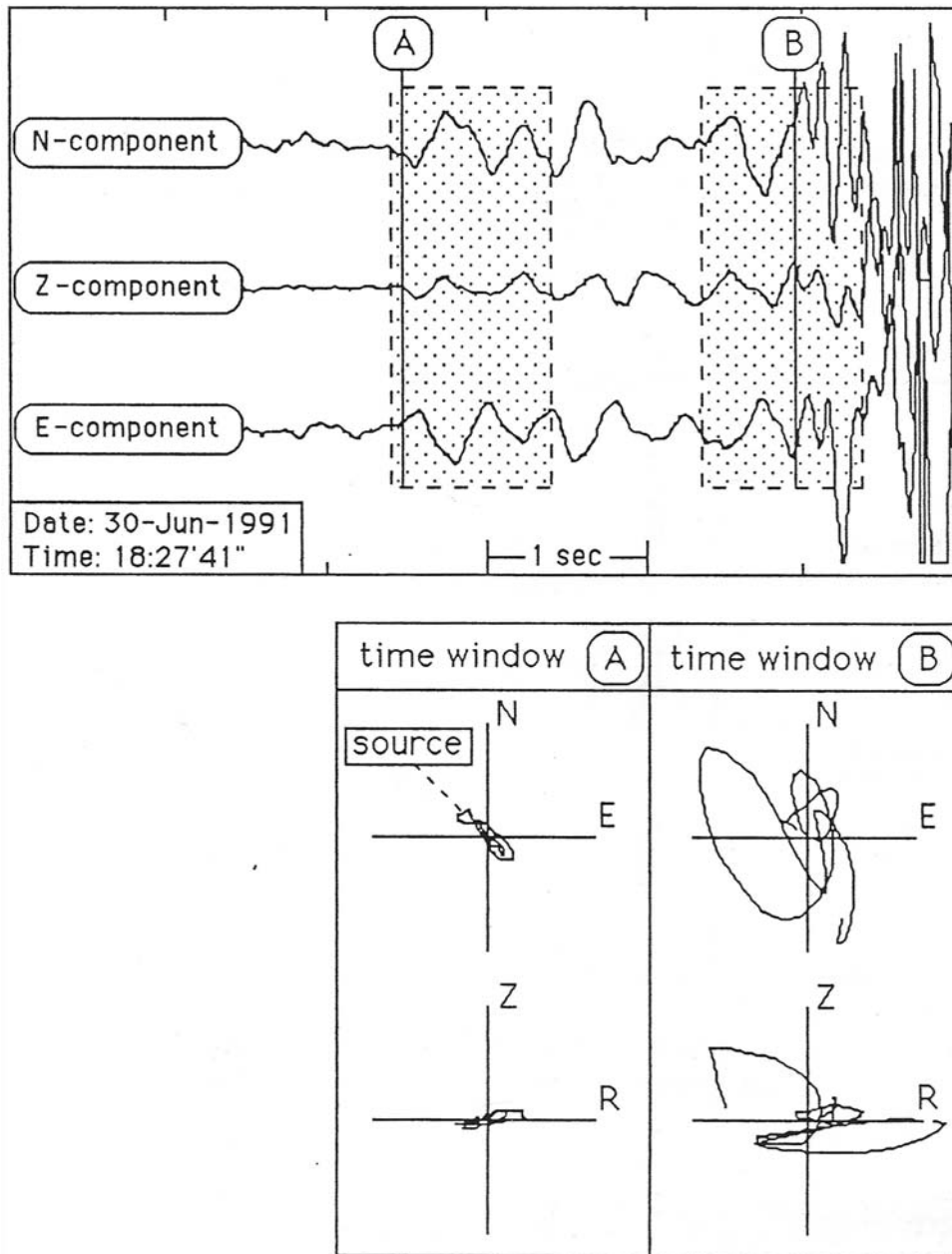
Figure 3.6: *Seismogram and particle motion of the event from figure 3.5, recorded at station SLT.*

As regards the second dominant phase in the explosion-quake seismograms, we believe that the air-pressure pulse generated by volcanic explosion is detected by the seismometer as a high-frequency signal. This interpretation was confirmed

by parallel microphone recording (fig. 3.7); the arrival of the pressure impulse is indeed simultaneous with the high-frequency phase in the seismograms, not only on the vertical (*Dreier et al.* (1994)), but also on all three components. Additional indications for this hypothesis could be also found in seismic prospectings.
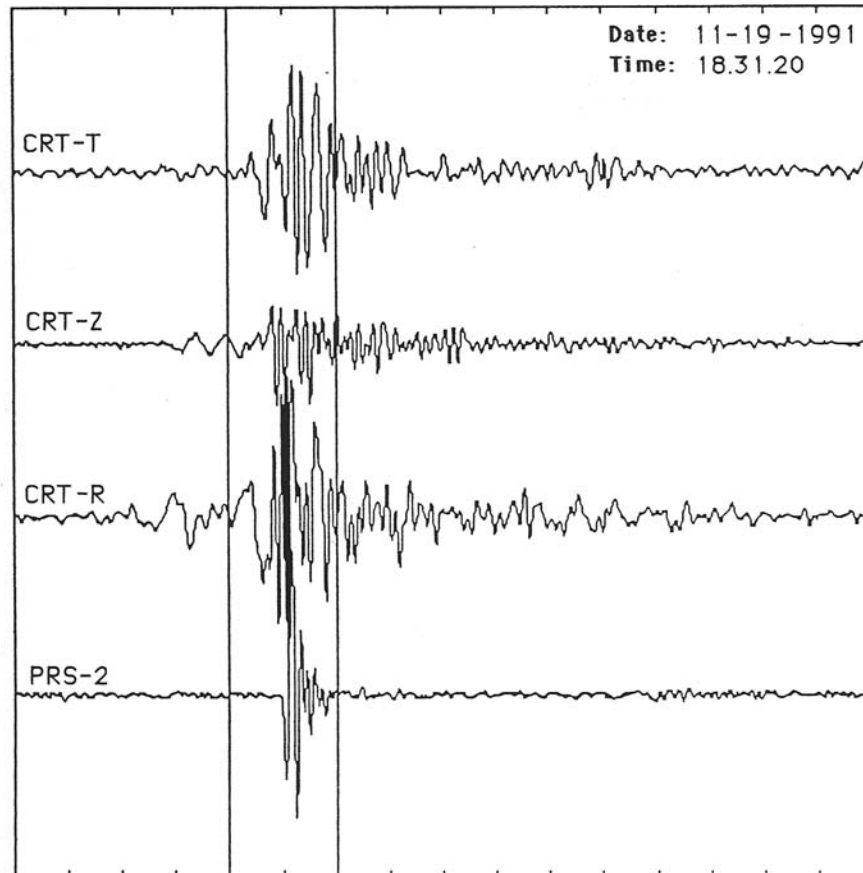
Figure 3.7: *Correlation between 3-component seismic signal (station CRT) and pressure signal.*

The seismic recordings generated by artificial sources show the same signal characteristics and particle motion as the explosion-quake seismograms (*Braun and Ripepe* (1993)). As for the propagation of the air-wave, we believe, that the air-pressure pulse generated by the volcanic explosion hits the ground while travelling in the air. At each point the air-wave enters the highly porous media, composed of loosely packed pyroclastics, and reaches the seismometer as a high-frequency signal. The absorption of the ground is too high to build up a new wave field.

3.4   Magma level determination

The single explosive mechanism we propose requires that the seismic-wave and the air-wave are generated at the same point and the same time. We comprehend the seismic source as an explosion at the top of the magma column, generated by rising gas bubbles reaching the surface (fig. 3.8).

At the explosion instant, shock waves are emitted, partly in the ground as seismic waves (p) and partly in the air ($m + a$). The different path lengths in addition to the different wave velocities of the seismic- and the air-wave could account for the large time difference between p-wave and air-wave onsets, observed even at stations close to the crater (*Braun and Ripepe* (1993)).
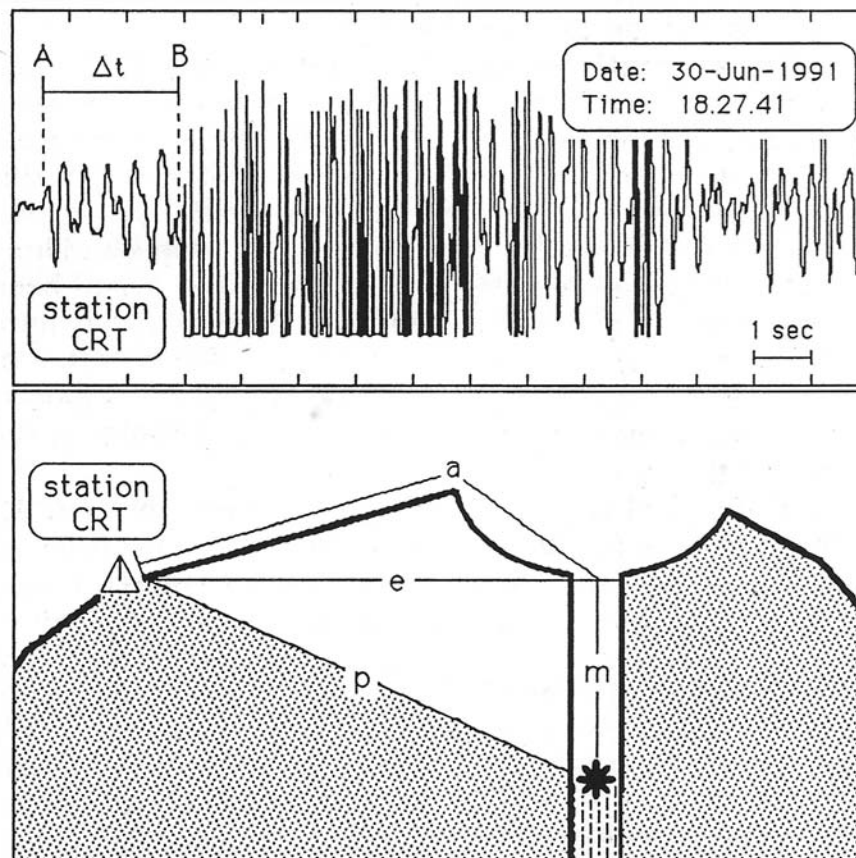
Figure 3.8: *Simple model to explain the travel time difference Δt between the p- and the air-wave onset.*

The variation of the Δt values is very irregular even during 24 hours and varies from one explosion to another in a range from $0.75\ s$ to $2.5\ s$ (fig. 3.9).

By assuming the source mechanism of an explosion at the top of the magma column, we tried to derive the magma level m from the Δt values measured at station CRT. If the geometrical configuration shown in fig. 3.8 is considered, the arrival-time difference Δt between p-wave and air-wave can be calculated as:

$$t_a - t_p = \Delta t = \frac{m}{v_c} + \frac{a}{v_a} - \frac{(e^2 + m^2)^{1/2}}{v_p} \tag{3.1}$$

where:
t_a = arrival time of the air-wave onset
t_p = arrival time of the p-wave onset
m = magma level under stations altitude
v_c = pressure velocity inside the conduit
$v_a = 330\ m/s$ = sound speed in the air
$v_p = 1600\ m/s$ = p-wave velocity
$e = 250\ m$ = epicentral distance (CRT)
$a = 300\ m$ = air-wave path from the conduit to the station (CRT)

The two unknowns in equation 3.1 are the pressure velocity v_c inside the conduit and the magma level m, while the only variable is the delay time Δt. If we assume for the pressure wave the same velocity inside the conduit as in the air ($v_c = v_a$), eq. 3.1 can be solved for the magma level m as a function of Δt. In this case high values of Δt would result from great differences in the p-wave and air-wave paths, indicating a deep magma level (fig. 3.10); on the contrary small Δt values would indicate a shallow source.
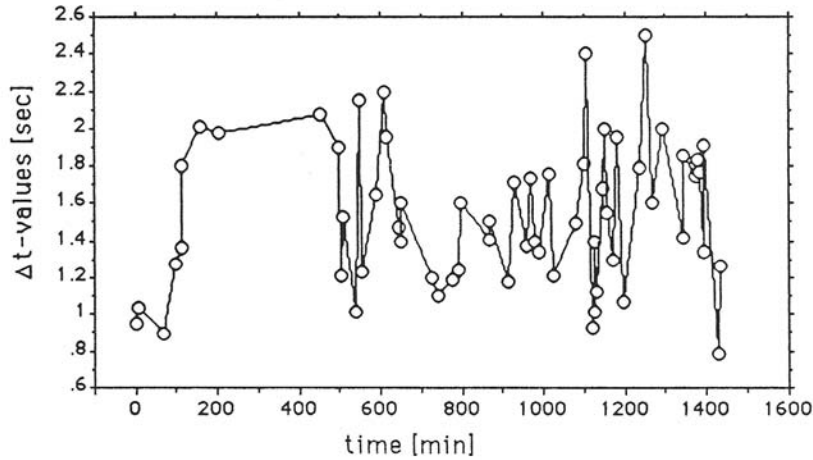
Figure 3.9: *Variation of Δt observed during 24 hours, determined from mixed-type events on June 30, 1991 at station CRT.*

According to this model, the magma level m would drastically fluctuate for small values of Δt. Changes of 0.1 s in the Δt would reflect movements of 40 m large of the magmatic column. When we consider that the Δt can fluctuate from 0.75 s to 2.5 s (fig. 3.9), it appears clear, that the magma level should vary its position inside the conduit of some hundred metres in few hours. Therefore the hypothesis of a pressure pulse travelling in the conduit with the same velocity in the air must be neglected.
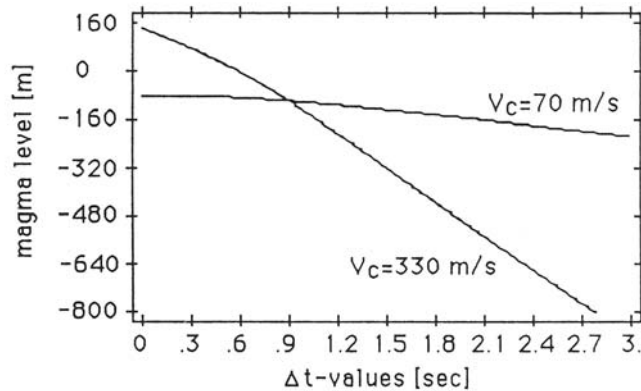
Figure 3.10: *Magma level as a function of Δt.*

On the other hand, if we assume a different velocity for the pressure wave inside the conduit, the sensitivity of the system should be reduced. In order to estimate a realistic range of variability for the velocity (v_c) of the pressure wave inside the conduit, we calculated different families of functions $v_c(\Delta t)$, assuming constant values for the magma level (Fig. 3.11). Only a pressure wave velocity between 30 m/s and 100 m/s can fully explain the large variability of the delay time Δt for small fluctuation in the magma level.

This result seems to be in good agreement with two different physical considerations on the nature of this pressure wave. First, if we assume the pressure wave to be a sound wave, the sound speed in a two-phase flow is much slower than in the air. As reported by *Kieffer* (1977) small changes in the gas content of the magma-gas mixture cause drastic changes in the sound speed. The second hypothesis wants the pressure wave to travel in the conduit with the same velocity as the ejected gas. For this case the velocity of the gas emitted during the volcanic explosions has been measured at Stromboli by *Chouet et al.* (1974), *Weill et al.* (1992), *Ripepe et al.* (1993) as equal to 70 m/s. Assuming this value for the velocity of the pressure wave v_c, the range 0.75 s to 2.5 s for the delay time Δt can be produced by small fluctuations of the magma level in a range of $50 - 130$ m under the crater terrace (fig. 3.12).

3.5   Conclusions

Distinct air-wave phases have been observed before in explosion-quake seismograms of several active volcanoes (*McNutt* (1986); *Mori et al.* (1989); *Okada et al.* (1990)). The recording distance of the respective seismograph stations was usually greater than 5 km, so that the air-shock onsets were clearly separated. At Stromboli the high-frequency phase after a low-frequency onset in explosion-quake seismograms has been mentioned by other authors, but never identified as an air-wave phase. *Fadeli* (1984) related the first long-period onset in the seismogram to a pressure wave generated by the coalescence of gas bubbles, and the second short-period wave group to the disruption of the magma. *Cardaci and Lombardo* (1988) interpreted the low-frequency phase as due to the vibration of the conduit generated by rising gas bubbles, and they related the second high-frequency onset to the explosion mechanism itself. *Ntepe and Dorel* (1990) discussed the low-frequency part of the seismogram as being due to the collapse of a foam layer, exciting the magma chamber. They related the high-frequency onset to the excitation of the terminal conduit by the explosion of a slug, according to the model of *Jaupart and Vergniolle* (1988).
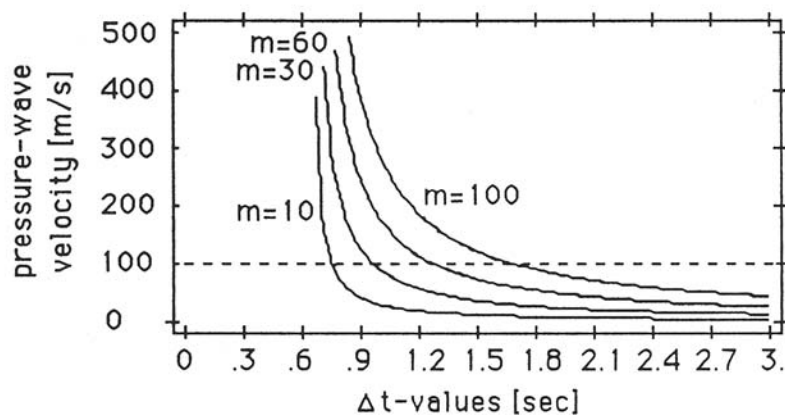
Figure 3.11: *Velocity of the pressure wave inside the conduit as a function of* Δt.

In our analysis we have interpreted the high-frequency onset as produced by a phenomenon completely extraneous to the internal gas-magma dynamics. The high-frequency phase is an air-wave (*Braun and Ripepe* (1993)) generated by the impact of the explosive ejecta on the atmospheric layer. Parallel recordings with a microphone have confirmed the simultaneous arrival of a pressure signal with the seismic high-frequency phase. Besides, from a seismological point of view, the air-wave produces a complicated particle motion on vertical as well on the horizontal planes.
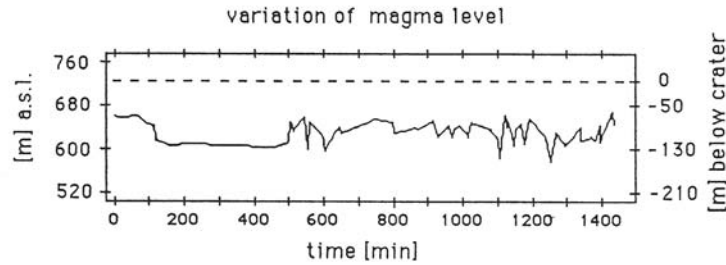
Figure 3.12: *Variation of the magma level during 24 hours, determined from the observed Δt values, shown in fig. 3.9. Inside the conduit a pressure-wave velocity of 70 m/s is assumed.*

The assumption of an explosion at the top of the magma column caused by rising gas bubbles as seismic source, is supported by the reconstruction of the mass fluctuations of the ejecta during an explosion. On this base two main explosive dynamics could be distinguished: a single short pulse, and a multiple and long pulse. The seismic signal characteristics have been associated to a variable number of explosing gas bubbles in the magma (*Ripepe et al.* (1993)). The presence of a p-wave and air-wave, as demonstrated above, supports this source mechanism of exploding gas bubbles at the top of the magma column.

The arrival time difference Δt between the seismic wave and the air-wave onset is thus caused by different path lengths and velocities. When the Δt values are used to determine the height of the magma column, short time variations of hundreds of metres are found considering the velocity of the air-wave inside the conduit (v_c), equal to the sound speed in the air (330 m/s). We calculated that values of v_c ranging from 30 to 100 m/s yield reasonable and more stable magma level around 90 m below the crater terrace. This is in good agreement with the measured gas velocities (*Weill et al.* (1992)) for the explosions at Stromboli.

On the other hand, if we assume that the magma level remains stable at least during a day, the Δt value could reflect variations in the velocity and gas content. Therefore, the amount of gas that is involved in a strombolian explosion, seems to characterize not only the explosive style, but also the seismic signal. One of the main future challenges will be to define the velocity v_c in order to understand the physical nature of the air-pressure wave inside the conduit.

Chapter 4

Infrasonic waves and volcanic tremor

Abstract   The origin of the volcanic tremor is still under debate. Many theories have been proposed in the last years, but none has yet been completely accepted. In 1993, highly sensitive pressure sensors (2.175 $Pa/Volt$) used to monitor the explosive activity at Stromboli have revealed unexpected correlation between small spike-shaped pressure signals ($1 - 2\ Pa$) and volcanic tremor. These pressure pulses repeat regularly in time with a current period of ca. $1\ s$. Video camera images allowed us to correlate the pressure pulse with small gas bursts occurring at one of the active vents. The striking correlation (0.971) between infrasonic and seismic energy fluctuations is particularly meaningful in the frequency domain. Infrasonic and seismic signals share the same spectral content ($3\ Hz$) for every station within a range of 700 m around the craters. Correlations in time and frequency domain remained unaltered during the 1994 field experiments. Moreover, during 1994, the increased degassing activity has been followed by an increase in pressure release ($7 - 8\ Pa$) and by a shift towards higher frequencies ($8\ Hz$) both in the infrasonic and seismic records. Infrasonic waves and volcanic tremor show similar energy fluctuations and frequency contents, appearing therefore to be produced by the same dynamical process. On this basis, we claim that volcanic tremor at Stromboli originates by continuous out-bursting of small gas bubbles in the upper part of the magmatic column.

4.1 Introduction

Volcanic tremor has received great attention in the last 20 years, mainly because it is considered the best precursor of volcanic eruptions. In spite of the physical mechanism of volcanic tremor is still uncertain.

Stromboli volcano is in a steady explosive state (5 – 7 explosions per hour) with volcanic tremor as stationary phenomenon. It has been demonstrated that at Stromboli volcanic tremor assumes different amplitudes according to different explosive activity of the volcano. High explosivity generally coincides with an increase of the volcanic tremor amplitudes (*Nappi* (1976)) while during period with few explosions, volcanic tremor shows low amplitudes.
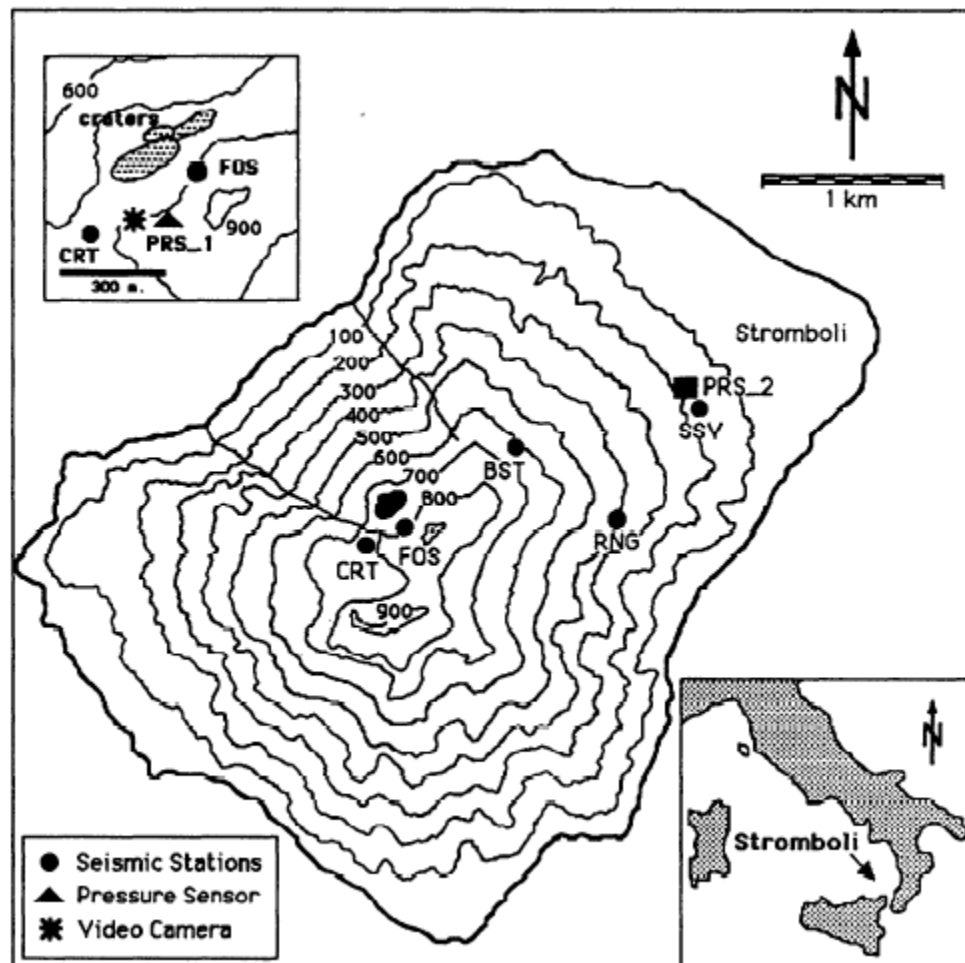
Figure 4.1: *Stromboli map with the position of the seismic stations, pressure sensor and video camera. The close up map indicates the position of the active craters during the experiments in 1993 and 1994.*

Source models have to deal with the low frequency range of the seismic signal (from 1 to 5 Hz) and the stability of some spectral peaks. Both characteristics are common to many volcanoes in the world (*Riuscetti et al.* (1981); *McNutt* (1986); *Gordeev et al.* (1989); *Mori et al.* (1989); *Ferrazzini et al.* (1991); *Vila et al.* (1992)).

Physical models proposed to explain the origin of volcanic tremor take into consideration resonant effects produced by the geometry of volcanic conduits or by vibrations of a fluid-filled tensile-crack generated by the excess of pressure in the fluid magma. Tremor could be originated from resonant effects produced by the geometry of volcanic conduits (*Seidl et al.* (1981); *Ferrick et al.* (1982)). According to this model, different frequency content of the seismic signal is directly linked to the length of the conduit sections.

A different model suggests that volcanic tremor is produced by vibrations of a fluid-filled tensile crack (*Aki et al.* (1977)). Vibrations would be generated by an excess of pressure in the fluid. Magma, moving through sudden openings of tiny cracks, produces tremor. Following this model, it has been proposed (*Chouet* (1985)) that fluid magma vibrates according to oscillations of the crack.

In spite of the different dynamics proposed to explain the origin of volcanic tremor, there is general agreement on the fundamental role played by pressure fluctuations in magma dynamics to generate seismic signals (*Ripepe* (1996)).

Since 1993 the use of high sensitive pressure sensors in "very" near field conditions (150 m from the vent) at Stromboli has revealed that small gas bursts, which are not producing clear seismic transient signal, generate low (ca. 1 Pa) pressure impulses.

According to simultaneous infrasonic and seismic records, we suggest that volcanic tremor at Stromboli is produced by the pressure drop arising from the explosions of small gas bubbles, once they reach the top of the magmatic column.

4.2 Infrasonic waves

To record acoustic pressure waves produced by volcanic explosions at Stromboli, we use since 1992 (*Braun and Ripepe* (1993)) dynamic microphones in parallel with short-period (1 s) seismometers (Mark L4). Microphones are provided with a feedback system shifting the instrumental frequency response down to 1 Hz. Microphone sensibility is 2.175 $Pa/Volt$.

In a volcanic system with open conduits, the explosive source can be thought to be confined at the top of the magmatic column. In this case the source is represented by exploding gas pockets contained in the fluid magma.

This is confirmed by experiments of simultaneous records of seismic and air waves produced by the same volcanic explosion (*Braun and Ripepe* (1993)). Frequency contents ($3-8\ Hz$), propagation velocity (340 m/s typical of sound speed

in the air at 300 K) and low pressure values (5 – 8 Pa), measured at a distance of 150 m from the crater, bring to the conclusion that these atmospheric pressure waves, correlated to volcanic explosions, are infrasonic (*Vergniolle and Brandeis* (1994)).
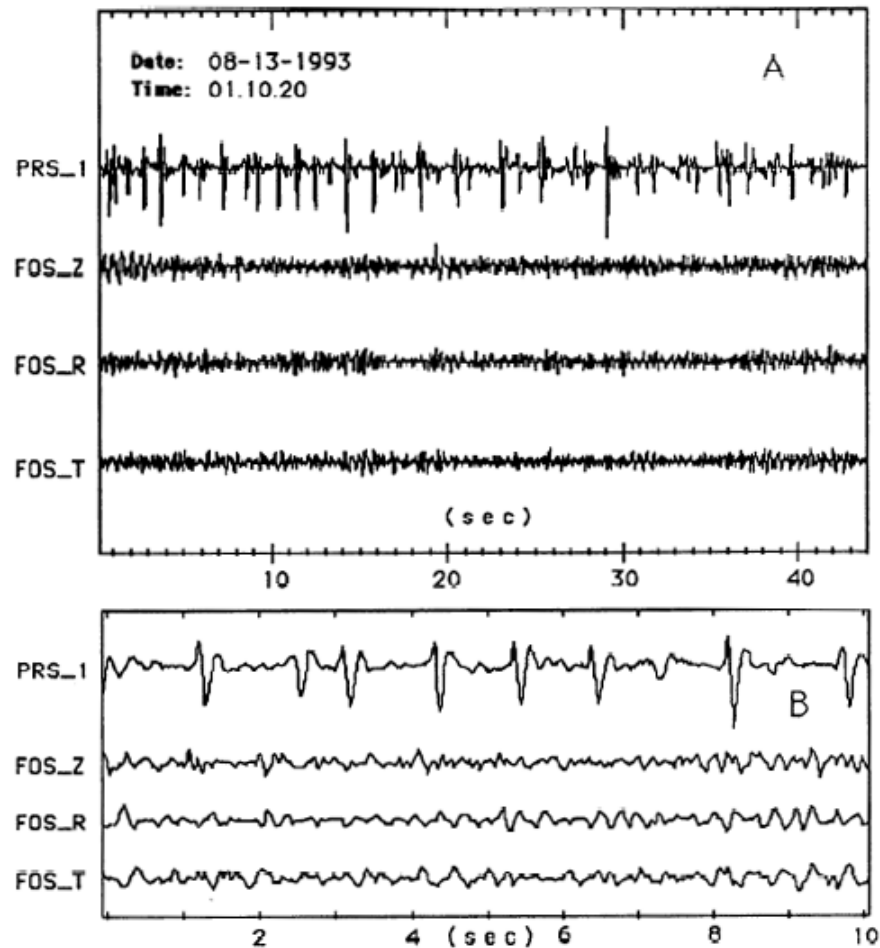
Figure 4.2: *Infrasonic impulses and seismic signals recorded by a pressure sensor and three component station located in the Fossa at only 150 m from the vent. (a) There is no evidence of transient signals in any of the three seismic components. (b) Close up of 10 s long interval.*

The high sensitivity and the small distance (150 m) from the vent (Figure 4.1) of the pressure sensor used, have revealed unusual infrasonic signals even in absence of volcanic explosions. Analyses of video images can prove, that in 1993 and in 1994 such signals are associated with continuous small bursts occurring in one of the active vents. These pressure signals are very low (1 – 2 Pa) and are spike-shaped (Figure 4.2). Moreover they repeat in time with variable time delays

in a narrow range of 0.8 to 1.2 seconds (Figure 4.3).

In spite of the different physical characteristics and different propagation media we tried to demonstrate that infrasonic and seismic waves are connected to the same source. If this is the case, the series of observed gas bursts could be directly responsible not only for the small acoustic impulses, but more importantly, also for the volcanic tremor recorded at Stromboli.
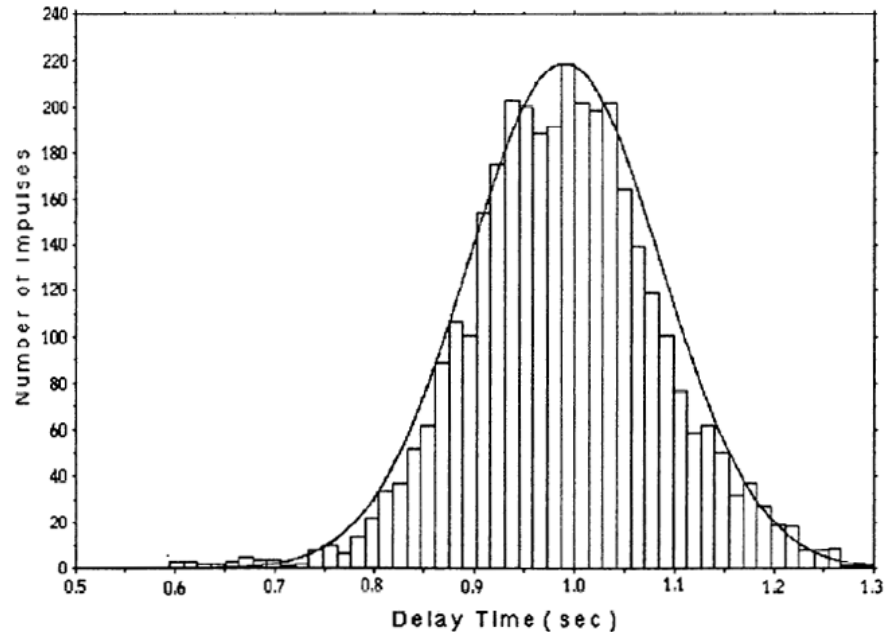
Figure 4.3: *Frequency distribution of the delay times between infrasonic impulses measured for one hour of continuous records. The theoretical Gauss distribution has been calculated taking into account the mean delay time of 1 s and the standard deviation of 0.096 shown in the real distribution.*

4.3 Energy fluctuation

In order to prove that the infrasonic and seismic signals are produced by the same source, we have analysed their temporal energy fluctuation. We here consider the signals recorded by the pressure sensor and by the three-component seismic station located in the Fossa at 150 m from the active vent (Figure 4.1). Seismic and infrasonic energies have been calculated every 6 minutes and in a 30 s large time window, as proportional to the squared amplitude. The comparison between infrasonic and seismic energy fluctuations (Figure 4.4) shows a good correlation (0.971). Nevertheless, it could be argued that the seismic station Fossa is too close to the source to be representative for volcanic tremor.
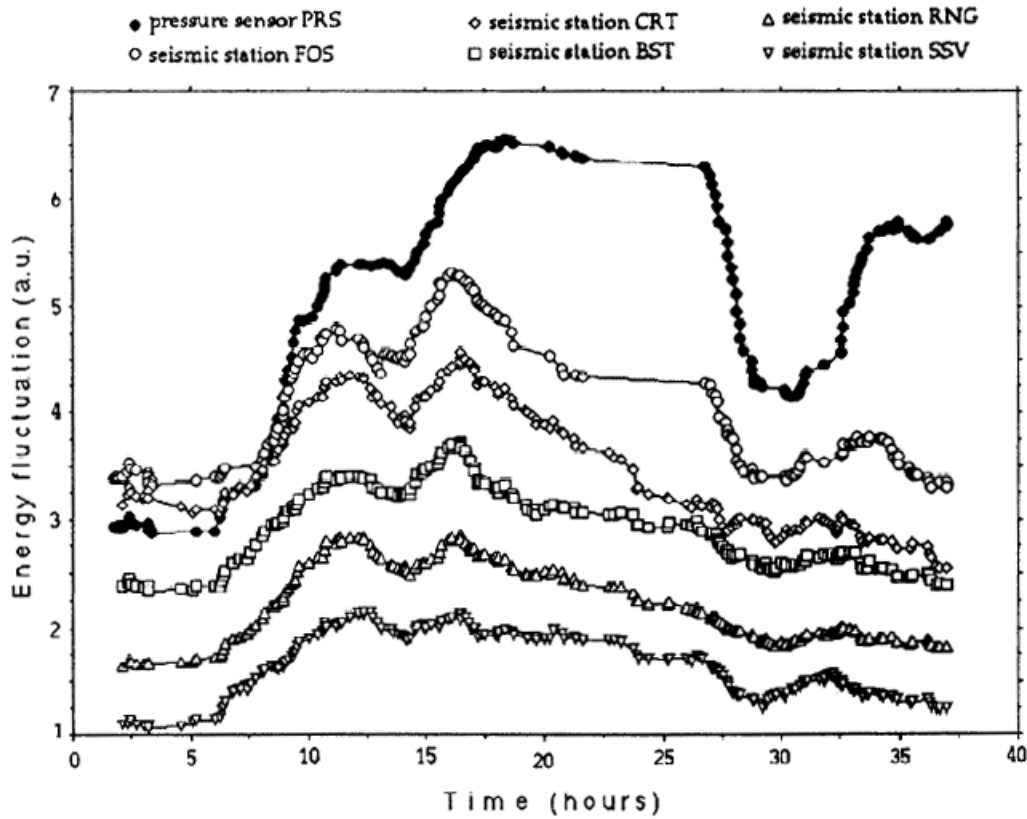
Figure 4.4: *One day energy fluctuations of the infrasonic signals compared to the seismic energy recorded at different seismic stations. Energies calculated at BST, RNG, and SSV stations have been amplified of a factor 2, 2.5 and 2.7 respectively in order to improve data representation.*

If the pressure sensor is really recording impulses generated by the same source of the volcanic tremor, the infrasonic energy must be correlated not only with the seismic energy recorded at the Fossa station, but also with the energy recorded at every station of the seismic network. The same energy analysis was then repeated for the six seismic stations operating at Stromboli during the experiments. We found that: (1) the seismic signal rapidly loses energy moving away from the crater according to high attenuation (Q = 20) of seismic waves and (2) that the seismic energy fluctuations for the six seismic stations are also correlated with the amplitude variations of the impulses recorded by the pressure sensor (Figure 4.4) at 150 m from the vent. The striking relationship between energy variation of infrasonic impulses and seismic energy fluctuations indicates that infrasonic and volcanic tremor are linked together to a common source. This source is dynamically represented by the burst of small gas bubbles at the top of the magmatic column.

4.4 Spectral content

Spectral analyses of seismic and infrasonic signals provide an additional proof to the argument of a common source for infrasonic impulses and volcanic tremor.
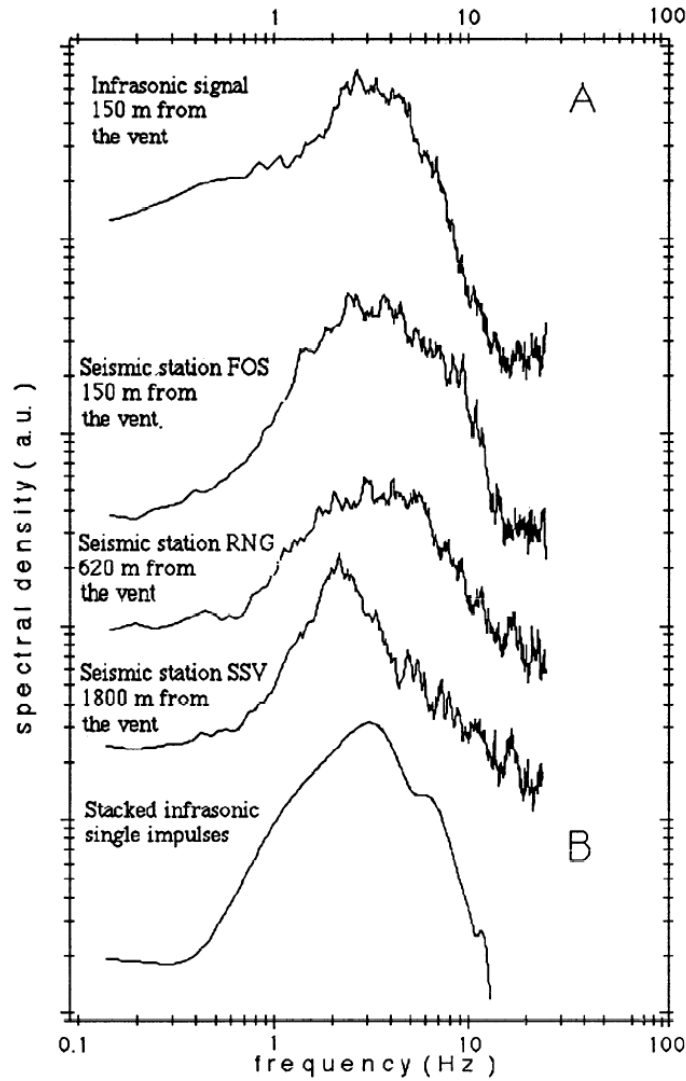
Figure 4.5: *(A) Spectrum of 1 minute of infrasonic records compared with the seismic spectra of different stations at different distances from the source. Note how only at station SSV (1800 m from the source) the spectrum has lost the 3 Hz main peak and shows energy at low frequencies (1-2 Hz). This effect can be due to absorption of the media. (B) Stacked spectrum calculated from the analysis of 200 single infrasonic impulses.*

In fact, if plotted in a log-log scale, infrasonic and seismic signals show spectra with the same general features (Figure 4.5). This is true for the Fossa station, and even for the other seismic stations located within a range of 700 m around the crater. Stacking more than 200 spectra of isolated impulses, we infer that the general trend of log-log spectra for infrasonic and seismic records is controlled by the dominant duration of the single pulses (Figure 4.5).
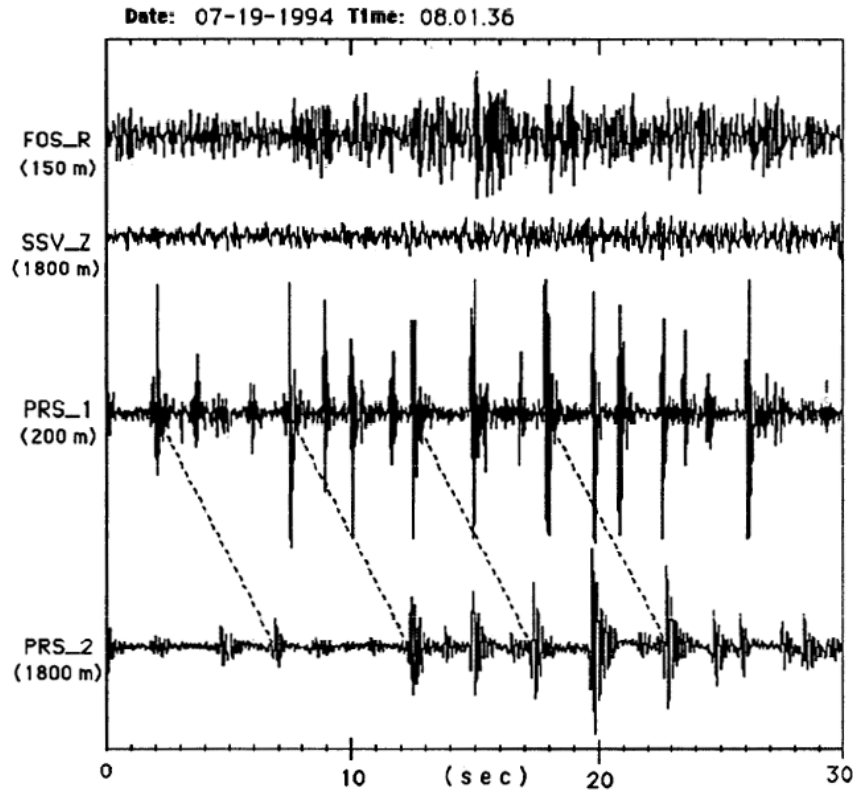
Figure 4.6: *Infrasonic impulses and seismic signals recorded by the three component station located in the Fossa (150 m from the vent) and by the pressure sensor at 1800 m from the vents. Delay times of 4.7 s between PRS-1 and PRS-2 infrasonic impulses are in agreement with a 340 m/s sound velocity in the atmosphere. The increased pressure values (6 – 7 Pa) recorded by the pressure sensor in the Fossa agrees with the visible increment of the degassing activity and with the records of the same impulses at 1800 m from the vent.*

Therefore, the spectrum for a series of impulses maintains the frequency content of the single pressure pulse. This behaviour has been detected also during the 1994 experiments. The degassing activity produced by continuous bursts was so strong that infrasonic pulses were recorded also by the pressure sensor located at 1800 m away from the craters (Figure 4.6).
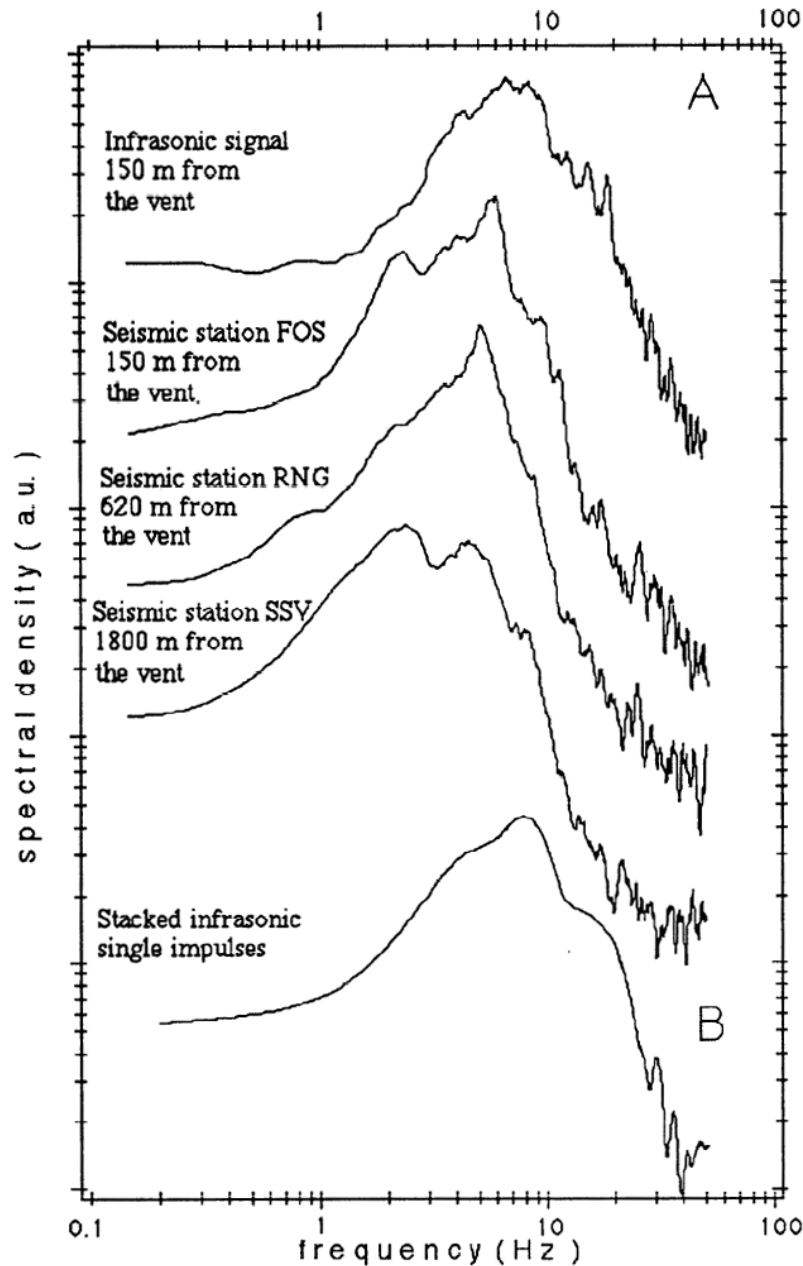
Figure 4.7: *(A) Spectrum of 1 minute of infrasonic records compared with the seismic spectra relative to stations at different distances from the source. Only station SSV (1800 m from the source) has lost the 8 Hz main peak and shows energy at low frequencies (2 Hz). As for 1993, this effect can be due to absorption of the media. (B) Stacked spectrum calculated from the analyses of 200 single infrasonic impulses.*

In this case, the increased pressure (5 Pa) has produced a distinct shift of the frequencies towards higher frequencies (8 Hz). The comparison between spectral content of pressure sensors and seismic signals recorded at every station, revealed a strong relationship between infrasonic and seismic signals (Figure 4.7).

The dominant spectral peaks in volcanic tremor at Stromboli, as at other volcanoes, have been interpreted as produced by resonant phenomena (*Aki et al.* (1977); *Chouet* (1985)).

According to variable delay time between impulses, we interpret spectra as being produced by regular bursting of small gas bubbles. The intermittent pressure drop generates a time series where the source time function (single burst) repeats almost regularly (0.8 – 1.2 s) in time (Figure 4.3).

The latter will produce on the general impulse spectral characteristics a comb-spectrum effect, with stable frequency peaks depending on delay times (e.g. delay time of 0.5 s will generate frequencies at 2, 4, 6 Hz, etc.). The more stable the delay time between the impulses is, the more harmonic the spectrum will be.

4.5   Conclusions

We suggest that volcanic systems with open conduits, such as Stromboli, have the source of the tremor confined at the top of the magmatic column. In this case, the source is represented by exploding gas pockets contained in the fluid magma. This source is in contact with two different media, ground and atmosphere. The shallow position of the volcanic tremor source is responsible for the partitioning of the explosive energy, both in the atmosphere and the ground. It has been demonstrated that the frequency content of acoustic signals produced by explosions of single bubbles in the magma is related to gas overpressure (*Vergniolle and Brandeis* (1994)). We found that gas overpressure also determines frequency content of seismic waves. In fact seismic signals show the same spectral behaviour as infrasonic impulses.

The similarity of spectral content and energy fluctuations undoubtly indicate a common origin for the infrasonic and seismic signals. The origin of volcanic tremor then seems to be related to gas bubbles overpressure.

According to our model the quasi-stable spectral peaks shown by the volcanic tremor do not have to be related to resonant effects, but they originate from regular bursting (every 1 s) of gas bubbles as consequence of intermittent pressure variations during degassing processes. The delay times between impulses produces a comb effect on spectrum. This effect is responsible for many of the frequency peaks which repeat in the spectra at regular time intervals. Infrasonic and seismic signals are produced by the same dynamical process and their analysis will unravel new insights on the role of gas in explosive volcanism.

Chapter 5

On the origin of the long-period tremor

Abstract This investigation deals with the nature of the long-period seismic signals (> 1 s) observed at Stromboli and addresses the question whether they are of volcanic origin or produced by sources such as Ocean Microseisms (OMS). We present results from the analysis of seismic broadband data recorded during 1992 by an array of 9 Guralp CMG-3T seismometers. The determination of the Array Response Function (ARF) shows that array techniques like delay-and-sum beamforming cannot be applied for this purpose, as the extension of the array is limited by the geographical constraint of the island of Stromboli volcano, being simply too small. Spectral analysis reveals three main peaks with periods at 4.8 s, 6 s and 10 s which are not stable in time but vary according to the regional meteorological situation. Whereas 4.8 s and 10 s show up in amplitude spectra calculated during rainy and stormy weather, the 6 s period can be observed during a period of good weather. The signals were first narrowly filtered and then cross correlation, particle motion and amplitudes of the main long periods studied in detail. Relative arrival times as well as seismic amplitudes of the filtered traces do not show any systematic feature, but vary with time. Particle motion analysis demonstrates, that all long-period signals are recorded by the array as plane waves and that the main propagation direction of the 10 s signals is parallel to the wind direction. No correlation with volcanic activity is obvious. We conclude therefore that the three main long periods are not generated by a close volcanic source. We assume a local cyclone to be the seismic source at 4.8 s and 10 s, which represent the Double Frequency (DF-band) and the Primary Frequency (PF-band),

respectively. Concerning the 6 s peak, we speculate a cyclone near the British Isles to act a seismic source.

key words   *long-period volcanic tremor – ocean microseisms – Stromboli volcano – seismic broadband array*

5.1   Introduction

It is only a few years that broadband seismometers have been used not only as instruments in observatories, but also for measurements in the field. Instruments used until now are seismometers of type Guralp CMG 3T (Stromboli: *Neuberg et al.* (1994); *Falsaperla et al.* (1995)) and STS-2 (Sakurajima: *Kawakatsu et al.* (1992); Stromboli: *Dreier et al.* (1994)) with natural periods of 30 s and 100 s respectively. The extension of the seismometer transfer function down to such low frequencies does not necessarily imply that all the seismic signals recorded by the broadband instrument are generated by the same volcanic source. Especially in the long period range other probable seismic sources such as Ocean Microseisms (OMS), swell and wind have to be considered.

In a pilot study performed in 1991, one STS-2 seismometer was installed on Stromboli (198 in fig. 5.1) and recorded volcanic tremor (*Dreier et al.* (1994)). High spectral energy at periods of about 6 s was reported, but it could not be established whether these low frequencies were generated by a volcanic source or if they were related to OMS or swell. Preliminary results from the analysis of seismic broadband data recorded at Stromboli one year later, indicated a strong influence of the seismic long periods from wind and ocean induced noise (*Neuberg et al.* (1994)).

In this study we present some considerations on the determination of the propagation direction of the long-period seismic signals. We show a more detailed analysis of the seismic broadband array data recorded in 1992 (*Neuberg et al.* (1994)) and discuss alternative long-period seismic sources.

5.2   Seismic data

In November 1992 we deployed on Stromboli volcano a seismic broadband array consisting on nine Guralp CMG-3T seismometers with a natural period of 30s. As shown in fig. 5.1 the instruments were installed in two different array configurations (1st and 2nd deployment) recording nearly four days each. The first array had a diamond shape with a distance of 100 m between adjacent stations and was designed to investigate the short period wavefield. The aim of the second irregularly spaced array was to study the long periods and azimuthal wavefield distribution.
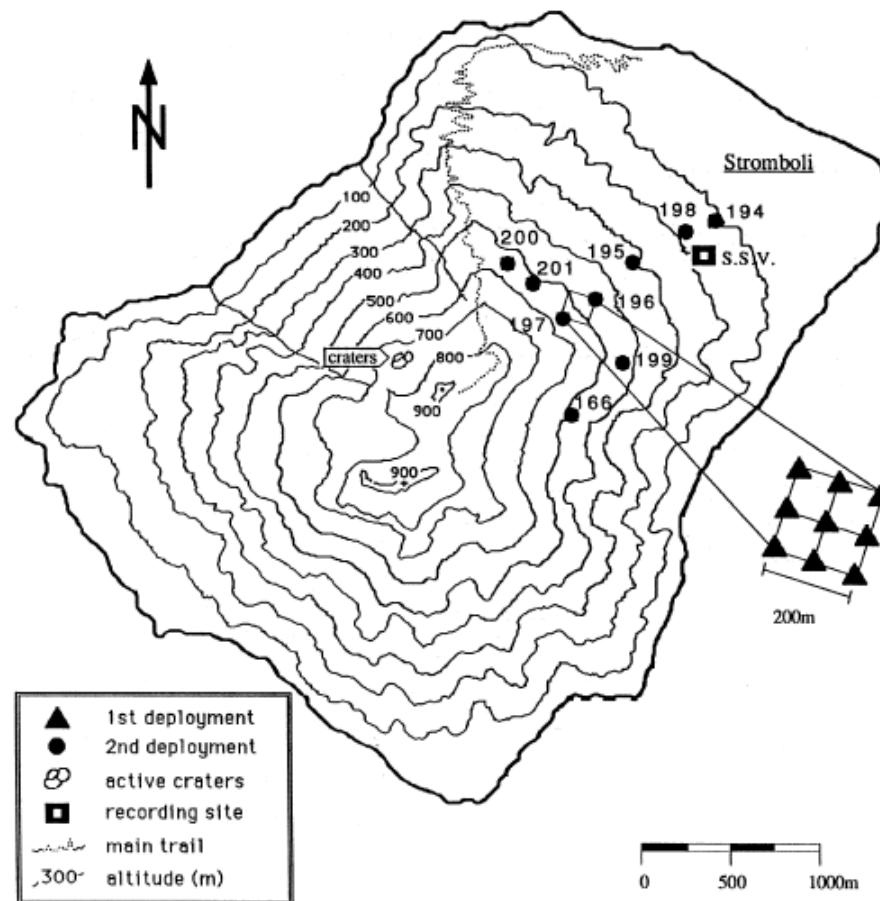
Figure 5.1: *Sketch map of Stromboli volcano with the configurations of the two seismic broadband arrays. The 1ˢᵗ and 2ⁿᵈ deployment are plotted with triangles and circles respectively.*

A detailed description of the seismic experiment is given in (*Neuberg et al.* (1994)).

Analysing the frequency content of the broadband data a considerable part of the seismic energy can be found below 1 Hz (see also *Neuberg et al.* (1994); *Dreier et al.* (1994)). Figure 5.2 shows a typical 3-component broadband velocity spectra at station 197 (see fig. 5.1) calculated for a time interval of 3 h and containing volcanic tremor and explosion-quakes. Long-period spectral peaks (> 1 s) are dominant at 2.3 s, 4.8 s and 6 s.
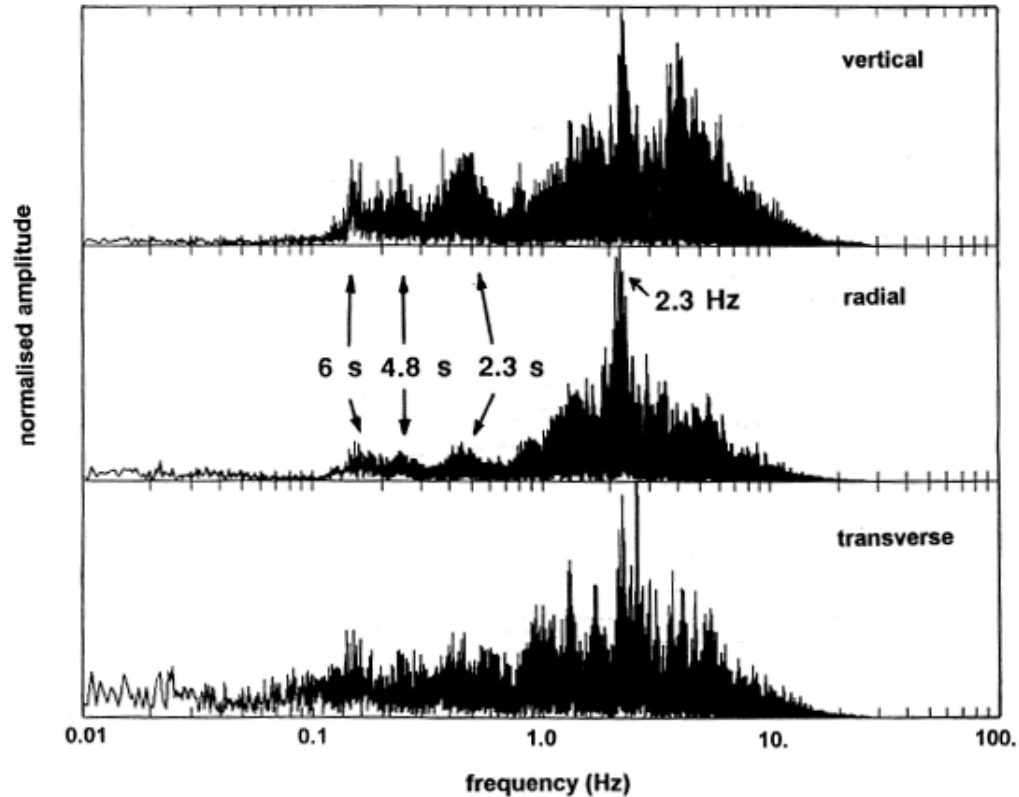
Figure 5.2: *Typical 3-component broadband velocity spectra recorded at Stromboli volcano (station 197). Note the long-period seismic energy at 2.3 s, 4.8 s and 6 s.*

5.3 Array characteristics

In order to locate the seismic sources of the long-period parts in the volcanic tremor, the wave propagation directions of the dominant frequencies have to be determined. Using data from nine seismic broadband stations this problem could be generally solved applying array techniques like *delay-and-sum beamforming* (see e.g., *Harjes and Henger* (1973)). This method can be applied only to plane wavefronts, which is the case if either the array dimensions are small or the source is very distant. The seismic arrays deployed on Stromboli volcano had an extension in the range of the distance from the active craters. Therefore the assumption of plane waves is valid only if the long-period tremor is not locally generated by the volcano but belongs to a remote source like swell originated microseisms. In order to calculate the wavenumber range the different arrays can resolve, the receiver

characteristics $A(\vec{k})$ of the array have to be studied:

$$A(\vec{k}) = \frac{1}{L} \sum_{n=1}^{L} e^{(-i\vec{k}\cdot\vec{r}_n)} \tag{5.1}$$

In eq. (5.1) L is the number of seismic stations and $\vec{k}$ represents the wavenumber vector. $A(\vec{k})$ is also called Array Response Function (ARF) and can be considered as a Fourier transform of the array configuration $\vec{r}_n$. Assuming for the OMS a period of $T_{OMS} = 6s$, propagating with a typical apparent wave velocity of $c = 2.5 \ km/s$ the expected wavenumbers are

$$\vec{k} = \omega\cdot\vec{\alpha} = \frac{2\pi}{T_{OMS}\cdot c} = 0.42 \frac{cycles}{km} \tag{5.2}$$

In order to check if the array extensions are large enough to resolve these wavenumbers we calculated the ARFs for the arrays deployed at Stromboli in 1992 (fig. 5.1). Figure 5.3a shows the ARF for the 1st deployment. With the small dimensions of $200 \times 200 \ m$ only wavenumbers of $\vec{k} \geq 22 \ cycles/km$ are resolvable. Figure 5.3b shows the ARF for the larger 2nd deployment. The main lobe is not symmetric, and wavenumbers from $\vec{k} = 4.5$ to $7.3 \ cycles/km$ can be resolved, depending on azimuth. Obviously the extension of both arrays is too small to resolve the required wavenumbers of $0.42 \ cycles/km$, mentioned above.

In order to look for a better array configuration resolving the long periods, we calculated the ARFs of hypothetical arrays with larger extension. The design of a more suitable array is limited by some geographical constraints: Stromboli volcano is $3500 \ m$ high and only the uppermost $900 \ m$ are above sea level. For this reason the largest array that can be installed on Stromboli cannot exceed the aperture of $4 \ km$. Assuming the stations set at the coast line, the wavenumber resolution ranges from $\vec{k} = 1.4$ to $2.1 \ cycles/km$, depending on azimuth (fig. 5.4). Even in this case the maximal possible extension is not large enough to resolve the typical wavenumbers of the OMS.

A seismometer installed on each of the Eolian Islands (fig. 5.4b) seems to represent a good arrangement for this purpose. The extension of this array would be $80 \times 40 \ km$, corresponding to a wavenumber resolution of $\vec{k} = 0.008 \ cycles/km$ and $0.16 \ cycles/km$, respectively. Nevertheless the shortest distance between the islands are between $10 \ km$ and $20 \ km$, leading to sidelobes between $\vec{k} = 0.62 \ cycles/km$ and $0.32 \ cycles/km$.

In this case spatial aliasing is produced, and this is why delay-and-sum-beamforming cannot be applied successfully for the localisation of the long-period seismic signals even in this case. We are therefore forced to neglect the array technique approach and to systematically analyse the array data with regard to spectral amplitudes, arrival time differences and particle motion.
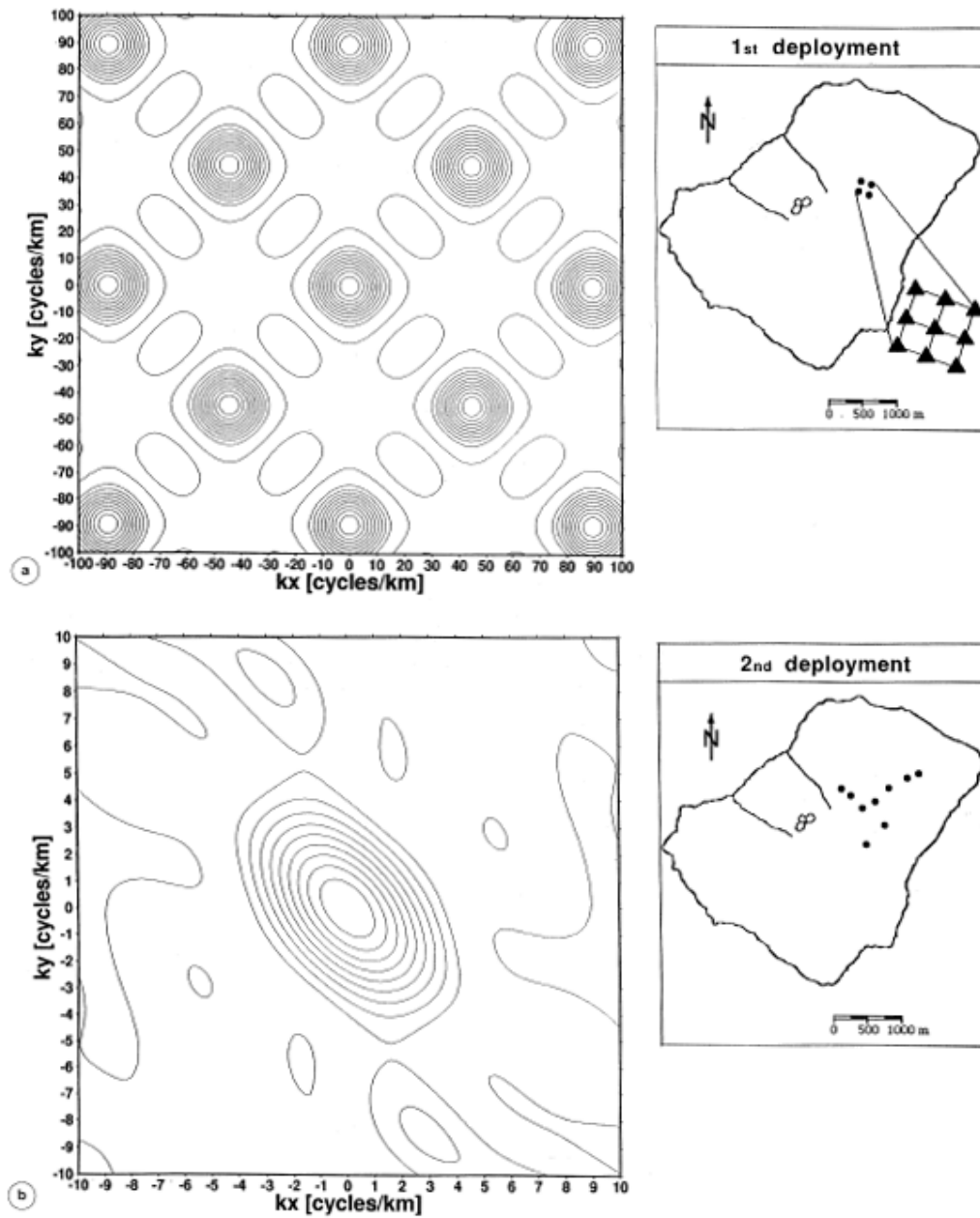
Figure 5.3: a,b. *Array response functions for the 1st deployment (a) and the 2nd deployment (b). On the right side the corresponding station configurations have been plotted in a map.*
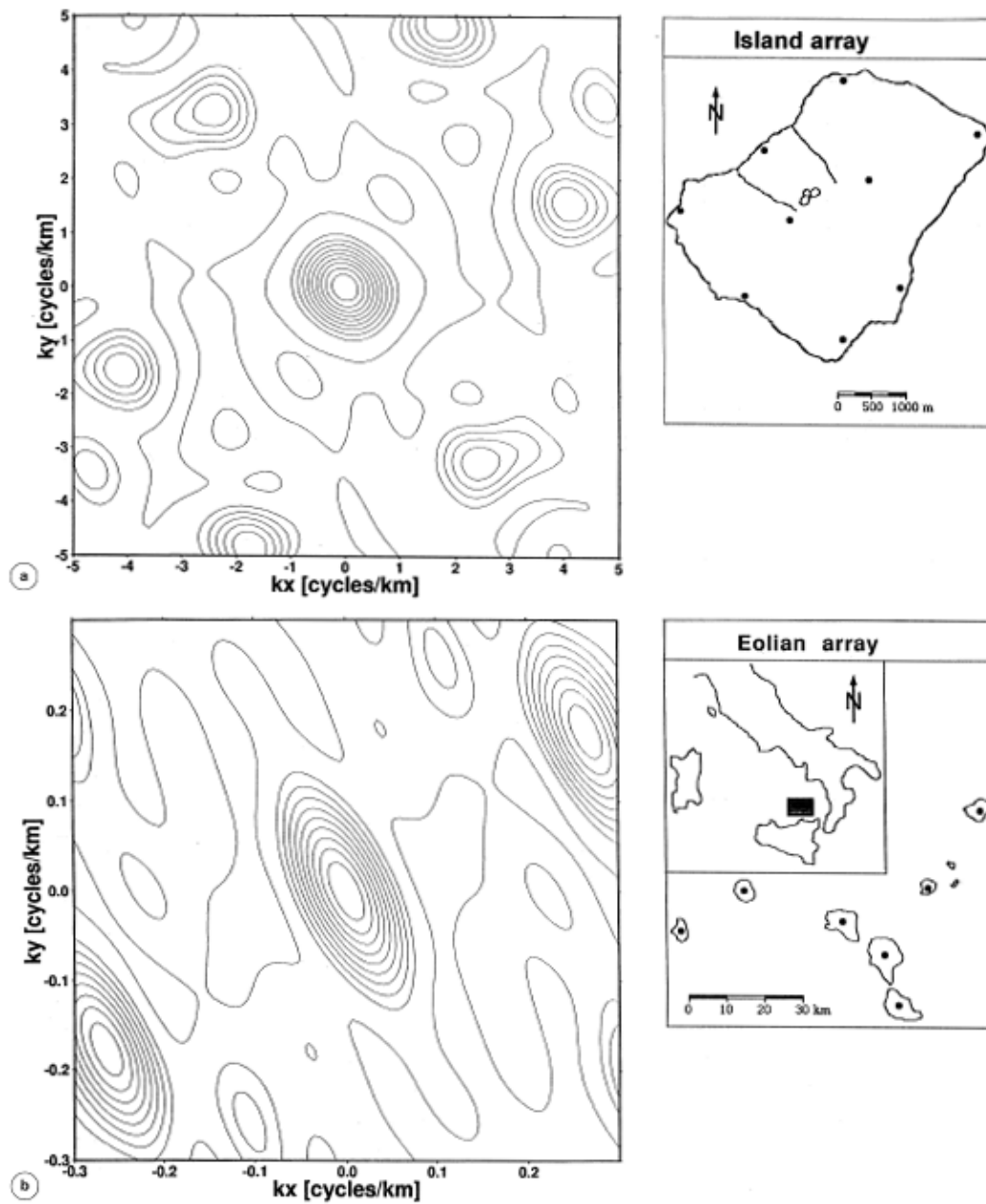
Figure 5.4: a,b. *Array response functions for two hypothetical deployments: (a) Island array: seven stations along the coast of Stromboli plus two central stations; (b) Eolian array: one station on each of the Eolian Islands. The corresponding geographical station positions are plotted on the right side of the figures.*

5.4   Spectral amplitude and weather

Before looking for the propagation direction of the long-period parts in the volcano-seismic signals the frequencies of the dominant peaks have to be precisely determined and their stationarity has to be checked. For this purpose the continuous time series was plotted for the entire recording period of 75 h (for the 2nd deployment) and the overall spectra of volcanic tremor and explosion-quakes were calculated every three hours. Figure 5.5 shows the temporal variation of the amplitude spectra recorded by the N-S component of station 197 (fig. 5.1). The frequency is plotted in logarithmic scale whereas the amplitude of the 24 single figures is plotted in a linear scale normalised to a values of 1600 $\mu m/\sqrt{Hz}$. The single amplitude values can therefore be directly compared. Small icons beside seismic spectra indicate qualitatively the actual weather situation.

Figure 5.5: a,b. *Temporal variation of amplitude spectra (station 197, N-S component) for a time interval of 75 h. Each of the spectra has been calculated for a 3 h time series consisting of volcanic tremor and explosion quakes. Note the correlation between spectral amplitude and the meteorological situation plotted with simplified weather icons. The arrows indicate the time periods that have been chosen for further investigation.*

The seismic record of the 2nd deployment started on 14th November 1992 during a rainy and stormy period. During 15th November 1992 the weather situation improved, wind calmed down and the day after, sunny weather followed. Figure 5.5 shows that during the *bad weather* period, high amplitudes at periods between 4.5 s and 5 s could be observed (from now on mentioned as 4.8 s). They decayed according to the weather improvement and disappeared completely in the evening of 15th November 1992. At the same time a smaller peak at about 10 s showed up and can be noted in figure 5.5. It occurred only during the highest amplitudes of the 4.8 s and disappeared the morning of the 15th November 1992. Nevertheless, following the weather improvement a new spectral peak at 6 s could be observed, starting in the evening hours of the 15th November 1992 and remaining stable until the end of the recording period, 17th November 1992.

Even without a more detailed signal analysis the correlation between the main long periods and the meteorological situation is remarkable and suggests that non-volcanic sources make a considerable contribution to the so called long-period volcanic tremor, recorded with broadband seismometers.

5.5 Data selection

In order to study in more detail the dominant low frequency parts in the volcano-seismic spectra (fig. 5.5), we selected two typical time windows where they could be clearly identified:

(A) 14.11.1992; 13:25, *bad weather*, for the study of the 10 s/4.8 s signals,

(B) 16.11.1992; 11:25, *good weather*, for the study of the 6 s signals.

Within these time windows (A) and (B) – indicated by arrows in fig. 5.5 – we selected a shorter time interval where no volcanic explosion-quake occurred, in order to study signals associated only with *volcanic tremor*. Figure 5.6a,b shows the selected 6 min and 9 min time intervals respectively for the main *bad* (A) and *good weather* (B) periods from all stations. Traces in fig. 5.6 are unfiltered and plotted in the same linear scale. They are normalised to a maximum value of 50 mm/s. Their amplitudes can therefore be directly compared. Note the low frequency content during the rainy and stormy weather (fig. 5.6a), comparable to OMS recordings described by many authors (*e.g.*, *Strobach* (1964) and *Strobach* (1965)). These wave groups – comparable to the quasi periodic oscillations of beating phenomena – are absent during *good weather* (fig. 5.6b).

5.6   Data analysis

5.6.1   Filtering

The two selected *bad* and *good weather* time windows (A and B) were filtered according to the three main periods (4.8 *s*, 10 *s* and 6 *s*) even if they could not be observed in the spectra. This signifies that, *e.g.*, the 10 *s* signal was analysed in the time window (A) *bad weather*, as well as in time window (B) *good weather*. For this purpose we applied a recursive Butterworth Filter (degree 6, forward and backward) with characteristics listed in table 5.1, where T_{center} is the period to be maintained, T_1, T_2 are the low-cut and high-cut frequencies with the bandwidth *df*.

5.6.2   Coherence

Figure 5.7a,b shows the seismic traces of fig. 5.6a,b, filtered around 10 *s* (table 5.1). The upper plot is from the *bad weather* period (A) and shows coherent wavefield over the entire array. However, during the *good weather* interval (B) signal at different stations are completely incoherent. This result was partially expected, because the 10 *s* peak could only be observed in spectra recorded during rainy and stormy weather conditions. This result can be used as a proof that coherence is not artificially caused by digital filtering. We performed the same procedure for the other long periods of 4.8 *s* and 6 *s*, obtaining similar results: coherent wavefield could only be observed of identified in the spectra.

$T_{center}(s)$	$T_1(s)$	$T_2(s)$	$f_1(Hz)$	$f_2(Hz)$	$df(Hz)$	$t_c(s)$
4.85	5.32	4.39	0.188	0.228	0.04	8
6.50	7.14	5.88	0.140	0.170	0.03	11
10.1	11.11	9.09	0.110	0.090	0.02	16

Table 5.1: *Filter characteristics of the narrow recursive Butterworth filter used to bandpass the broadband seismograms. Listed are the center period (T_{center}), the low-cut and high-cut periods (T_1,T_2) and frequencies (f_1,f_2), the corresponding bandwidth df and the coherences time t_c (eq. 5.1).*
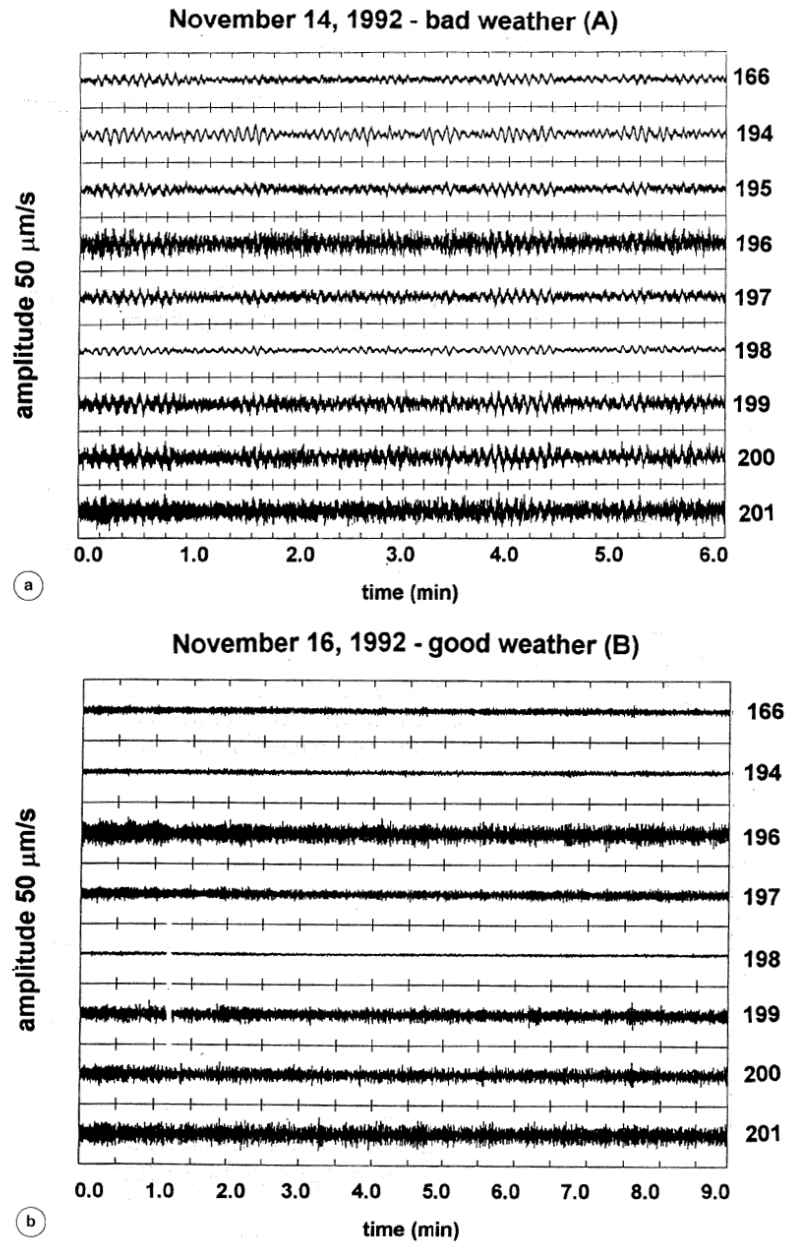
Figure 5.6: a,b. *Unfiltered tremor seismograms (without volcanic explosion quakes) recorded on the radial component of all the stations during (a) the bad weather (A, 14.11.92) and (b) the good weather (B, 16.11.1992) periods (see also corresponding plots n. 1 and n. 16 in fig. 5.5). Note the long-period wavetrains occurring during the bad weather period. The numbers at the right ordinate indicate the respective station number from fig. 5.1.*
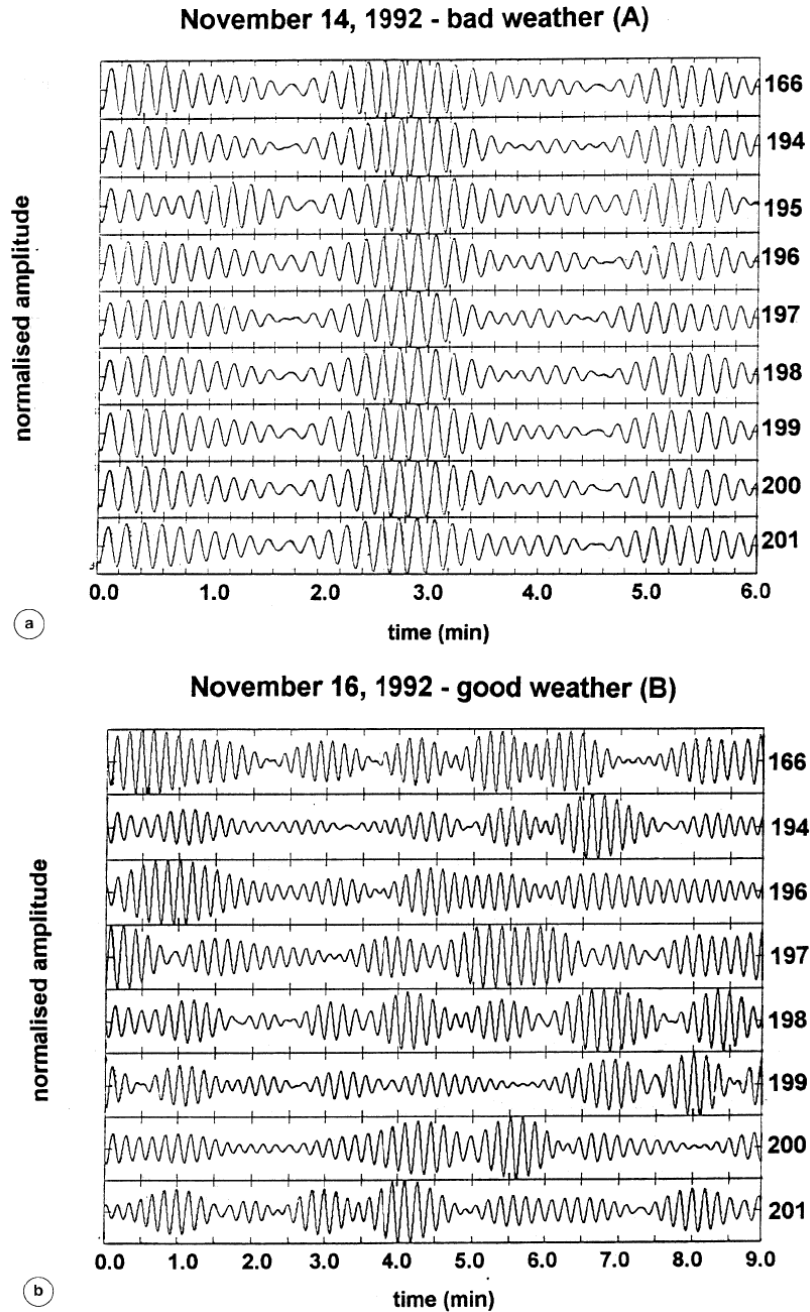
Figure 5.7: a,b. *Seismograms from fig. 5.6a,b filtered around 0.01 Hz with the Butterworth-bandpass listed in table 5.1. The 10 s signal is coherent over the entire array during (a) the bad weather period, whereas during (b) good weather no coherence can be observed. The numbers at the right ordinate indicate the respective station number from fig. 5.1.*

5.6.3   Cross correlation

In order to determine the azimuth of the incident wavefront from arrival time we cross correlated traces among themselves. Despite the high correlation (> 0.9) no systematics in the arrival times could be found. The arrival time sequences at different stations are not stable varying within short time intervals. Such variation was not expected if signals were generated by a local volcanic source.

5.6.4   Particle motion

Applying a narrow filter to a stationary random signal, the particle motion is forced to describe an ellipse, for a time span called coherence time t_c (*Seidl and Hellweg* (1991)). The coherence time t_c depends on the filter bandwidth *df* and can be calculated as (*Seidl and Hellweg* (1991)):

$$t_c = \frac{1}{\pi \cdot df}. \tag{5.3}$$

If a 3-component seismic trace is filtered with a narrow bandpass of bandwidth *df* the corresponding particle motion is significant only if it remains stable for a time span as long as the corresponding coherence time t_c. The respective coherence times for the used narrowband filters are listed in table 5.1.

Figure 5.8a-c shows the horizontal components of the particle motion for the 4.8 *s* (a), the 10 *s* (b) and the 6 *s* (c) plotted for a 6 min duration. The signals were filtered with the narrow bandpass as described in table 5.1. The single plots in fig. 5.8a-c have been arranged in scale according to the position of the recording station in the 2nd deployment (note the scale and the North direction).

Concerning the *bad weather* recordings (A) we can observe that the particle motion pattern of the 4.8 *s* signal shows no preferential direction (fig. 5.8a). Wavefronts arrive from every direction. However, the 10 *s* signal is mainly longitudinally polarised in the N120°E direction (5.8b). Clear and stable longitudinal polarisation can be observed for at least 50 *s*, a time span three times longer than the coherence time ($t_c = 16$ *s*). The result is hence significant and not due to an artificial filter effect.

Concerning the 6 *s* signal of the *good weather* period (B) the polarisation does not have the clear longitudinal characteristic as for the 10 *s* signal but a preferential azimuth in the direction of N140°E can be observed (fig. 5.8c).

Each investigated period shows particle motions displaying the same pattern for every array component. An exception to this is station 194 (see fig. 5.1), where the mean azimuth shows systematically a decrease of 20° if compared to all the other stations. This is probably due to al local magnetic anomaly or to a non correct orientation of the instrument.
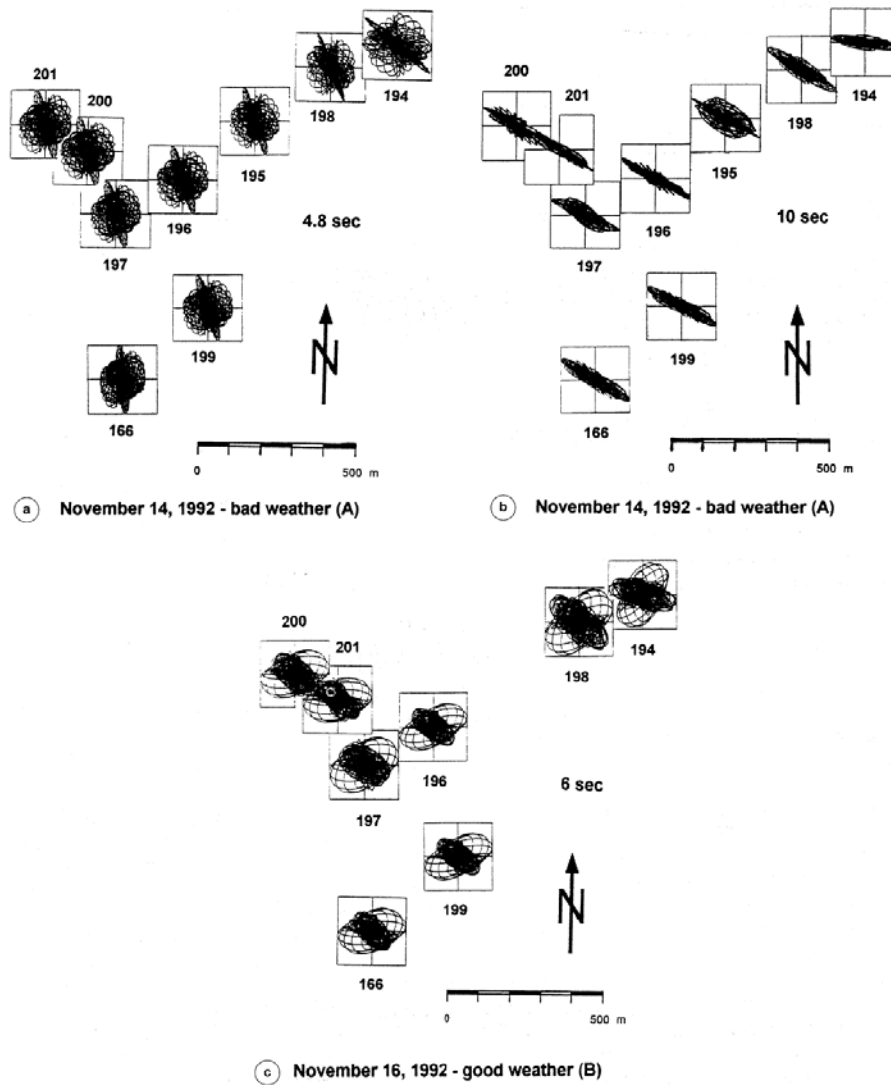
Figure 5.8: a-c. *Particle motion plots for the narrowly filtered signals around (a) 4.8 s, (b) 10 s and (c) 6 s. The single plots have been arranged in scale, according to the position of the seismometers in the 2nd deployment (note the scale and the North direction).*

Nevertheless we conclude from particle motion analysis of the filtered traces, that whichever the case, the long periods of 4.8 *s*, 6 *s* and 10 *s* are recorded by the array as plane waves, therefore not being generated by a local and close volcanic source.

5.6.5 Amplitudes

No dependence of amplitude on station altitude could be observed. We therefore assume differences in signal amplitudes at different stations for unfiltered recordings (fig. 5.6a,b) as due to the site effect. Table 5.2 shows the spectral amplitude $[(mm/s)/\sqrt{(Hz)}]$ of the main long periods, recorded on the horizontal and the vertical components of station 197 (fig. 5.1).

Signal amplitudes on the horizontal components are always larger than vertical ones for the three main periods. For the 4.8 s and the 6 s the horizontal to vertical component ratio is about 3. Nevertheless, for the 10 s this ration is much higher (> 20), since here the vertical component never exceeds the noise level.

5.6.6 Correlation with volcanic activity

After the drastic changes of the long-period tremor in frequency, as well as in amplitude, we looked for a correlation with the volcanic activity. Commonly the short period volcanic tremor is understood as representing a volcanic activity parameter (e.g., *Schick* (1988)), expressed in terms of root mean squared seismic amplitude (rms-value). This correction is not valid if seismic broadband data are used, because high rms-values (fig. 5.6a) are produced by a long-period wavefield with no volcanic origin. Besides this, the variation of the rms-value can be estimated from fig. 5.5. Seismic energy above 1 Hz remains nearly stable during the recording interval of 75 h and weather improvement does not effect the records. Not even the number of explosion-quakes changes, showing a stable value of 11 – 14 explosion-quakes per hour.

Tremor period	Seismic amplitude $[(mm/s)/Hz^{1/2}]$		Ratio
(time window)	horizontal	vertical	horiz./vert.
4.8 s (A)	5000	2000	2.5
10 s (A)	750	45	> 20
10.1 s (B)	450	140	3.2

Table 5.2: *Spectral amplitude $[(mm/s)/Hz^{1/2}]$ and amplitude ratio of the main long periods recorded on the horizontal and vertical component.*

5.7 Discussion and conclusions

Wavenumber characteristics of different array configurations on and around Stromboli volcano show that typical wavenumber values of 0.42 $cycles/km$ for OMS cannot be resolved with delay-and-sum beamforming.

Detailed analysis of the narrow filtered signal shows that periods of 4.8 *s* and 10 *s* appear only during times of *bad weather* (A), whereas the 6 *s* can be observed only during *good weather* (B). We exclude that the three long periods are produced by a volcanic source such as an oscillating magma chamber beneath the volcano for the following reasons:

- particle motion analysis demonstrates that the array records plane waves (fig. 5.8a-c) – an indicator for a remote seismic source;

- seismic energy is much higher on horizontal components, which excludes a deep source;

- neither from arrival times, nor from seismic amplitudes can a propagation sequence be determined.

We assume that the three major long-period signals recorded at Stromboli volcano are part of the OMS and are caused by the actual meteorological situation. Possible sources of the OMS have been widely studied in the past (*Darbyshire* (1950);*Longuet-Higgins* (1950);*Hasselmann* (1963);*Haubrich et al.* (1963);*Strobach* (1965); *Gordeev* (1990); among others). It has been observed that the recorded seismic periods are often half the periods of the dominating ocean waves (e.g. *Darbyshire* (1950); *Haubrich et al.* (1963)). The observations of the so called Double Frequency (DF-band) is consistent with the theoretical model of *Longuet-Higgins* (1950), which describes standing waves as an OMS source.

As stations installed near coasts or on islands, additionally weaker amplitudes can be observed within the Primary Frequency (PF-band). These periods have been associated with strong winds (*Oliver and Ewing* (1957); *Gordeev* (1990)).

The long-period seismic signals at a frequency twice the PF-band show high energy content and are well known. *Haubrich et al.* (1963) report up to 100 times more seismic energy for the DF-band than for the PF-band.

In our data, the unfiltered seismogram recorded during *bad weather* (fig. 5.6a) is very similar to the quasi periodic oscillations of the OMS, as described, e.g., by *Strobach* (1964). The typical seismic *bad weather* long periods at 4.8 *s* and 10 *s* (A in fig. 5.5) show the frequency relation 2:1, described, e.g., by *Haubrich et al.* (1963). Seismic energy – roughly estimated from table 5.2 a squared amplitude in the horizontal components – shows 50 times higher values for the 4.8 *s* (DF-band) than for the 10 *s* (PF-band).

Looking at the particle motion plots (fig.5.8a,b) no polarisation can be found for the 4.8 *s* signal as would be expected from microseisms generated by swell. Nevertheless, the particle motion pattern of the 10 *s* signal shows a clear longitudinal polarisation in N120°E which is identical to the wind direction, determined from a meteorological map of November 14, 1992, 12:00 GMT (fig.5.9).
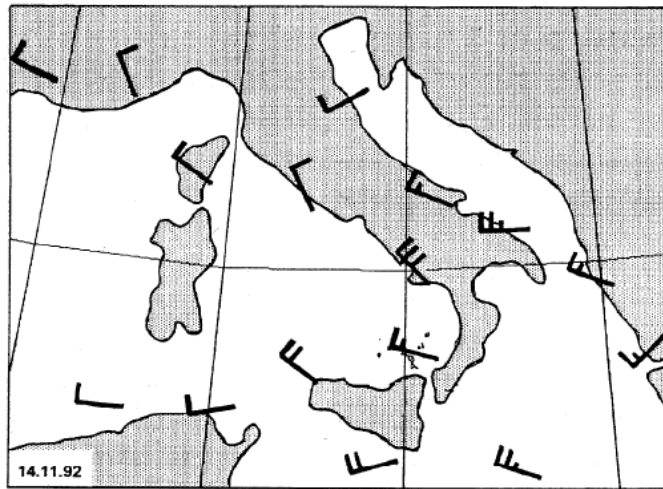
Figure 5.9: a,b. *Wind direction (horizontal line) and wind velocity (vertical line) at November 14, 1992 taken from a meteorological map. One vertical line corresponds to 30 kt per hour.*

The lack of energy on the vertical component (see table 5.2) leads us to the conclusion that the 10 s signal is caused by the wind, generating ground inclination, rather than propagating waves. This result is consistent with a study of *Berckhemer and Akasche* (1966) on seismic ground noise and wind, at the seismological observatory Gräfenberg-Germany (GRF). The amplitudes of the 4.8 s and the 10 s signals decrease in time, following the weather changes as shown in fig. 5.10, where the meteorological situation in Europe is presented day by day, starting on 14th November 1992. A low pressure area, located on the Tyrrhenian Sea on 14th November 1992, moved quickly eastward. Wind reached velocities up to 160 km/h blowing from WNW (fig. 5.9).

On the basis that:

(i) the actual wind direction was identified in the seismogram (10 s in figs. 5.8b and 5.9a),

(ii) the seismic amplitudes of the *bad weather* periods (4.8 s, 10 s) decreased with weather changes (figs. 5.5 and 5.10),

(iii) the 4.8 s and 10 s signals show the PF/DF-band characteristics,

(iv) we have not been able to identify any change in volcanic activity,

we conclude that 4.8 s and 10 s periods were generated by the cyclone that passed quickly south of Italy during 14th November 1992 (fig. 5.10).
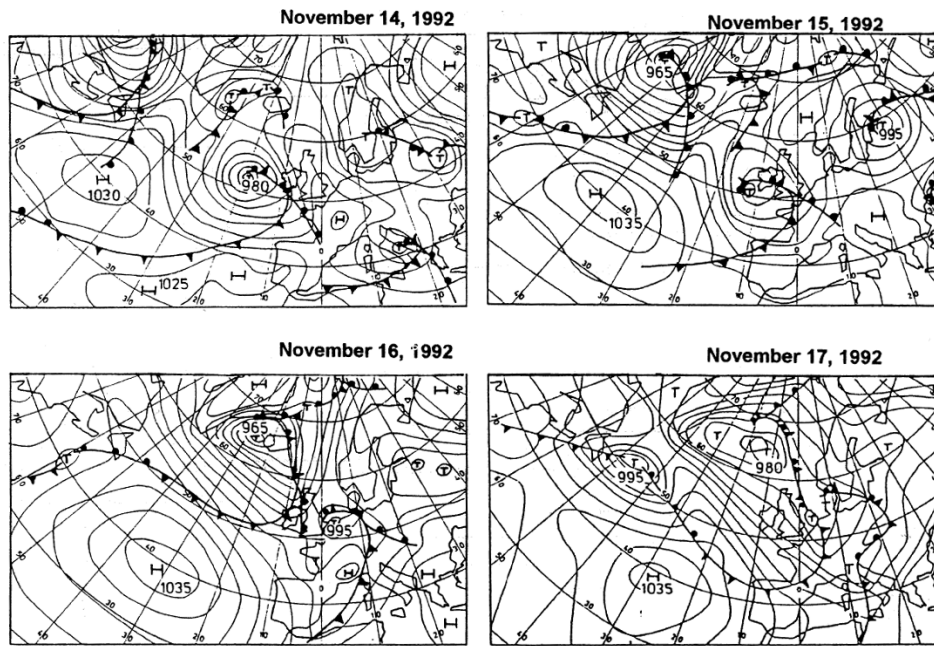
Figure 5.10: a,b. *Development of the meteorological situation in Europe, between 14ᵗʰ and 17ᵗʰ November 1992.*

As for the 6 s peak the interpretation is more difficult. The propagation (N140°E in fig. 5.8c) we observed is slightly different from that one determined for the 10 s signal, during the *bad weather* interval. Even in this case no indication for a volcanic origin has been found and also the 6 s signal seems to be generated by the OMS. For seismic broadband stations located on the continent, such as GRF (*Henkes* (1991)), the 6 s period is already known as OMS generated in the Atlantic region. Looking at fig. 5.10 a strong low-pressure area near England can be localised after 15ᵗʰ November 1992 moving slowly towards Europe. This cyclone could be responsible for the occurrence of the 6 s period in the seismic energy recorded at Stromboli volcano.

Chapter 6

Further studies on the origin of the long-period tremor

6.1 Introduction

From a seismological point of view, *volcanic tremor* represents the source of information on the complex internal processes inside a volcano. A main difficulty in the study of the volcanic tremor recorded at Stromboli is determining whether the high energy in the long-period part of the broadband spectra $(2 - 10 \ s)$ is generated by volcanic activity or by ocean microseisms (OMS).

Seismic noise recorded outside active volcanic areas in a period range between $2 - 15 \ s$ is generally generated by ocean waves and swell and therefore called *Ocean Micro Seisms* (OMS). *Longuet-Higgins* (1950) published a paper explaining how kinetic energy of the water waves is transmitted into the ground. He proposed the pressure transfer of standing waves on the sea floor as driving mechanism. When the area generating coherent standing waves is large with respect to the water depth, the kinetic energy becomes transmitted into the ground. The oscillation period is half the period of the exciting water waves (*double frequency*). Depending on the coastal shape, the OMS can also be generated by swell. This mechanism can be very efficient if the orientation of the coast line coincides with the front of the arriving surging billow. In this case the seismometer records directly the surf period (*primary frequency*).

The present chapter extends the study of chapter 5 and uses additional seismic, meteorological and mareographic data in the same recording period.

6.2   Analysis of seismic data

6.2.1   Remarks on the data analysis

The first approach was to compare power spectra recorded at Stromboli (STR), with those recorded at a seismic broadband station installed on non-volcanic underground. For this purpose noise spectra from the seismic broadband station l'Aquila (AQU), located in the Central Apennines (90 km NE of Rome, fig. 6.8), were calculated for the period November 14 – 17, 1992.

To have a correct comparison, the instrumental characteristics of the STR- and AQU-data had to be adapted to each other. As already introduced in chapter 5 the seismic sensors deployed temporarily at Stromboli were of type Guralp CMG-3T (30 s), whereas station AQU is equipped with a STS-1 seismometer (360 s). Being interested exclusively in the long-period part of the spectra, the STR-data (sampling interval 0.016 s) was interpolated and decimated to 20 Hz, according to the sampling rate of the Quanterra digitizer operating at AQU. In a second step the AQU-data was high-pass filtered by a 6-pole Butterworth filter at a corner frequency of 0.033 Hz ($T \approx 30$ s).

The Power Spectral Density (PSD) was calculated by estimating the periodogram, which can be obtained by squaring the Fourier-Transform

$$P_T(f) = \frac{1}{T} | \int_0^t x_T(t) e^{-i2\pi ft} dt |^2 \tag{6.1}$$

using a combination of the *Welch*-Method (averaging of single spectra of overlapping data segments) and the *Daniell*-Method (averaging of contiguous Periodogram-values). For the window length a value of $T = 786$ $s = 15720$ $samples$ ($\approx 2^{14}$ $samples$) was chosen, corresponding to a spectral resolution of $\Delta f = \frac{1}{T} \approx 0.00127$ Hz. For the calculation of the PSD, the following steps have been conducted:

- subdivision of the 3-day record in 74 records of 1 h length

- subdivision of the 1 h records in 786 s long time windows, corresponding to a 50% overlap

- Calculation of the PSD for every single time window

- Summation of the eight single spectra und averaging

- Smoothing and storage of the averaged PSDs

The power spectra calculated for longer time windows (figure 6.1) have been obtained by stacking and averaging of the single 1 h – power spectra. The seismic traces used for the calculation of the PSD are proportional to ground velocity $[m/s]$ and hence the dimension of the ordinates of the PSD-diagrams pictured in chapter 6.2.2 is $\frac{(m/s)^2}{Hz}$.

6.2.2 Comparison of the tremor spectra with noise spectra recorded at station AQU

Fig. 6.1 shows the PSD calculated at stations AQU and STR for all three components on the entire recording period of 74 h, following the procedure described in chapter 6.2.1.
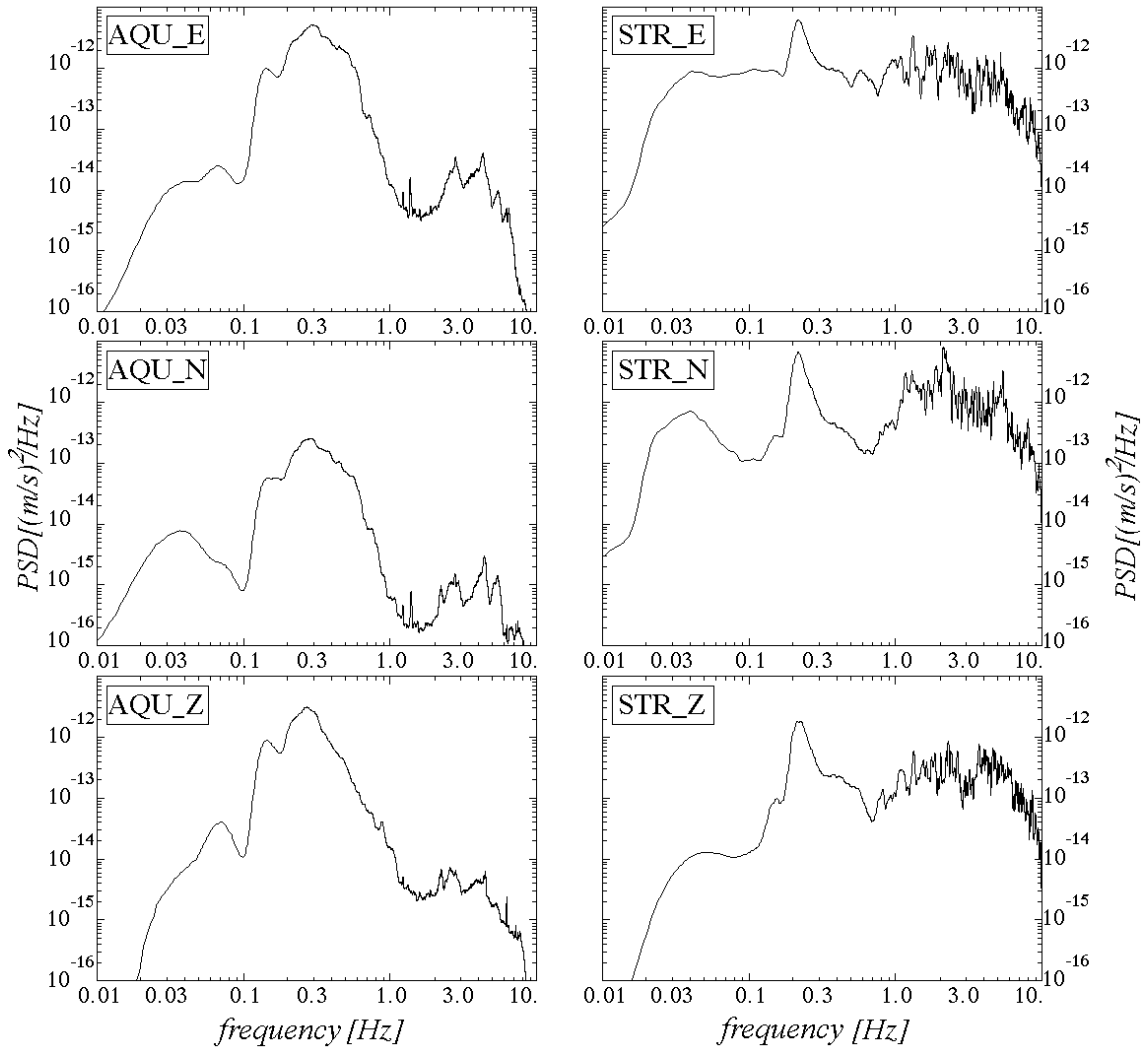
Figure 6.1: *Power Spectral Density determined at the stations AQU and STR for the entire record length of 74 h.*

The PSD for AQU and STR in figure 6.1 are plotted in the same scale. The dominant feature in the noise spectra of station AQU is the high spectral density values between 0.1 and 0.7 Hz, with two local peaks a smaller one at 0.15 Hz and

a broader maximum around 0.3 Hz. The seismic energy in this frequency band is known to be generated by surf and swell during the passage of cyclones and is called *ocean microseisms*(OMS). Following *Longuet-Higgins* (1950) these two well known peaks are called *Primary Frequency Peak* (PF) and *Double Frequency Peak* (DF) (chapter 6.1).

Also the energy maximum in the tremor spectra (STR-E, STR-N, STR-Z in fig. 6.1) is found between 0.2 and 0.3 Hz, but here the spectral energy is concentrated in a narrower frequency band. The energy within the tremor frequency band (above 1 Hz) in the STR spectra, is several orders of magnitudes higher than for AQU. The reason is the volcanic activity of Stromboli, the well known short-period tremor (chapter 4).

At a first glance the differing PSD at AQU and STR (figure 6.1) might suggest that OMS cannot be the cause for the long-period part in both spectra. Particularly the small energy maximum between 0.2 – 0.3 Hz in the STR-record is uncommon for the OMS and was therefore studied in more detail.

6.2.3 Stationarity of tremor spectra observed at STR

The first step was to check the stationarity of the main long-period spectral peaks (chapter 6.2.2) for the entire data record (from November 14 – 17, 1992). Continuous seismic data recorded at the station nearest to the crater (197 in figure 5.1, from now on called STR) was used to study the temporal variation of the spectral content of the volcanic tremor. The entire 74 h dataset was divided in 3 h windows, power spectra calculated according to chapter 6.2.1, and the results were depicted in a *waterfall* plot. The figures 6.2, 6.3 and 6.4 show the respective temporal variation of the power spectra of the E-, N-, Z-component, determined at station STR between November 14, 1992, 12:00 UTC and November 17, 1992, 14:00 UTC. Each single power spectrum was calculated for the unfiltered continuous data stream, including volcanic tremor and explosion-quakes. In the power spectra calculated on November 16, 1992 between 12:00 and 15:00 UTC (figures 6.2, 6.3, 6.4) high energy was observed on all three components within the analysed frequency band, and hence was clipped manually.

A first qualitative analysis of the power spectra of all three components shows that the energy level above 1 Hz remains nearly constant during the 74 h recording period. However, one can find strong temporal variations in the long-period part of the power spectra. On November 14, 1992 the tremor spectra (figures 6.2 – 6.4) are dominated by high power at frequencies around 0.21 Hz, corresponding to a period of $T \approx 4.8\ s$. The amplitude of this frequency peak decreases exponentially with time, reaching the background noise level after about 36 h (November 16, 1992, 00:00 UTC). During the first 15 hours, the power spectra of the horizontal components show an additional peak at 0.105 Hz ($T \approx 9.6\ s$), having energy about 30 – 50 times lower than the previously described peak. Following the *fade-out* of

the spectral energy at 0.21 Hz ($T \approx 4.8\ s$) at November 15, 1992 15:00 UTC, a new spectral peak appears at 0.15 Hz ($T \approx 6.6\ s$), which can be observed principally on the vertical component till the end of the record. During the last 24 hours a second broader spectral peak appears between $0.3 - 0.6\ Hz$, which does not reach the sharpness and stability of the formerly described spectral peaks.
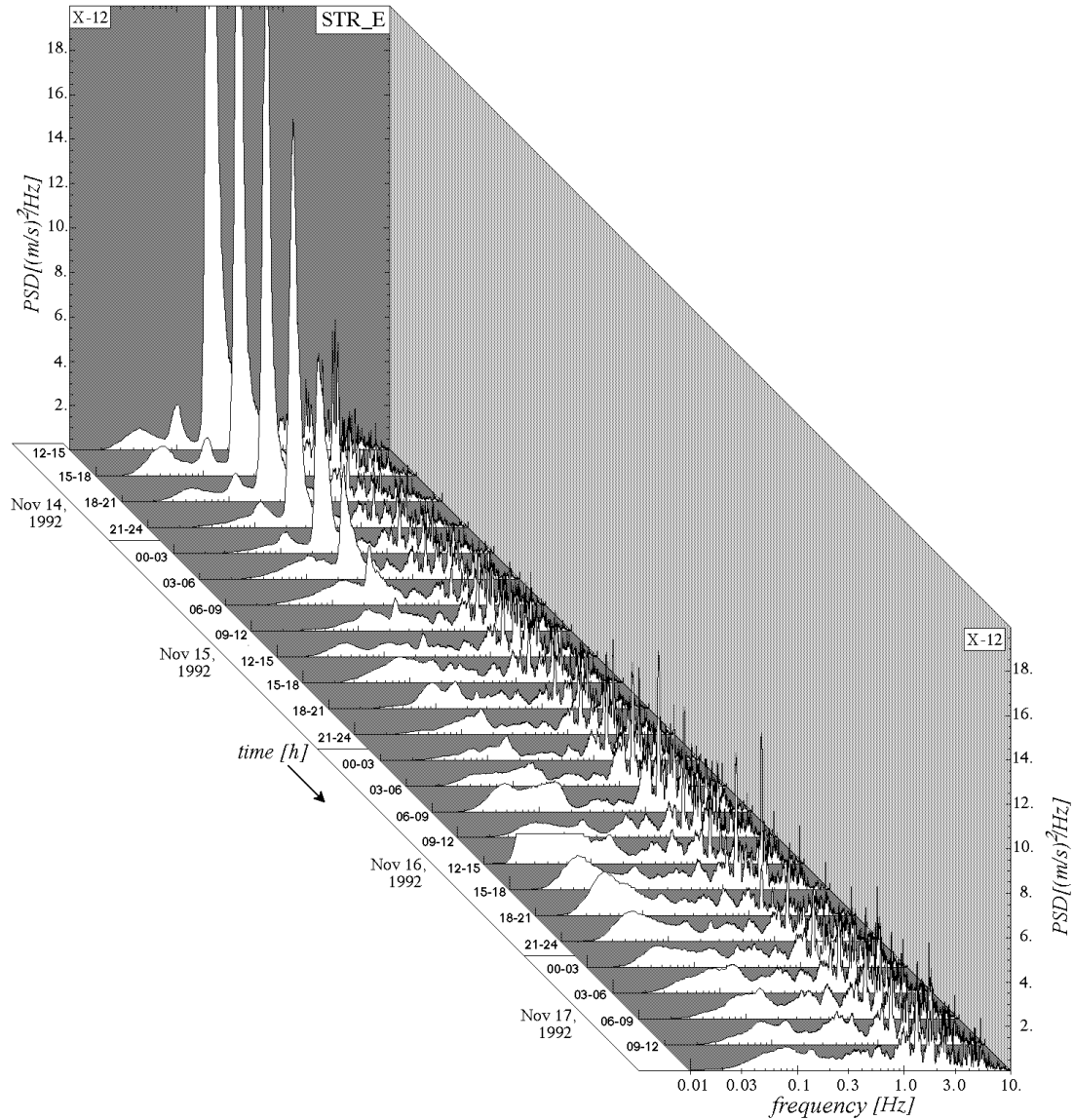
Figure 6.2: *Temporal variation of the Power Spectral Density calculated for the 74 single-hour records of STR (E-W component).*
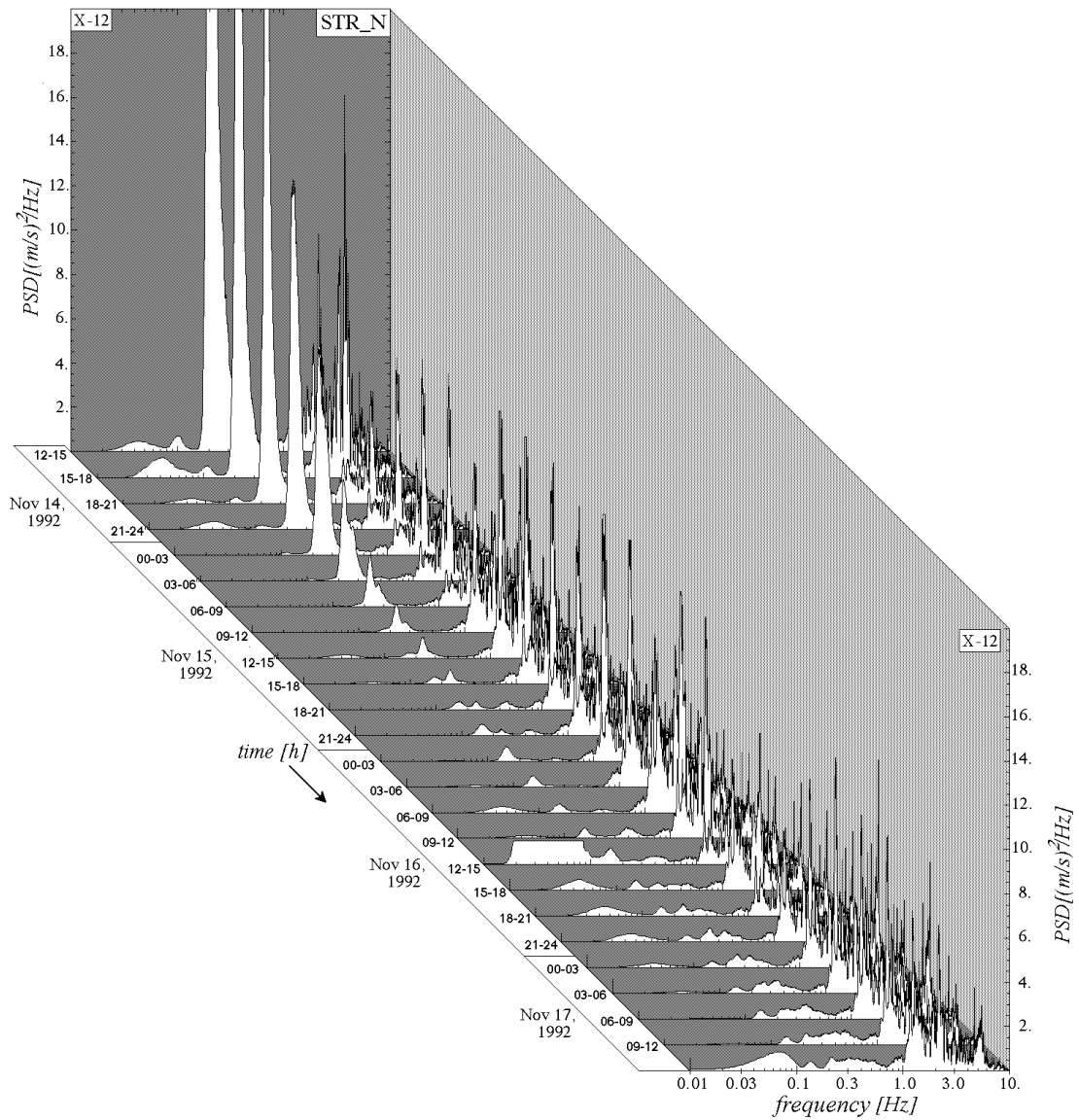
Figure 6.3: *Temporal variation of the Power Spectral Density calculated for the 74 single-hour records of STR (N-S component).*
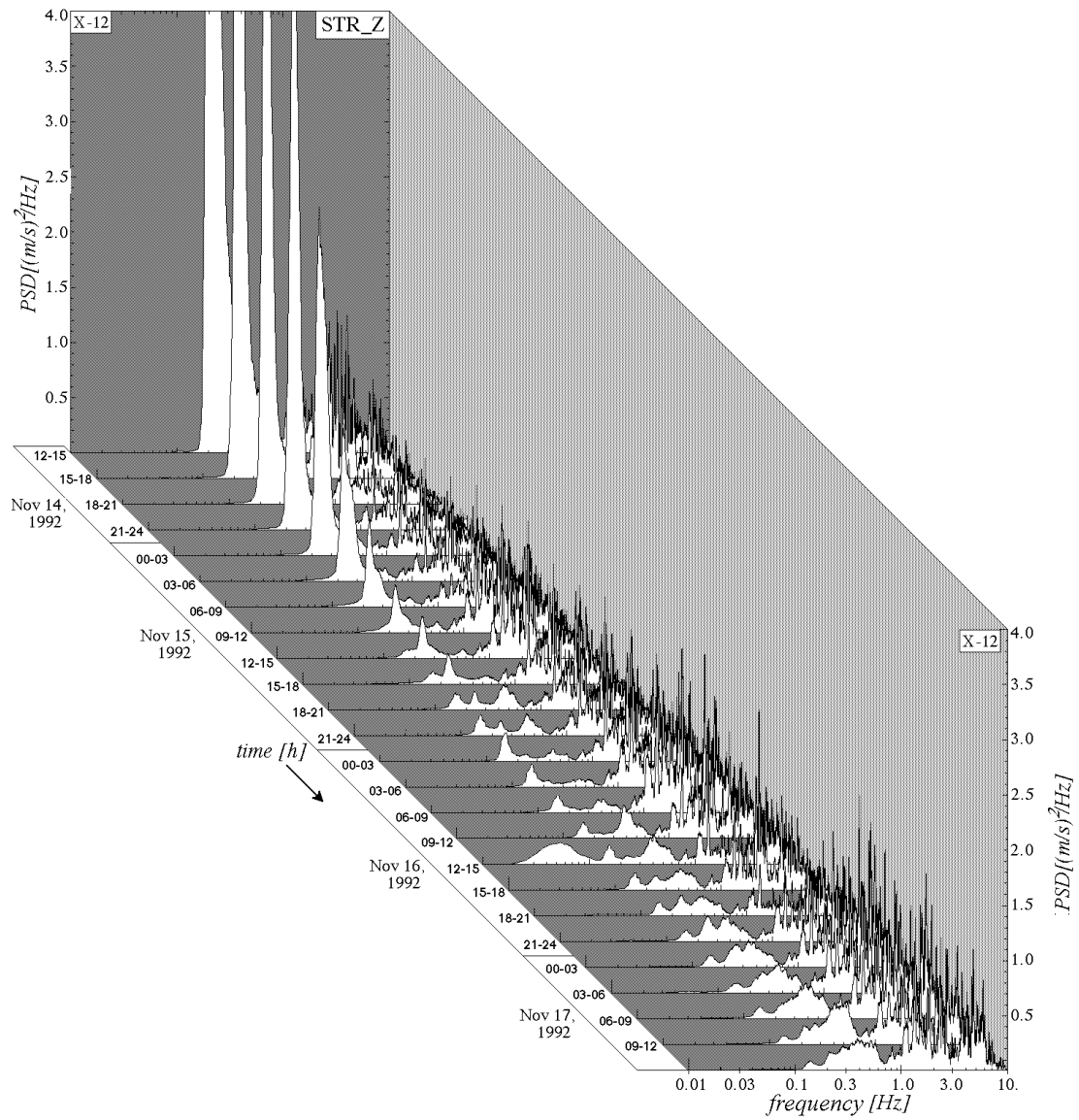
Figure 6.4: *Temporal variation of the Power Spectral Density calculated for the 74 single-hour records of STR (Z component).*

6.2.4 Stationarity of the noise spectra observed at AQU

In order to evaluate which part of the long-period energy in Strombolian tremor spectra is caused by OMS, the noise spectra of the correspondent period have been analysed for the seismic broadband station (AQU). Surprisingly, the temporal variations of power spectra calculated for station AQU show a similar behaviour as found for station STR, even if the differences between the single components is less marked. For this reason only the PSD of the E-component are plotted (figure 6.5).
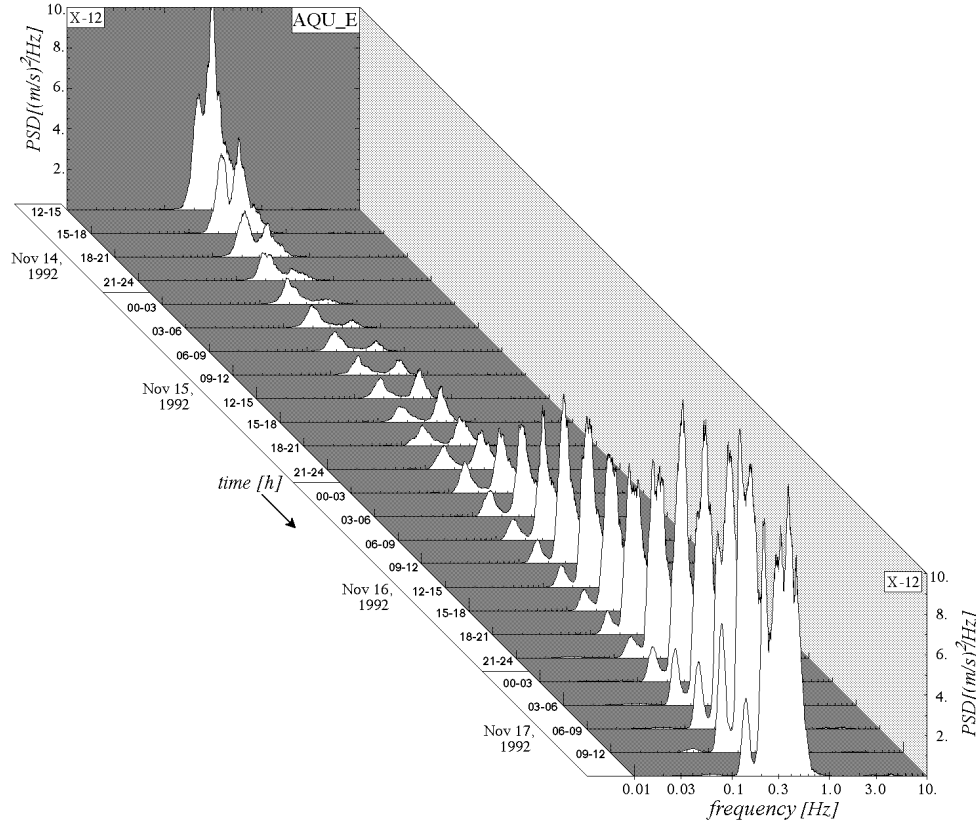
Figure 6.5: *Temporal variation of the Power Spectral Density calculated for the 74 single-hour records of AQU (E-W component).*

The most significant difference with respect to the power spectra calculated for STR is the strong increase of the spectral energy in continuously broadening frequency band around 0.3 Hz on November 16, 1992 and November 17, 1992. Another aspect common to the two stations is the continuous decrease of the spectral energy at 0.21 Hz during the first 36 hours, which does not stop but shifts slightly in frequency to a final value of 0.15 Hz (figure 6.7).

6.2.5 Comparison of the frequency variations

In order to compare quantitatively the temporal energy fluctuations recorded at AQU and STR, the observed frequency variations have been replotted in an enlarged scale. Figures 6.6 (STR) and 6.7 (AQU) are tripartite plots, where the external parts show in a log-log scale the power spectra of the E-component (left) and the vertical component (right). The lines in the central graph connect schematically the significant power spectral peaks identified in the external plots.
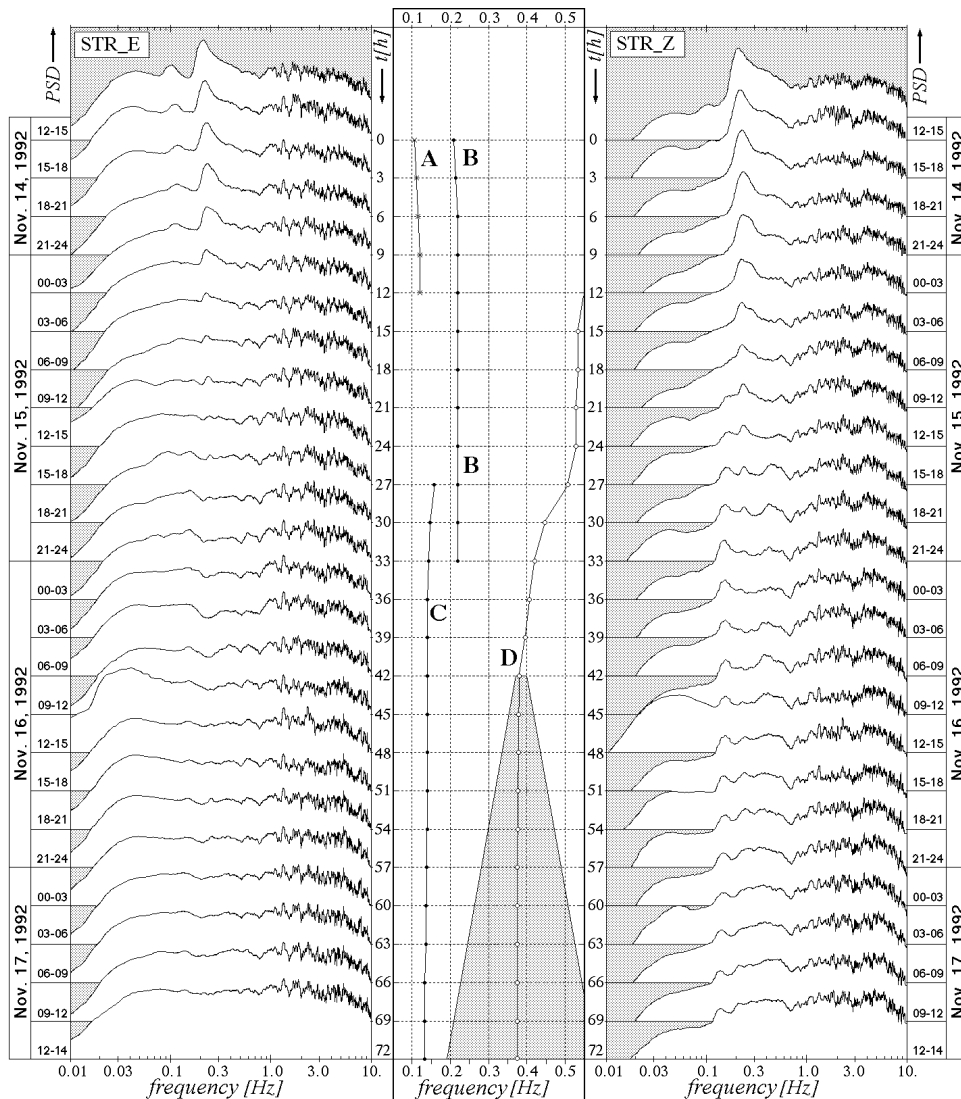
Figure 6.6: *Station STR: temporal variation of the significant long-period peaks (centre); PSD (double logarithmic scale) for the E-component (left) and the Z-component (right).*

In order to better distinguish the temporal variations of the peak frequencies, which concern only the very narrow frequency band between 0.1 – 0.5 Hz, a linear frequency scale was chosen for the central graph. The time scale (top to bottom) reaches from $t = 0\ h$ (November 14, 1992, 12:00 – 15:00 UTC) to $t = 72\ h$ (November 17, 1992; 12:00 – 14:00 UTC).
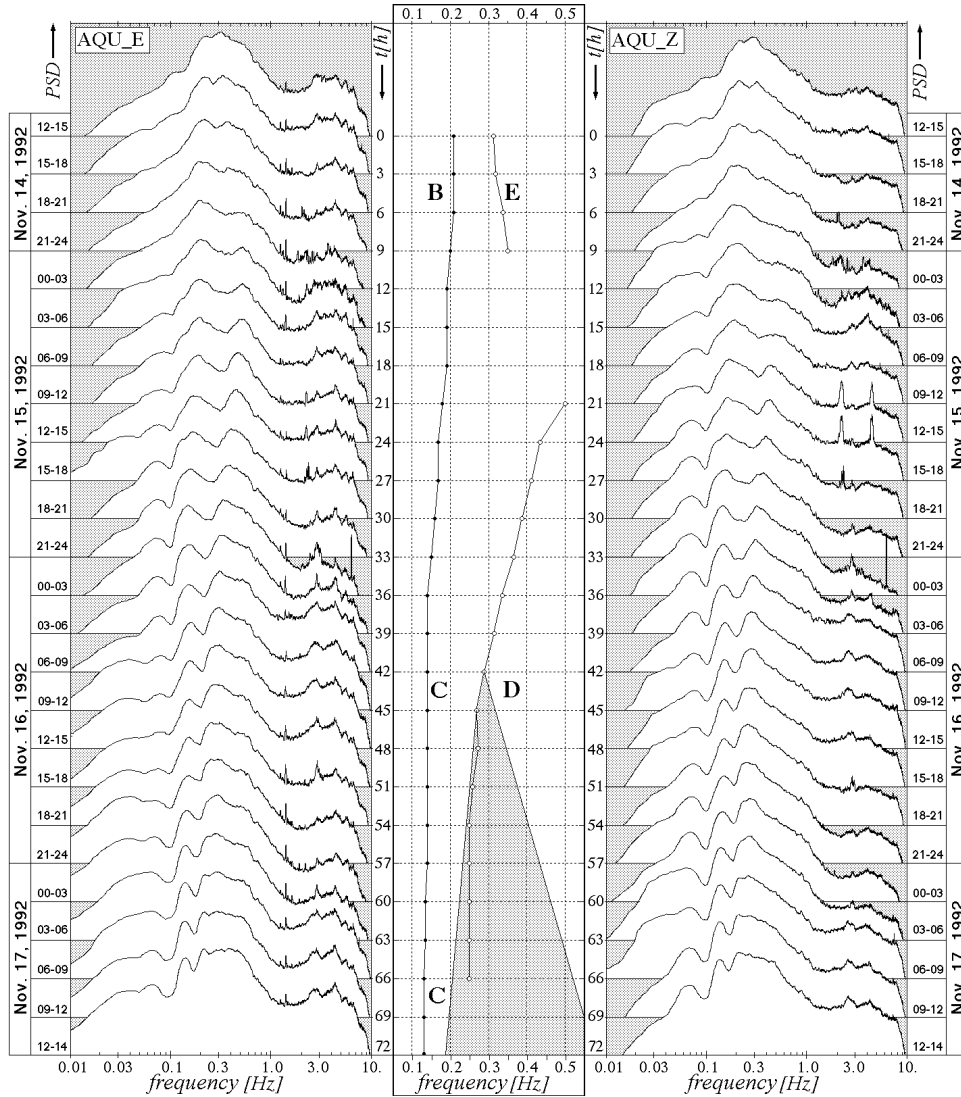
Figure 6.7: *Station AQU: temporal variation of the significant long-period peaks (centre); PSD (log-log scale) for the E-component (left) and the Z-component (right).*

During the second half of November 15, 1992 the formerly mentioned frequency shift from 0.21 Hz (**B**) to 0.14 Hz (**C**) can be observed at both stations. At AQU this frequency shift occurs continuously, whereas in the power spectra recorded at STR after approximately 30 hours the peak at 0.14 Hz is properly *switched-off* and at the same time the 0.21 Hz peak becomes *switched-on*. Moreover, the occurrence of a spectral energy at 0.21 Hz is accompanied by the appearance of a gradually broadening spectral peak at $\approx 0.3 \ Hz$ (**D**). This can be well observed also at station AQU: contemporaneously to the *fade-out* of the 0.21 Hz peak and the *fade-in* of the 0.14 Hz peak, significant spectral energy occurs in a relatively broad frequency band around 0.3 Hz (**D**). Significant spectral energy at 0.105 Hz (**A**), recorded during the first 12 hours at STR (figure 6.7) is missing in the corresponding power spectra calculated for AQU. On the other hand the spectral peak **E** observable at AQU during the first 9 hours, does not occur in power spectra of STR.

6.3 Analysis of non-seismic data

6.3.1 Meteorological data

In order to better evaluate the contribution of the OMS to the long-period seismic energy in the Strombolian tremor spectra, external influences like the weather dynamics were considered. Figure 6.8 shows the maps of the isobars with the positions of the cyclones (T_1, T_2) and the corresponding front systems (1. and 2.) for Central Europe and Italy during the period of interest (November 14 – 17, 1992)

Data of the meteorological parameters wind direction, wind velocity and atmospheric pressure recorded at different Italian stations (Florence – FI, Messina – ME, Ustica – US) and the sea level variations are plotted in figure 6.10. The corresponding time specifications are given in Central European Time (CET). The weather charts of November 14, 1992 are dominated by a low-pressure area (T_1), situated at 00:00 above Central Italy which moved during the following hours towards East (06:00 Croatia; 12:00 Bulgaria). The associated cold front migrated from North to South reaching in the morning of November 14, 1992 the North coast of Sicily.

This transition of the first cold front can be already noticed in the atmospheric pressure data of Florence on November 13, 1992. Figure 6.10 shows, that the atmospheric pressure reached its minimum value at 18:00, followed by a short lasting change of wind direction to the North and a contemporary increase of seismic noise level (figure 6.9). About 12 hours later this cold front reached the North coast of Sicily. Strong winds from the North were reported from Ustica and Messina with peak velocities from 60 km/h (US) to 80 km/h (ME). While the first cold front continued to migrate towards South (November 14, 1992; 12:00 South of Malta) during November 14, 1992 an anticyclone reached Italy from NW, and remained stable also on November 15, 1992. There is a noticeable time delay between the air-pressure recorded at FI and ME and the change of wind direction towards South (figure 6.10).

On November 16, 1992 a second cold front (T_2), belonging to a British Channel cyclone, migrated from the West towards Italy. Continuous decrease of the air-pressure at FI and ME figure 6.10 and the sudden increase of the seismic noise level (figure 6.9) suggest the approaching cold front. On November 16, 1992 T_2 reached Corsica and Sardinia at about 12:00 and the line FI – Palermo on November 17, 1992 at 06:00. T_2 is immediately followed by a third Eastwards moving cold front, belonging to a further cyclone situated on November 16, 1992 12:00 on the British Islands (T_3) (figure 6.8).
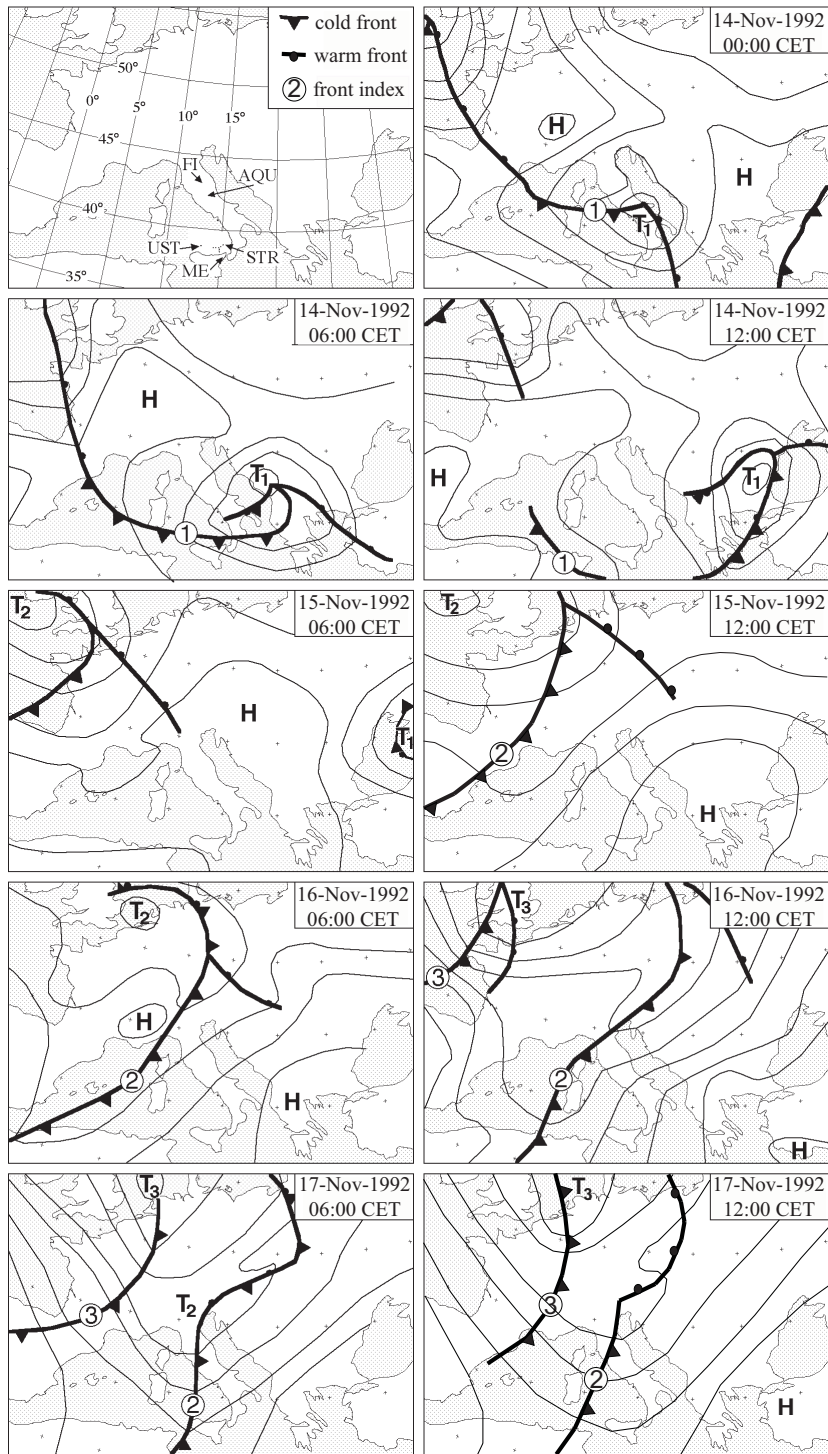
Figure 6.8: *Evolution of the meteorological situation in Europe for the period November 14 – 17, 1992.*

6.3.2   RMS-value of the seismic noise

The comparison of the temporal air-pressure variations with the seismic RMS-values show an inverse proportionality. The RMS-value recorded at Florence increases, when the air-pressure decreases (figure 6.9). Considering the corresponding time shift, the same correlation can be found between the RMS-value at AQU and STR and the air-pressure recorded at ME (figure 6.9). Unfortunately the seismic recording period (AQU, STR) lies exactly between the cold front passages of T_1 and T_2 (figure 6.9) and hence the maximum RMS-values may be found outside the recording period. It is worthwhile to note that at STR the RMS-values are much higher during strong winds from NW (T_1), rather than during the passage of T_2 with winds from SW. However, station AQU shows during times of low-pressure comparable RMS-values.
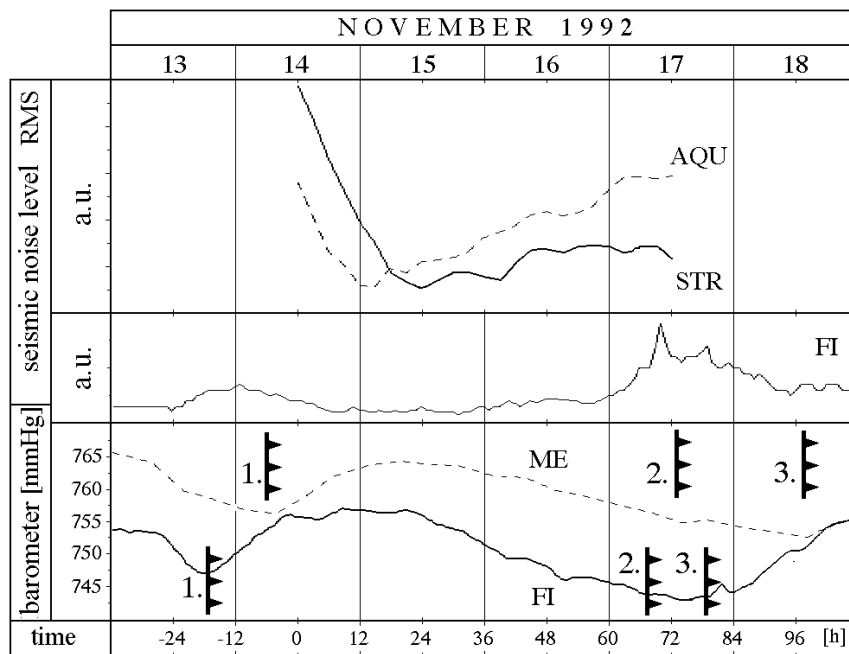
Figure 6.9: *Mean seismic noise level (RMS) for stations AQU, STR, FI and barometric pressure (ME, FI) at November 1992.*

6.3.3   Mareographic data from station Messina (ME)

For the estimation of the locally generated OMS it is important to consider also the sea level fluctuations caused by meteorological parameters. Unfortunately no corresponding data were recorded near Stromboli during the seismic broadband measurements (November 1992). Therefore recordings of the sea level variations

from the nearest situated harbour Messina (ME) were analysed. Even if data from the harbour of Messina cannot represent the situation at Stromboli – given the small distance – such data can help to provide a rough estimate of the sea level fluctuations in the Southern Tyrrhenian sea.
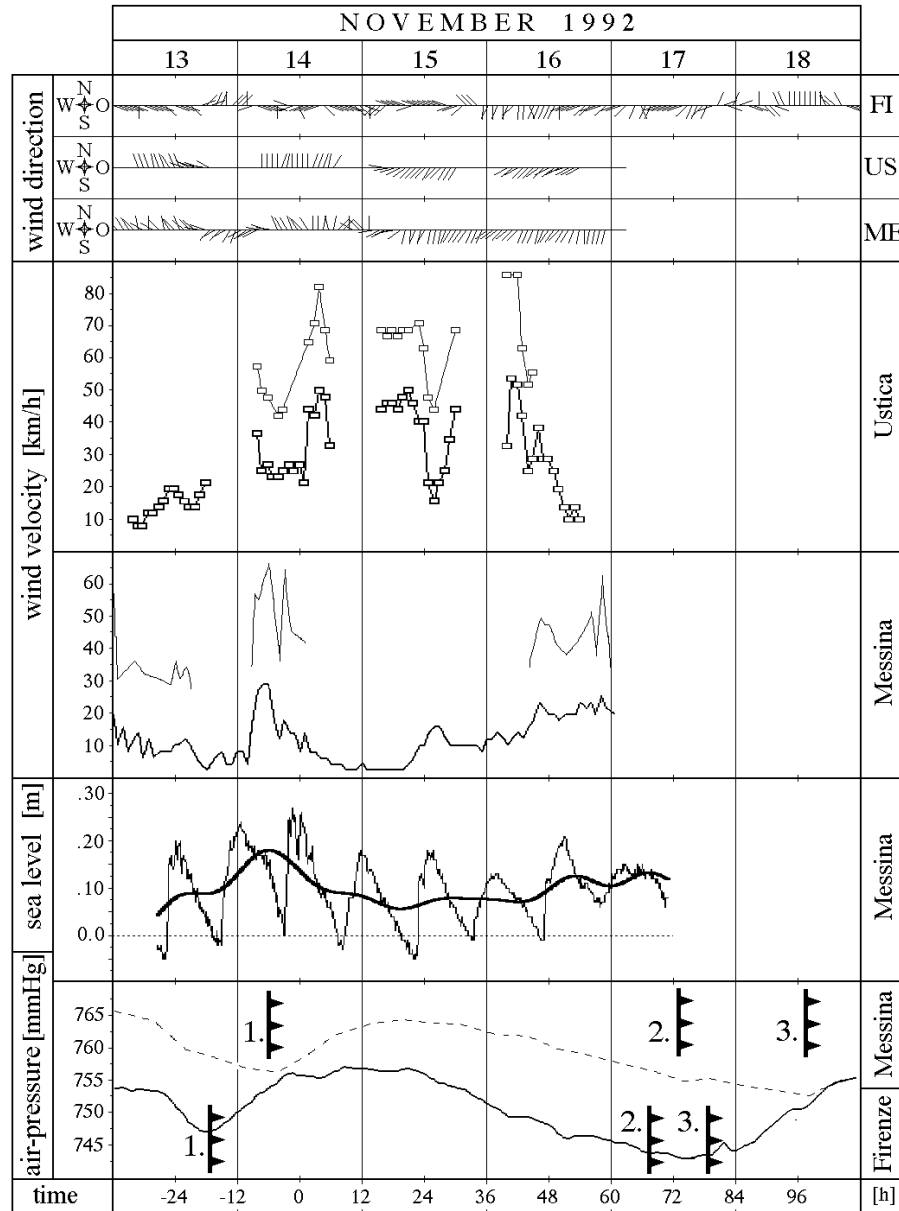
Figure 6.10: *Wind direction (FI, US, ME), wind velocity (US, ME), sea level (ME) and barometric pressure (ME, FI) for the period November 13 – 18, 1992.*

Figure 6.9 shows the absolute variations of the sea level (in m), which are not corrected for the tides. Dominating characteristics of the tide curve are the periods M_2 (lunar) and S_2 (solar). Its asymmetric shape (figure 6.9) is caused by the bathymetry of the Strait of Messina, which resembles more a *river mouth* rather than an open sea. The sea level shows a typical quick swell and a slow ebbing, hence the *flood tide* takes less time, than the *ebb tide*, giving the sea level variations the typical sawtooth shape.

In order to estimate the influence of the wind on the sea level fluctuations, the data has to be corrected for the expected tides. Computer codes, like e.g. ETGTAB *Wenzel* (1994) calculate exactly the theoretical tides of the solid earth as function of the geographical latitude and longitude, but are not able to predict the tides including individual harbour characteristics. Those predictions are extrapolated from long lasting observations. In the case of Messina, due to the sawtooth shape of the tides, the harbour authority publishes only the maximum and minimum values of the predicted sea level (four values per day).

In order to estimate the relative sea level variations, a linear interpolation between the extreme values was subtracted from the data and the residual curve was low-pass filtered at a frequency of $15 \ h^{-1}$. In figure 6.10 the resulting smoothed curve was superposed to the raw sea level data.

The relative maximum of the smoothed graph arises where the largest deviations from the theoretical sawtooth appear in the raw data, i.e. during the first 12 hours of November 14, 1992. This correlates well with the wind velocity recorded at Messina, that reached in the morning of November 14, 1992 mean values of 30 km/h and maximal values of 65 km/h. Similarly to the mean seismic noise level, the highest values of wind velocity are observed during the passage of the cold front from North to South (T_1).

In summary, it can be stated that the comparison of the seismic tremor recorded at Stromboli with the meteorological and mareographic data of the area indicates a strong interaction between the weather dynamics and the long-period tremor data.

6.4 Conclusions

The study of the seismic tremor recorded on Stromboli volcano in the period range between $2-30 \ s$ did not reveal a local volcanic seismic source. On the one hand the main seismic energy is concentrated on the horizontal components, whereby an excitation of the deep seismic source can be excluded. On the other hand, the tremor signals filtered in three narrow filter bands are all recorded by the array as plane waves, further excluding a volcano seismic source. The number of explosion quakes remained more or less constant during the 74-hour recording period, having a mean value of $11-14$ events per hour.

Moreover, several pieces of evidences support the hypothesis that the OMS are responsible for the long-period energy in the power spectra recorded on Stromboli:

- The temporal variation of the spectral content bear a great resemblance with the power spectra calculated at the remote station AQU.

- The comparison of the data with the weather dynamics shows, that the passage of the cold front results also at STR with an increase of the RMS.

At the end of the thirties Italian scientists studied the OMS generated in the Mediterranean. One interesting result was that the seismic noise increases during significant air-pressure fluctuations, a phenomenon which is primarily observed during the fast passage of a bad weather front.

Caloi (1951) pointed out, that the seismic energy transmission from the atmosphere into the ground is more effective if the velocity of the pressure fluctuation (front passage) is similar to the propagation velocity in the dispersion-free shallow water. *Caloi* (1951) stated – by analysing different weather conditions – that the wind velocity does not influence the amplitude of the OMS. In spite of high wind speed before and after the passage of a cold front, the seismic RMS-value showed an inverse proportionality with respect to the temporal variation of the atmospheric pressure.

The variation of the spectral content of the power spectra depends on the differing source regions, or better on the location of the cyclones. *Caloi and Migani* (1971) published characteristic OMS-periods of different source regions inside the Mediterranean, in particular seismic energy at a period of 5 s ($\approx 0.2\ Hz$) is generated within the Tyrrhenian Sea, while energy at 3 s ($\approx 0.33\ Hz$) seems to be typical for the Adriatic Sea. Caloi's observations coincides very well with the present data analysis.

On November 14, 1992 the first cold front was situated over the Tyrrhenian Sea and migrated quickly from North to South. Accompanied by high wind speeds and swell the passage of the bad weather front was recorded seismically by high spectral energy at 0.21 Hz ($T = 4.8\ s$). The highest amplitudes were found at the island station STR – lower spectral amplitudes were observed a the continental station AQU. Compared to AQU, *Peak* **A** is recorded at STR with seismic energy ten times higher. However, the spectral power of *Peak* **C** at STR reaches only a third of the spectral power found at AQU. *Peak* **B** is recorded at both station with comparable spectral energy.

The following *ridge* of high pressure can be noticed in the power spectra by a slight decrease of the energy. At the end of the registration period a low-pressure area was located near the Northern Adriatic Sea, recognizable by seismic spectral energy at 0.33 Hz ($T = 3\ s$), with higher amplitudes at AQU.

The frequency peak at 0.14 Hz recorded at AQU and STR is undoubtedly correlated with the OMS. Following *Longuet-Higgins* (1950) on the origin of OMS, the 0.14 Hz peak seems to be the corresponding PF-band of the 0.3 Hz peak.

The long-period spectral energy in a frequency band between $0.03 - 0.3\ Hz$ is generated exclusively by the OMS. The temporal variation of the main frequencies recorded at both stations are too similar to be generated by a significant contribution of volcanic activity.

Chapter 7

Seismic broadband array

Abstract   An array of nine three-component broadband seismometers was deployed in two different configurations on Stromboli volcano. The analysis of the seismic wavefield related to volcanic explosions revealed some observations which offer a completely new insight into the dynamics of a volcano. These new observations are restricted to the low-frequency range below 1 Hz and underline, therefore, the superiority of broadband recordings over conventional short period observations. Surprisingly simple wavelets indicate an initially contracting source mechanism. Gas-jets, that could not be seen in a short-period seismic record at all, generate a clear dilatational wavelet in a broadband recording suggesting the same contracting source mechanism. The analysis of particle motion and seismic array techniques permits a location of the seismic source. We find low-frequency signals of 3 s and 6 s periods that are not related to eruptions and do not share a common source with the eruption-related events. A video recording of visible volcanic activity at the crater region allows one to correlate precisely eruptive features with seismic signals.

7.1   Introduction

Stromboli volcano, located north of Sicily, is a popular target amongst Earth scientists for several reasons. Its continuous activity provides some 10 explosions per hour and the crater region is easily accessible. Several short-term seismic experiments have been carried out (e.g. *Lo Bascio et al.* (1973)) some of which also used seismic arrays and a few research groups run a permanent seismic station (*Falsaperla and Neri* (1986)) or a seismic network (*Napoleone et al.* (1993)). In

addition some attempts have been made to determine the amount and velocity of gas-jets and ejecta as a function of time (*Chouet et al.* (1974); *Ripepe et al.* (1993)).

A crucial drawback of the majority of seismic investigations carried out on Stromboli, but also on other volcanoes so far, is their restrictions to a frequency band above 1 Hz. This was simply due to the unavailability of broadband seismometers. Such instruments have been used only recently in pilot studies at Stromboli (*Brüstle et al.* (1993)) and Sakurajima (*Kawakatsu et al.* (1992)), but in both cases only a single seismic station. Here we use an array. In the following we refer to the part of the spectrum below 1 Hz as being "long period" signals, in contrast to *Chouet* (1992) who uses the term to describe a class of magma flow related events with signals around 1 Hz.

7.2 Seismic experiment

The new approach in our experiment was to combine seismic array techniques with broadband seismometry. We deployed nine Guralp CMG3T seismometers in two configurations as depicted in Figure 7.1. The data were recorded on Lennartz MARS-88/OD seismic recorders with a sampling frequency of 62.5 Hz and a dynamic range of 120 dB. This results in an observed frequency range from 0.03 Hz
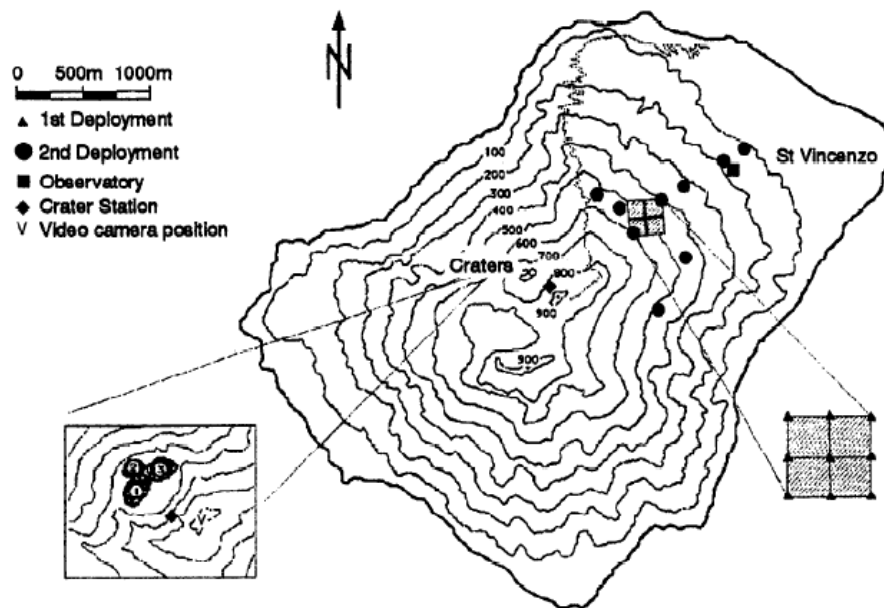
Figure 7.1: *Map of Stromboli volcano with the two seismic deployments, the short-period crater station, and the location of the video camera.*

(30 s period) to a 25 Hz after application of an anti-aliasing filter. All seismic
stations were equipped with a GPS time signal receiver. The first deployment
(Figure 7.1) was designed to study the short period part of the wavefield; the dis-
tance between adjacent stations was 100 m and provided coherent signals across
the array up to 1.3 Hz.

The second deployment aimed at the long-period part of the wavefield, the
location of the seismo-volcanic source, and the detection of possibly long-period
tremor. The signals recorded at two adjacent stations some 400 m apart are
coherent to 2 s period. We recorded in the first and second deployment for 4 and
5 days, respectively.

During the experiment three craters were active, displaying different types of
eruptive activity. We refer to these craters in the following as crater #1, #2, and
#3 counted from South to North (Figure 7.1). Crater #3 displayed continuous
low level activity comprising burning gas and very few ejecta interrupted by short
and violent explosions generating narrow lava fountains up to 150 m high. The
eruptive activity at crater #2 can be characterized by strong gas-jets with only
few ejecta lasting about 5 to 10 s. Crater #1 showed explosions with ash clouds
and a broad lava fountain, lasting up to 5 s.

In order to relate the visible eruptive activity to the seismo-volcanic signals
in a quantitative way we deployed a video camera with GPS time signal at the
summit overseeing all active craters (Figure 7.1). For both deployments five hours
of video coverage were achieved. In addition we used a three-component short
period seismometer (Mark L4) which is part of the permanent seismic network of
the Earth Science Department at Florence University. It is installed only a few
ten meters from the craters and was used to relate the active crater to a recorded
seismic event for the time without video coverage. The particle motions could be
used to distinguish between crater #1 and #3, while the gas jets of crater #2 did
not produce any short-period seismic signal at all.

7.3   Short period seismic wavefield

The spectra in Figure 7.2 give an overview of the wavefield comprising time sections
of seismic background and eruption-related event as recorded at a distance of 1500
m from the craters. This demonstrates that an essential part of the seismic signal
is composed of frequencies below 1 Hz. The comparison of spectra of different
events at one station and spectra of one event at different stations demonstrates
that the signals are increasingly dominated by the structure through which they
propagate as on goes to higher frequencies. The signals show a wide variety of
features which differ from event to event and station to station. Particle motion
analysis reveals elliptical trajectories, which indicates that the wavefield above
1 Hz consists mainly of surface or other guided waves as the distance from the
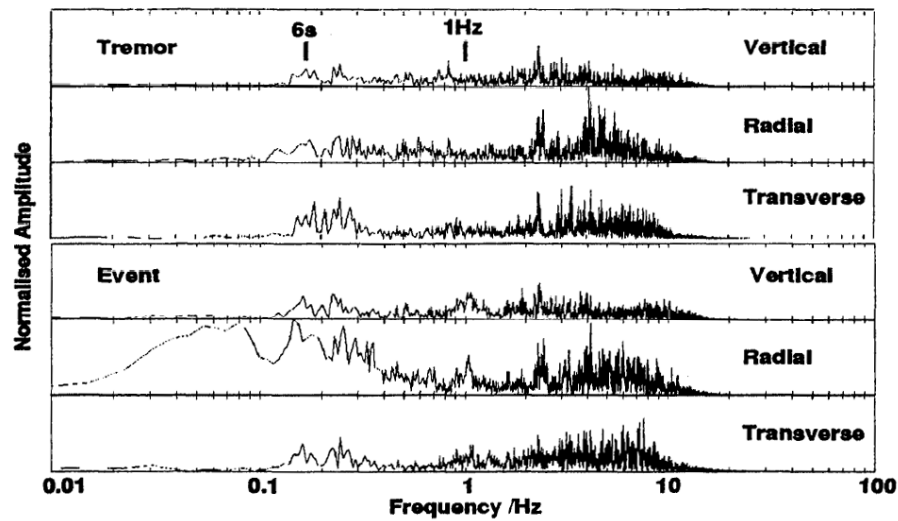
Figure 7.2: *Normalised amplitude spectra of a 2 minute seismic record, vertical and radial components, containing tremor and a seismo-volcanic event related to crater #1; the record was obtained at a distance of 1500 m from the crater region. Note the consistent peaks at 1 s and 6 s period for both the shock and the tremor.*

craters increases. In some cases the frequency range above 3 Hz can be further complicated by a ground-coupled air wave (*Braun and Ripepe* (1993)). An automated beamforming and particle motion analysis method of *Mao and Gubbins* (1995) has been used to determine the angle of incidence and azimuth of the seis-
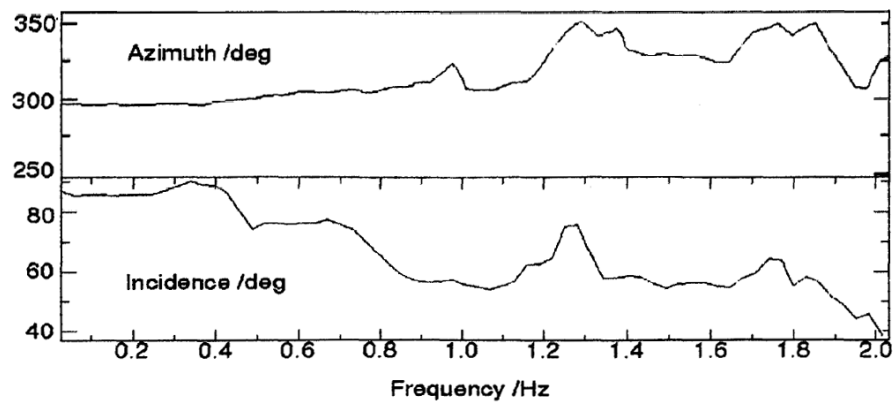
Figure 7.3: *Azimuth and angle of incidence for different frequency bands show strong variations above 0.4 Hz; record from the southernmost station, 1 km east of the craters.*

mic wavefield for various frequency bands. The results, presented in Figure 7.3 for a 32 s time window of a event related to an eruption at crater #1, indicate a stable range up to 0.4 Hz and a growing directional variation of the seismic wavefronts as the frequency increases.

An extensive treatment of the wavefield obtained by the first (small) deployment is the subject of a separate study. As high frequency signals on Stromboli show no spatial coherence it can here been stated that high frequency signals are masked by path effects to such an extent that it is not possible to link them directly to the volcanic source mechanism. This feature is, however, very different for broadband recordings.

7.4   New long-period source characteristics

In order to demonstrate the advantages of seismic broadband recordings over conventional short-period records the following comparison has been carried out: Figure 7.4 shows the radial component of a seismic signal associated with an eruption from crater #1 and recorded at the southernmost station of the second deployment (Figure 7.1). A short-period record (b) is simulated by high-pass filtering
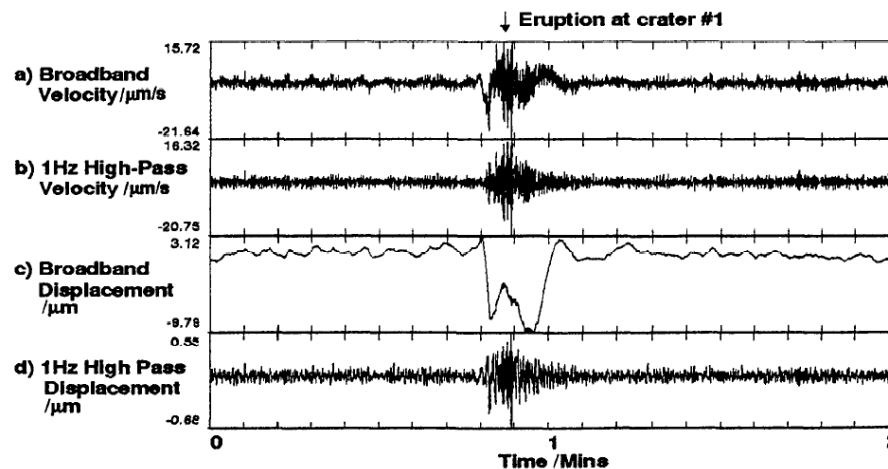
Figure 7.4: *Comparison between broadband (a) and simulated short-period (b) velocity seismograms (E-W) and displacement (c,d) for an eruption at crater #1; (b) represents the conventional seismic record on a volcano. The broadband displacement (c) shows a surprisingly simple wavelet compared to the short-period trace (d). The line indicates the onset of the eruption as determined by the video record.*

the broadband signal (a). This is what one would see with a commonly used 1 Hz-seismometer. Integrating both traces (a) and (b) provides the broadband and short-period displacements (c) and (d), respectively.

The short-period displacement (d) with its emergent onset does not show any distinctive features which would shed any light on a possible source mechanism. The broadband trace (c), however, reveals a clear, several seconds long, double-pulsed, displacement towards the source, which is composed of frequencies too low to be detected by a 1 Hz-seismometer. If an isotropic source is assumed then this signal portrays a source with an initially contracting rather than expanding mechanism.

The gas-jets from crater #2 exhibit a different seismic signature as seen in Figure 7.5 where the traces (a) through (d) correspond to those in Figure 7.4. Here, the eruption cannot be detected in the short-period record (d) at all, but is
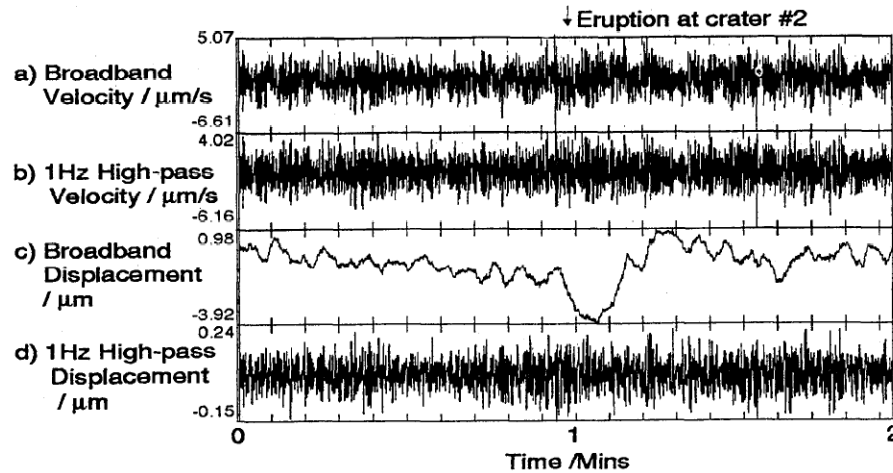
Figure 7.5: *Same as in Figure 7.4, but for a gas-jet from crater #2. Note, that the eruption is not detectable at all in the short-period displacement (d).*

clearly represented in the broadband signal (c). Again, the single-pulsed wavelet (d) indicates a contracting source which shows, however, significantly different features compared to events related to crater #1. In fact, after "calibrating" the seismic record by relating the waveforms to a particular type of eruption as seen on the video, the active craters could be identified throughout the entire seismic record just by looking at the waveforms. A test of waveform identification using the video footage resulted in a confidence level of 90%. Some examples are depicted in Figure 7.6. The time of the visible eruption at the crater, as determined by the video record, is delayed by approximately 3 s compared to the onset of the seismic signal.

Due to their long-period character these signals are not affected by the short-wavelength stratigraphy typically seen on a volcano. They are P-waves, as determined by the particle motion, and will be the new data base from which to model in full detail the contracting process in the magmatic conduit over several seconds.
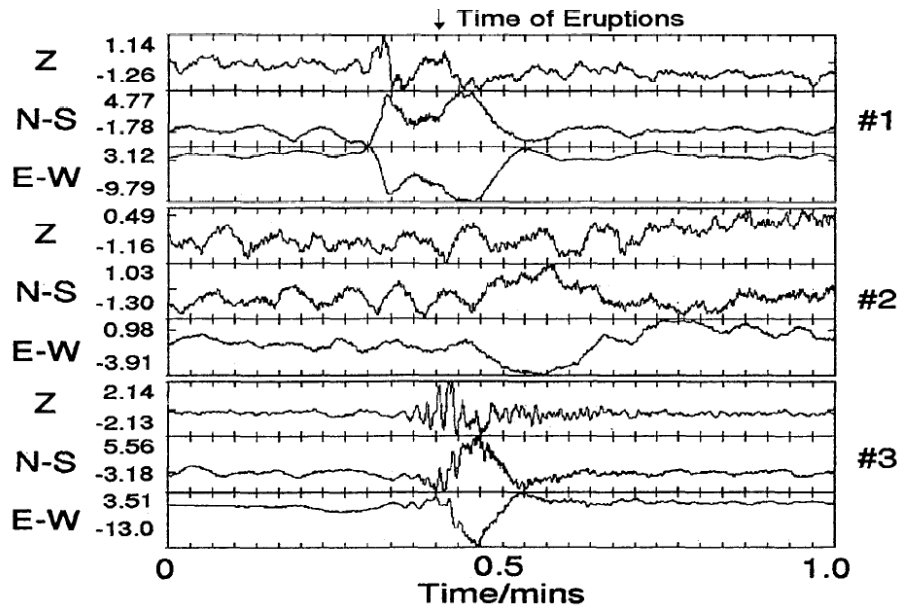
Figure 7.6: *Examples of characteristic displacement waveforms associated with different craters.*

The time difference between the seismic signal and the eruption on video record, as well as the character of the eruption will provide additional constraints to the modelling process.

7.5 Source location

While some long-period source characteristics can be studied with a single seismic broadband station, array techniques comprising beamforming, particle motion analysis and matched filter methods are used to determine the source location. In order to assure the use of direct P-waves for the analysis of particle motion a low-pass filter was applied with a cut-off frequency of 0.1 Hz, safely below the range where directional stability breaks down. The direction of particle motion for the seismic stations in the second deployment (Figure 7.1) are depicted in Figure 7.7. Azimuths and angles of incidence are in good agreement with the results of beam-forming and indicate a source region, vertically ranging from approximately 100 m to 600 m below the crater region. All epicentres fall in an area northwest of the craters (Figure 7.7) and do not show any significant variation with respect to the specific crater where the associated eruption occurs. This is in good agreement with *Del Pezzo et al.* (1992) and indicates, within the limits of our azimuthal coverage of 55°, a confined source region common to all craters.
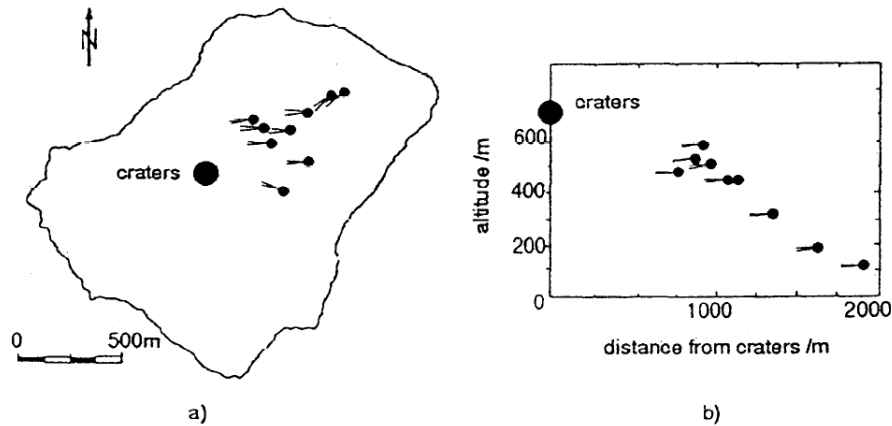
Figure 7.7: *Plane view (a) and vertical cross section (b) of Stromboli with seismic stations (full circles) in the second deployment. The particle motions on (a) point to the source region northwest of the craters; (b) indicates a source region ranging from 100 m to 600 m altitude.*

7.6 Long-period volcanic tremor

The seismic background noise on a volcano may contain signals originating from a continuously active volcanic source and is, therefore, often referred to as volcanic tremor.

The more specified "harmonic tremor" is characterized by a stationary strongly peaked spectrum. We did not observe harmonic tremor on Stromboli but found more complicated spectra (Figure 7.2) that do not show consistent similarities for frequencies higher than 1 Hz, either for one time section recorded at different stations or for different times at a single station. The long-period background signal, as shown in Figure 7.8, exhibits spatial coherency across the entire array and, therefore, indicates a common source.

Previous studies on Stromboli proposed a common source for eruption-related seismic events and volcanic tremor. In order to investigate this hypothesis for low frequencies, particle motion analysis of the bandpass-filtered signals for the dominant spectral peaks at 3 s and 6 s period were used to determine the angle of incidence and azimuth of the corresponding wavefield. Both angles vary with time, and when traced back, do not coincide with the source location for the seismo-volcanic events depicted in Figure 7.7. We therefore conclude that, if these long-period wavetrains are genuine volcanic signals at all, they originate from a source different than the one for the eruption-related events. We suspect these signals are caused by a combination of ocean- and wind-related noise.
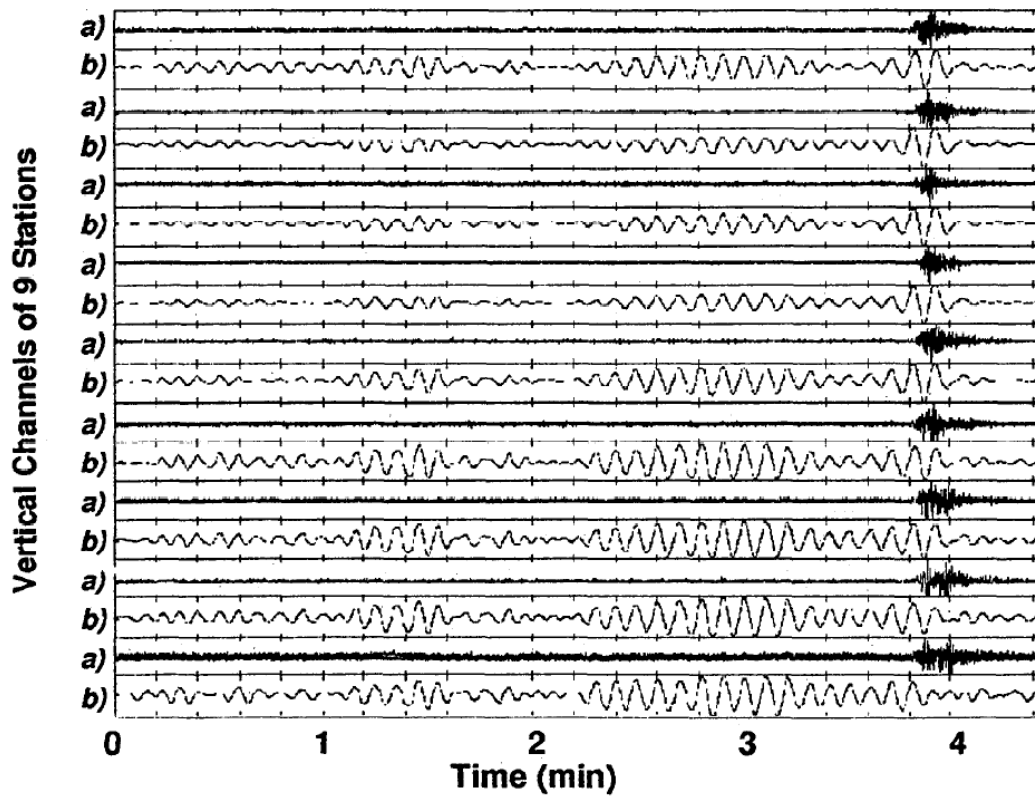
Figure 7.8: *Unfiltered velocity seismograms (a) and bandpass filtered [5 s – 10 s] traces (b) for all the stations of the second deployment. The traces are arranged in order of increasing distance from the craters. The bandpass filtered traces show highly coherent wavetrains not related to eruptions.*

7.7   Conclusions

The results presented indicate that seismo-volcanic events on Stromboli are composed of signals in a very broad frequency range. We demonstrate that using short-period seismic equipment discloses only a small portion of seismic information, which is dominated by surface and other guided waves and cannot be directly linked to the seismo-volcanic source. In many cases events related to an eruption cannot be detected at all. In terms of source modelling the implication is that, even for spatially coherent short-period data, the source can be only partially modelled. Source models based on data lacking spatial coherency reflect path effects rather than source characteristics.

With broadband seismometers, however, we find a surprisingly simple wavelet showing ground motion towards, rather than away from the crater region. It is significantly different for gas jets and lava fountains. We interpret the onset of

these wavelets towards the source a few seconds ahead of the eruptions as an abrupt pressure reduction, possibly caused by movement of fluid through a narrow section of the magma system. This reduction triggers the expansion of the gas-fluid system and leads to the eruption.

A refined model of the source model constrained by the observed wavelets and the video recording is the subject of a subsequent publication.

Chapter 8

The April 5, 2003 paroxysmal eruption

Abstract   On April 5, 2003, one of the largest eruptions in the last decades was observed at Stromboli volcano, Italy. The eruption occurred in a period of increased volcanic activity, following a first explosion in December 2002, which interrupted the typical moderate "Strombolian" behaviour. We present an exhaustive analysis of the available broadband seismic data and relate them to the observed eruption phases. Prominent features of the seismic signals include an ultra long period signal starting a few tens of seconds prior to the explosive eruption as well as a strong energetic signal a few seconds after the onset of the eruption. Both signals are not exactly synchronized with the other geophysical observations. We present a detailed study of those signals using spectral and particle motion techniques. We estimate eruption parameters and seismic source characteristics by different inversion approaches. Results clearly indicate that the paroxysmal eruption was triggered by a shallow slow thrust-faulting dislocation event with a moment magnitude of $M_w = 3.0$ and possibly associated with a crack that formed previously by dike extrusion. At least one blow-out phase during the paroxysmal explosion could be identified from seismic signals with an equivalent moment magnitude of $M_w = 3.7$ and is represented by a vertical linear vector dipole and two weaker horizontal linear dipoles in opposite direction, plus a vertical force.

8.1   Introduction

Stromboli volcano is one of the most active and deeply studied volcanoes on earth. The volcano is located in the North-eastern edge of the Aeolian archipelago in the southern part of the Tyrrhenian Sea, about 55 km offshore from the Italian coasts of Calabria and Sicily. The summit of Stromboli Island reaches an altitude of 924 m a.s.l., even if the volcano edifice rises up to a height of nearly 3000 m with respect to the seafloor. The three main craters are located SW of the summit, at about 700 m a.s.l. North-west of the craters, a steep slope, named *Sciara del Fuoco* (SDF), drops steeply down to approximately 1700 m below sea level (*Romagnoli et al.* (1993)). The SDF is known to be continuously sliding. It has been at the origin of several subareal and submarine landslides in historic and prehistoric times. The last slide occurred on December 30, 2002. The volcanic activity at Stromboli is better known from the frequent occurrence of moderate explosions, a behaviour known as "Strombolian", which has a typical rate of 3 to 10 events per hour (*Chouet et al.* (1974)). This behaviour is occasionally interrupted by the occurrence of major eruptions, often accompanied by lava flows reaching the sea along the SDF. Since the last eruption in 1985, Stromboli showed its typical moderate and persistent eruptive activity, which was interrupted on December 28, 2002, by a large explosion. This unexpected eruption was followed by lava flows, starting from different fissures located approximately 300 m below the crater terrace. After 3 months, the lava supply decreased more and more, but the typical Strombolian activity did not restart. On April 5, 2003, finally a paroxysmal explosion occurred, the largest one since September 11, 1930, and the only one recorded simultaneously by such a multitude of different scientific instruments.

The present paper focuses on the event, which started on April 5, 2003, 07:12 UTC, and which occurred at the end of the 4-month eruption period. After a short overview of the crisis chronology and results available from other authors, we present the available seismic data, discuss their main characteristics and derive a model able to explain the eruption dynamics and the seismic source.

8.2   Overview on chronology and geophysical data

The eruption of December 28, 2002, was characterized by the opening of a main NE - SW trending fissure and by the subsequent lava flows toward the SDF slope (*Calvari et al.* (2005)). Two days later, on December 30th, the collapses of portions of the NW flank produced two landslides in the area of the SDF. The slides generated a local tsunami on Stromboli Island with a maximal runup height of about 11 m, causing several damages at the island villages (*Tinti et al.* (2006)). At this time, a new effusive fissure (fissure 1) was observed at about 550 m a.s.l. During the following 2 months, the lava flows descending the SDF were mostly fed by this fissure. The estimated volume of extruded magma was about 6×10^6 m^3 (*Calvari*

et al. (2005)). Occasionally decreased flow rate at this fissure was accompanied by an increased effusive flow rate from a second fissure (fissure 2) that had formed 170 *m* above, at 670 *m* a.s.l., and was first observed on December 30th. The lava flow from fissure 1 was finally interrupted on February 15, 2003. Since that time, the effusive activity was taken over by the upper fissure 2 (*Calvari et al.* (2005)). About 2 months later, on April 5, 2003, a paroxysmal eruption from the summit crater area occurred, starting at craters 1 and 3 (*Calvari et al.* (2006)). During the whole volcanic crisis, from December 2002 and at least until April 1, 2003, the summit conduit, including its three vents at this time, was blocked, as indicated by the cessation of Strombolian activity and the lack of high-temperature events in the crater area from measurements with a thermal camera (*Calvari et al.* (2005)).

Different studies reported a wide set of geophysical data (*Mattia et al.* (2004); *Calvari et al.* (2006); *Rosi et al.* (2006); *D'Auria et al.* (2006)), recorded during the eruptive process of April 5, 2003. The monitoring program included deformation, seismic, gas and infrared measurements, as well as visual observations. GPS data from four stations were analyzed by *Mattia et al.* (2004). Most of the GPS stations were damaged by the April 2003 explosion, and could still be used to identify three different eruptive phases. The observed deformations and uplift prior to the explosive eruption have been interpreted as caused by the slow ascent of a magmatic column in a feeder dike toward the crater area. The general behaviour can be summarized by the ascending or filling of a dike with a dip angle of 55 – 73° and a strike angle of 209 - 215° (sub-parallel to the SDF slope). The authors found also indications that the extension, orientation and opening of the dike slightly changed over a time period of about 45 *s* prior to the explosion.

A different set of information was used by *Rosi et al.* (2006), which describes the visual observations of the climactic explosions and their relation with infrared data from a sensor pointed toward the craters. The interpretation of these data led to the description of four phases of the explosive eruption, which correlate only partly with those defined by *Mattia et al.* (2004).

The first eruption phase in both studies is identified with the eruption onset. It started at 7:12:33 UTC (time R1), with the emission of red ash from two of the summit vents and later extended to the third one *Rosi et al.* (2006). At exactly the same time, GPS data from station SDIC, located SW of the crater region, measured a movement upward and away from the vents *Mattia et al.* (2004). Eruption phase 2 of *Rosi et al.* (2006) starts about 33 *s* later at 7:13:07 (R2), when the onset of the infrared thermal signal is observed, also associated with ash emission. The beginning of this phase is also marked by a change in the deformation direction, which has been modelled by a loss of pressure in the feeder conduit (*Mattia et al.* (2004)). However, the GPS-based onset of eruption phase 2 starts about 2 *s* earlier (7:13:05). Visual observations during phase 2 indicate the emission of dark ash plumes with jets extending toward NNE. An abrupt increase in the crater temperature at 7:13:20 marks the beginning of a third eruption phase

(R3). Again, the analysis of the GPS dataset puts the onset of this phase 3 s earlier. Inversion of GPS data in the eruption phase 3 led *Mattia et al.* (2004) to conclude that the feeder dike possibly changed its orientation during this phase toward a greater dip (73°) and a lower strike angle (209°). Unfortunately, GPS stations were soon damaged by the explosive fallout and the orientation change is thus weakly constrained. Two seconds after the eruptive phase R3 at 7:13:22 a large climactic explosion (paroxysmal explosion) was observed by video, characterized by the emission of larger ground hugging ash plumes. Observations following the paroxysm indicated that the lava flow from fissure 2 was covered by ejected material from the initial phase of the event, reaching a maximal thickness of about 10 m. Five seconds later at 7:13:27 a powerful blast occurred, with a large increment of the spreading velocity of the cloud (*Calvari et al.* (2006)). During the paroxysmal explosion, infrared pulses and visual observations of large ash plumes indicate at least two other subevents, which have not been resolved in time. According to *Rosi et al.* (2006), a fourth eruption phase (R4) started at 7:13:59, when the activity of the volcano consists mostly of pyroclastic flows and smaller explosions. The onset of phase 4 is also observed by *Mattia et al.* (2004), but again 3 - 4 s earlier (7:13:55).

Comparing the timing of these eruption phases defined in different studies leads to some interesting considerations. First, deformation data always precede the IR signal by 2 - 4 s. Moreover, we observe how, in the cases of the large explosion and the first major subevent, the IR pulses preceded the visual observation of the eruptive pulses and the formation of Phoenix clouds by approximately 3 s (main event 7:13:19 - 7:13:22 UTC, first subevent 7:13:40 - 7:13:43 UTC). This observation suggests that 3 s are needed for the expansion of the climactic plume.

8.3   Seismic data

Seismic records of the April 5, 2003 explosion have been first discussed by *D'Auria et al.* (2006). The authors identified different seismic phases and, although they did not carry out a waveform inversion, they could interpret some data features and propose a reconstruction of the explosion kinematic. The observations start with an ultra long period (ULP) signal, which was identified as precursor of the explosion, and interpreted as consequence of a tilt responding to the volcano deformation during magma ascent and ejection. This signal was followed by three seismic phases, related respectively to the vesciculation process in the volcanic conduit (starting at 7:12:42), the explosion signal (7:13:35), and the falling of ejected blocks and the following landslides (starting at about 7:13:50). The interpretation of the eruption process was finally associated to the ascent of an anomalous gas-rich magma batch (*D'Auria et al.* (2006)).
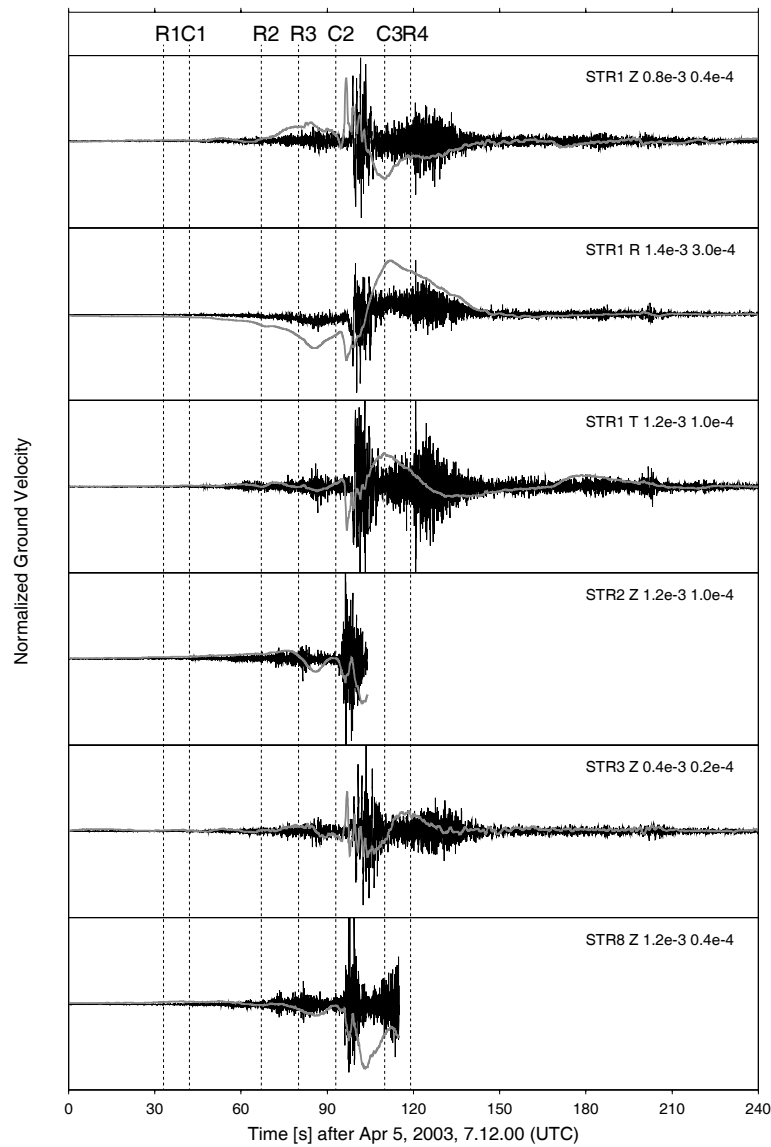
Figure 8.1: *Example of seismograms for the explosion of April 5, 2003. Data correspond to velocity records. Vertical, radial and transversal components for station STR1 are shown in the three upper traces (thin lines). Vertical components for the remaining stations are plotted in the remaining traces (thin lines). Lowpass filtered traces (below 0.1 Hz) are superposed at each component (thick gray lines). Amplitudes are normalized to different values to point out main seismic phases; scaling factors are given at the top right of each trace for the original trace and the lowpass filtered trace respectively. Eruption and seismic phases commented in the text are marked in the figure (dashed lines).*

In this study, we use broadband seismic data from the monitoring network of the INGV, corresponding to stations STR1, STR2, STR3 and STR8, located on the NE flank of the volcanic cone (Fig. 8.3). Station instrumentation consists of a Guralp CMG40T sensor, recorded with a sampling rate of 50 Hz and with a flat instrument response between 0.0188 and 50 Hz. Records from stations STR2, STR3 and STR8 show few clipped samples during the first part of the eruption, which have been extrapolated to reconstruct the main signal. At the time of the paroxysmal explosion, stations STR2 and STR8 were damaged by bombs falling down and signals are useless starting from 7:13:44 and 7:13:55 respectively. Data pre-processing included the mentioned interpolation, correction for the instrument response, high-pass filtering above 0.01 Hz and resampling to 10 Hz.

The obtained ground velocity records show a strong ultra long period signals (ULP) as well as clear seismic phases with sharp onsets and large amplitudes (C1, C2, C3 in Fig. 8.1). The spectrogram for the radial component at station STR1 shows the frequency content of the different seismic phases (Fig. 8.2).

The ULP signal, clearly visible on radial and vertical components below 0.1 Hz, has a dominant period of about 100 s. Although its onset is not sharp, it is evident that the signal starts before the higher frequency seismic phases are observed, preceding the eruption. Owing to the observation of large amplitudes on the horizontal components, with respect to the vertical ones, the signal was interpreted by *D'Auria et al.* (2006) as a consequence of tilt, rather than displacement. The analysis of particle motions indicates that the first motion is linearly polarized at each station toward the source (Fig. 8.3). A similar behaviour has been observed for LP or ULP events at Stromboli (*Chouet et al.* (2003); *McGreger and Lees* (2004); *D'Auria et al.* (2006)).

The first clear seismic onset (C1) is observed at 7:12:42, in agreement with *D'Auria et al.* (2006). The seismic signal following this onset is characterized by the inclusion of high frequencies, up to 4 - 5 Hz. At 7:13:33 (the onset and the following seismic phase will be referred as C2), a large amplitude signal is observed, with dominant frequencies of 0.7 - 1.1 Hz. The signal consists of few pulses and lasts about 10 s. This phase C2 was also observed by *D'Auria et al.* (2006), starting at 7:13:35. Differently from the ULP, signals starting at C1 and C2 do not present a clear linear polarization. Finally, we define a last seismic phase (C3), starting at about 7:13:50. This phase is marked by a progressive increment of the amplitudes, lasts for about 40 s and is also characterized by the higher frequency content; this signal has been associated to the fallout of ejected material (*D'Auria et al.* (2006)).

The identified seismic phases can be compared to the eruptive phases described in paragraph 2. Phase R1 has no clear expression in the seismograms, possibly indicating that the ash venting starts slowly and begins to generate significant seismic signals 10 s later (onset C1). Similarly, phase R2 is not associated to clear seismic onsets, although it roughly corresponds to the increase of low-frequency
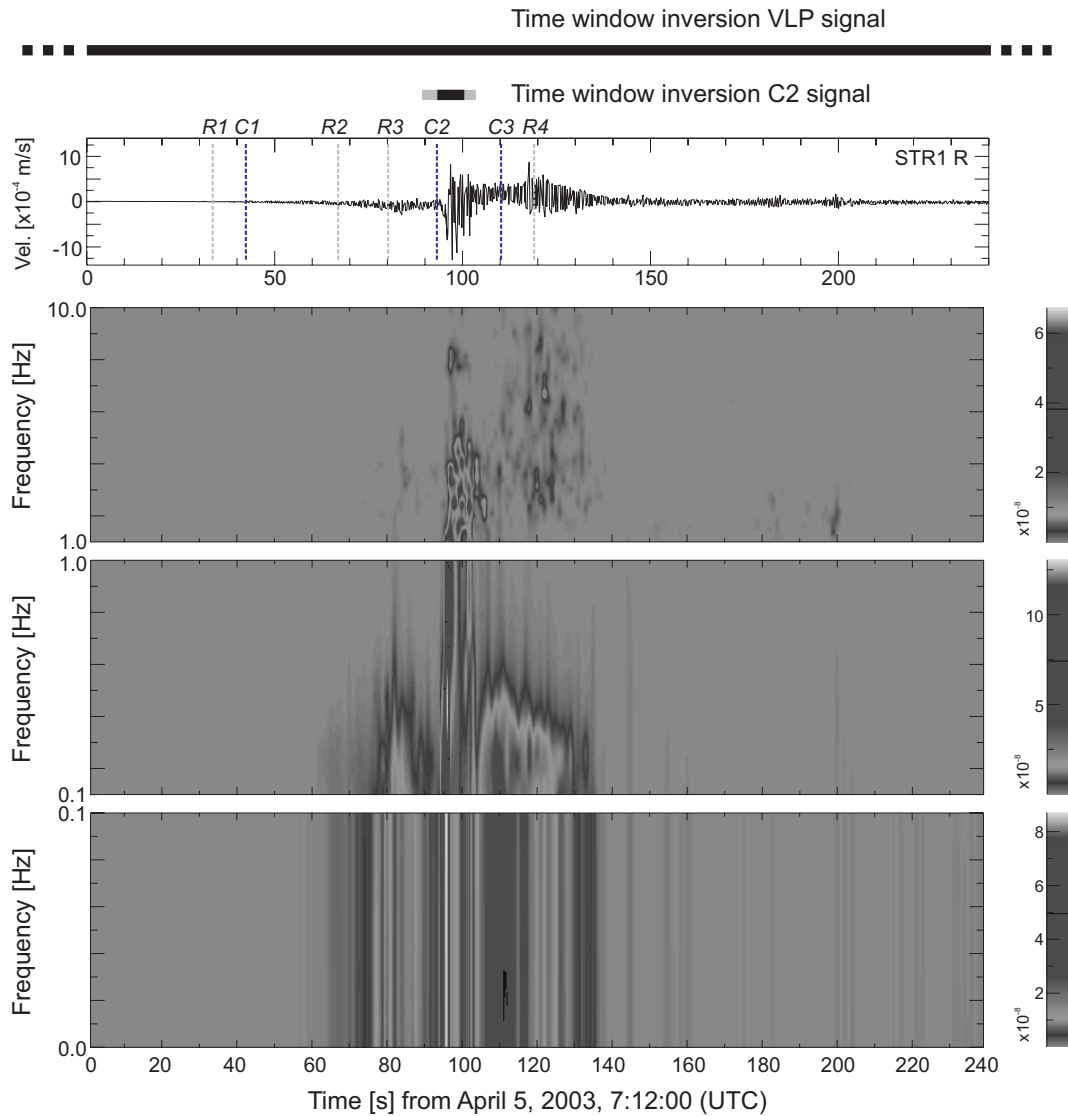
Figure 8.2: *Seismogram (velocity) and corresponding spectrogram of the radial component at station STR1. Eruption and seismic phases commented in the text are marked in the figure. Data windows used for the inversion are indicated by thick black lines at the top. Time window for the ULP signal exceeds the plotted time interval (dotted line). A thick grey line indicates the whole time window plotted in Fig. 8.5.*
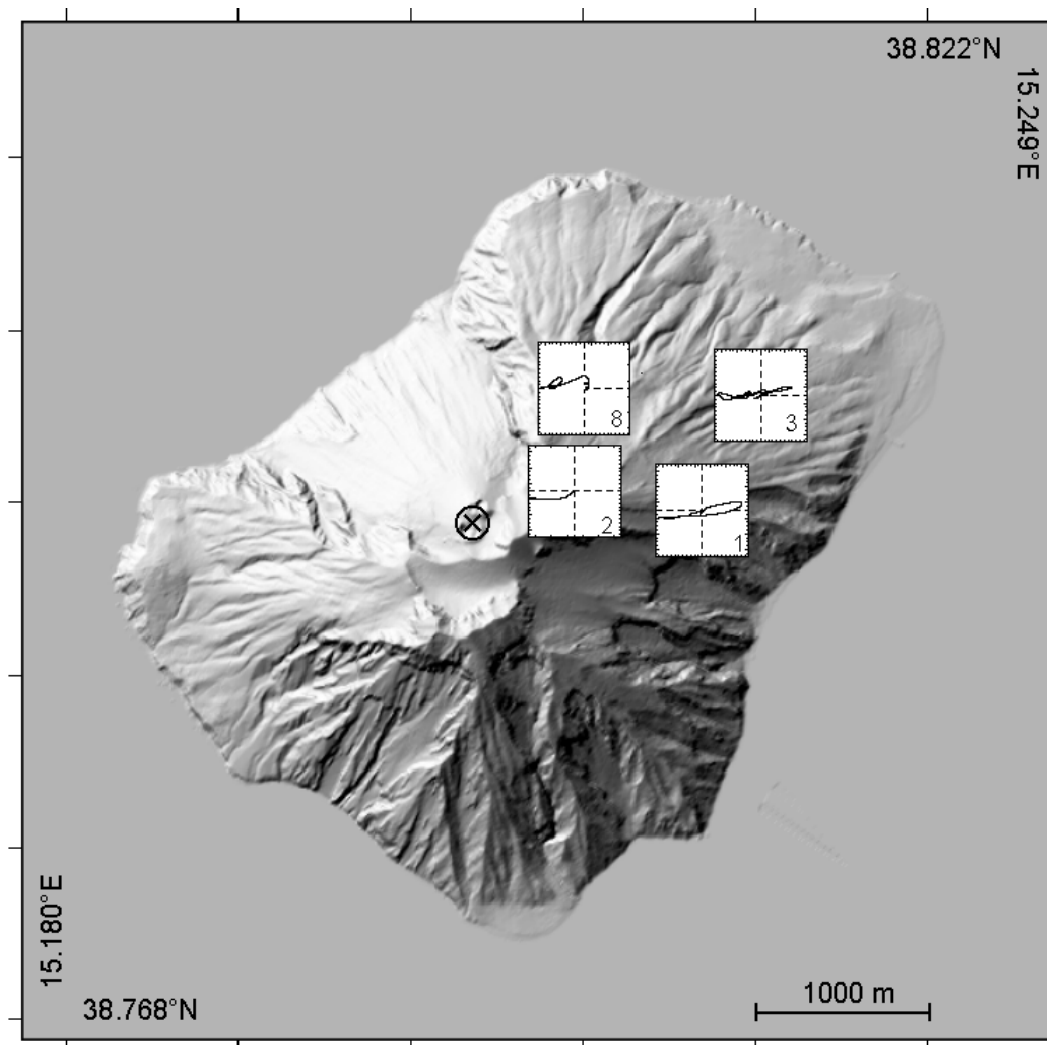
Figure 8.3: *Map of Stromboli volcano and particle motions observed at four stations (STR1, STR2, STR3, STR8) for the long period signal, obtained by lowpass filtering of the data below 0.1 Hz. Dashed line corresponds to the profile used for plotting Fig. 8.6. The location of the fissures mentioned in the text is also indicated, as well as the source location (cross).*

seismic energy (Fig. 8.2). Phase R3, which was corresponding to the first jet emissions, is visible in the seismic records, associated both with an amplitude peak and the radiation of a wider range of frequencies, up to 0.8 Hz. Phase R4 is also observed in the seismograms, starting at about 7:13:50 UTC (C3), being preceded by a period of reduced amplitudes of seismic signals. During this period, which has been associated to the fallout of ejected material and consequent landslides, the seismic signals present an increment of the high-frequency content (mostly above $1 - 2 ~Hz$), the low-frequency content being still present and slowly decaying. The two strong onsets clearly visible in the seismic data (C1 at 7:12:42 UTC and C2 at 7:13:33 UTC) have apparently no expression in the IR and deformation data. The seismic phase C2 seems to be consistent with the visual observation of the blast seen from the helicopter (*Calvari et al.* (2006)).

The seismic signal following C1, characterized by a high-frequency content, is not suitable for the inversion, since the small-scale velocity structure and the scattering processes have a strong effect in this range of frequencies. A trial for such inversion led to ambiguous results and it is therefore not discussed. On the contrary, the seismic phase C2 is associated with a radiation of frequencies below 1.1 Hz. Therefore, this part of the signal is worth to be studied in detail by a deeper analysis and waveform modelling. The ULP event is the second signal suited for a deeper modelling analysis because of its low-frequency content and its simple linear polarization. However, the analysis of the ULP signal is complicated by the possible presence of significant tilt effects and by the fact that some traces are interrupted, requiring the set up of a specific inversion technique. Finally, seismic data from the last seismic phase (C3), with dominant frequencies at $1 - 10 ~Hz$, cannot be used for source inversion: in this range of frequencies, seismic wave propagation is very sensitive to small-scale velocity heterogeneities, which we cannot reproduce in our model.

8.4 Methodology

The moment tensor (MT) allows a general representation of the seismic source, under the assumption of a point source. Moment tensor components reproduce the effects of any combination of generalized dipoles, and therefore can be used to describe either crack opening (tensile component), buried internal explosions (isotropic component) or shear faults (double-couple component). The modelling of the seismic source for certain volcanic events (e.g., long period events, eruptive sources, etc.) may require the introduction of an additional single force (SF) term. SFs are used to reproduce the radiation effects caused by the mass movement in the focal region, such as fluid transfer or material ejection during eruptions. The time evolution of point-like sources is typically approximated by simple functions, such as smoothed triangles or a Brüstle-Müller function (*Brüstle and Müller* (1983)) of

a given duration. Again, in the case of volcanic sources, this description may be insufficient, owing to the complexity of the source mechanisms and of their time evolutions. Consequently, we may describe the focal mechanism of the volcanic source as:

$$\sum_{i=1,6} M_i(t) + \sum_{j=1,3} F_j(t) = \sum_{i=1,6} M_i f_i(t) + \sum_{j=1,3} F_j f_j(t) \tag{8.1}$$

where M indicates MT components, F indicates SF components, and f represents the STFs of each component. For the given source, seismic waves are radiated and their propagation can be described by means of Green's functions (GFs). The displacement u observed at the volcano surface (at coordinate x) will be equal to the time convolution of a source (M, F) and a radiation term (G) (Aki and Richards, 1980):

$$u_n(\vec{x}, t) = M_{pq}(\vec{\xi}, t) \star G_{np,q}(\vec{\xi}, \vec{x}, t) + F_p(\vec{\xi}, t) \star G_{np}(\vec{\xi}, \vec{x}, t). \tag{8.2}$$

As a first step toward the inversion of Eq. (8.2), we calculate GFs. They have been obtained for a homogeneous medium with topography. The rheological parameters of the model (3500 m/s, 2000 m/s and 2650 g/cm^3, for P- and S-wave velocity and density respectively) are in agreement with those chosen by *Chouet et al.* (2003) to study the source mechanism of small-scale explosions at Stromboli. A homogeneous model is justified to study signals with a dominant frequency of 0.01 Hz (ULP signal) and associated wavelength larger than 100 km, since small-scale perturbations in the model will affect the average wavefield parameter only. The topography, however, cannot be neglected at long wavelength. Our model takes into account Stromboli's volcano topography (*Baldi et al.* (2005)) with a height accuracy of 3 m, but does not include bathymetry and the water layer. To calculate GFs, we have applied a pseudospectral approach (*Tessmer et al.* (1992); *Tessmer and Kosloff* (1994)), using a 3D grid with a size of 12.5 $km \times$ 12.5 km centred on Stromboli Island. The grid precision is 100 m for the horizontal components, while it is variable in the vertical direction. The small grid interval is justified because the same GFs will be used later to study the high-frequency radiation.

The source mechanism and their time dependency can then be retrieved by inverting Eq. (8.2), either in time or in frequency domain (*Ohminato et al.* (1998); *Auger et al.* (2006); *Cesca and Dahm* (2008)), to fit the observed seismograms. The stability of such inversions typically increases when the amount of available data is much larger than the number of unknowns of the problem. In this study we follow a frequency domain inversion technique (*Cesca and Dahm* (2008)), which is preferable than time-domain inversion in terms of computational requirements. This method fits the complex spectra by minimizing the $L2$ norm between data and synthetics, and finally reconstructs the timedependent source components.

The choice of an $L2$ norm to evaluate the data fit implicitly gives a larger weight to larger amplitude data, for which a larger signal-to-noise ratio is expected. The technique also allows the inclusion of different constraints on time behaviour of the source (*Ohminato et al.* (1998)), in order to have a common time dependency for different source components. The described inversion method cannot take into account effects associated with tilt, since GFs are calculated for displacements. Tilt signals are observed as a consequence of the ground inclination and result in long period signals, affecting mostly the horizontal components of the seismograms. As a consequence of tilt, the vertical and horizontal components of recorded seismograms, $d_z(t)$ and $d_h(t)$, will be:

$$d_z(t) = u_z(t)$$

$$d_x(t) = u_x(t) - g \int \int \tau(t) dt dt \tag{8.3}$$

where $u_z(t)$ and $u_x(t)$ are the vertical and horizontal displacements, $\tau(t)$ is the tilt angle and g is the gravity acceleration. The tilt angle can be expressed as the difference between the vertical displacements at neighbouring grid points, divided by the horizontal distance between them. For example, if we want to calculate the tilt along the x direction at a point $(x_0, y_0, z(x_0, y_0))$, we can calculate it from the variation of the vertical displacements at $(x_1, y_0, z(x_1, y_0))$ and $(x_{-1}, y_0, z(x_{-1}, y_0))$, Δx being the horizontal distance between neighbouring points. For small angles, this leads to:

$$d_z(x_0, t) = u_z(x_0, t)$$

$$d_x(x_0, t) = u_x(x_0, t) - g \int \int (\frac{u_z(x_1, t) - u_z(x_{-1}, t)}{2\Delta x}) dt dt. \tag{8.4}$$

If the observed signal is dominated by displacements, Eq. (8.4) will be approximated by:

$$d_z(x_0, t) = u_z(x_0, t)$$

$$d_x(x_0, t) \approx u_x(x_0, t) \tag{8.5}$$

which in the case of low frequencies will lead to similar waveforms on the radial and vertical components. On the contrary, when the horizontal component of the seismograms will be dominated by the tilt component, Eq. (8.4) will be rewritten as:

$$d_z(x_0, t) = u_z(x_0, t)$$

$$d_x(x_0, t) \approx lim_{\epsilon \to 0} \left[-g \int \int \times (\frac{u_z(x_0 + \epsilon, t) - u_z(x_0 - \epsilon, t)}{2\epsilon}) dt dt \right] \tag{8.6}$$

$$\approx K \int \int u_z(x_0, t) dt dt$$

The constant K states here the proportionality between the vertical displacement, observed on the vertical component of the seismograms, and its double time integration, observed on the horizontal component.

8.5 Inversion of the ULP signal

The location of the deformation source derived from GPS records during the paroxysmal explosion of April 5, 2003 (*Mattia et al.* (2004)), agrees with the location of a wide set of smaller explosive events (*Chouet et al.* (2003)). The direction of linearly polarized ULP ground motion points toward the same epicentre and depth at $38.7925°$N, $15.2106°$E and $200\ m$ below the surface. Thus, it is reasonable to fix the source location at this point when calculating GFs.

The inversion approach described in paragraph 4 cannot be used for this part of the signal, having only 6 complete (3 components for stations STR1 and STR3) and 6 incomplete traces (remaining stations). Since the number of stations is limited in our study we introduced physical constraints to the inversion whenever justified. For the ULP signal, that started prior to the paroxysmal explosion and which cannot be associated with fast mass movement, it is justified to test three types of moment tensor sources, (1) an opening and closing crack of arbitrary orientation and moment, (2) a thrust or normal faulting dip-slip source with arbitrary strike, dip and moment (rake is fixed to either $\pm 90°$) and (3) a pure explosive source. For (1) and (2) we tested 32.400 possible orientations using analytical formulas for moment tensor representation (*Dahm et al.* (1999); *Nakano and Kumagai* (2005)) and assuming a Poisson ratio of $\nu = 1/3$, proper for hot rocks (*Chouet et al.* (2003)). The scalar moment was inverted by linear least squares. A bandpass filter between 0.02 and $0.1\ Hz$ was applied to seismic ground displacement data and GFs. The choice of the STF was based on the low-frequency waveform of the radial component seismograms at STR1, since this time trace shows the largest amplitudes and lowest signal-to-noise ratio. As a first approach, we assume the tilt negligible and we do not include it in our modelling. The assumed STF (STF1) is defined as the normalized radial component of displacement at STR1. Then, we introduce tilt effects, which are accounted in GFs and in synthetic seismograms on the base of Eq. (8.4). To choose properly the STF, we first assume that the reference seismogram (STR1, radial) is dominated by displacements, and thus Eq. (8.5) is valid: in this case, we can use again STF1. If, on the contrary, the seismogram is dominated by tilt effects, then Eq. (8.6) is valid, and we choose STF2, which is defined as the double derivative of the observed waveform. Note that all these STFs (Fig. 8.4a, left) describe the moment rate. The whole signal was considered for station STR1 and STR3 (time window of $300\ s$), and a shorter

signal (110 s) for the remaining stations, since these records were interrupted when stations were damaged. The L^2 fit of solutions and the used STFs are shown in Fig. 8.4a. Since all considered sources have the same degree of freedom, the misfits of different inversions results can be directly compared.

The best fitting solutions (Fig. 8.4a) are obtained for a shear crack source and STF1, either including tilt (misfit = 0.258) or neglecting it (misfit = 0.260). The difference between these misfits is not significant; the good fit for the model without tilt is related to the better fit of the trace with the largest amplitude (STR1, radial). On the contrary, the solution derived by the model including tilt presents a better fit of all traces (Fig. 8.4b) and is therefore preferable. In both cases, the fault and auxiliary planes have a NW – SE striking (42° and 77° respectively). The shear crack solution for a different source time function (STF2) is consistent in terms of the fault plane orientations, but presents a significantly lower fit (misfit = 0.350). Similarly, the assumption of a tensile crack source, indicating a dipping crack (53.78°) with a wide range of striking angles, leads to worse fits. Finally, the inversion for a pure isotropic explosive source led to a worse fit and could not reproduce the main observations. It is therefore not further discussed.

The best fitting double-couple solution (misfit = 0.258) is found for the two possible nodal planes of a dip-slip thrust mechanism with strike $\varphi_1 = 77°$, dip $\delta_1 = 66°$, slip $\lambda_1 = 90°$; $\varphi_2 = 257°$, $\delta_2 = 24°$, $\lambda_2 = 90°$. The scalar seismic moment calculated for this solution ($M_0 = 5.0 \times 10^{13} Nm$) is associated with a moment magnitude $M_w = 3.0$. Neglecting the tilt modelling, the best solution (misfit = 0.260) would be associated to the fault planes identified by $\varphi = 42°$, dip $\delta_1 = 55°$, slip $\lambda_1 = 90°$; $\varphi_2 = 222°$, $\delta_2 = 35°$, $\lambda_2 = 90°$, with a scalar moment of $3.0 \times 10^{15} Nm$. A comparison between the observed and synthetic seismograms for the best solution is presented in Fig. 8.4b, showing a relatively good waveform fit. Although synthetics cannot perfectly match all characteristics of the observed signals, the fit is much improved with respect to those obtained for the others fault plane orientations. The fit cannot be further improved under the initial assumptions (e.g., pointlike source, choice of the STF, etc.). Nevertheless, these assumptions were required for this application, in consequence to the amount of data and their quality (e.g., interrupted traces).

The double-couple solution was unexpected for us, but presents a significantly better fit than the solution of the tensile crack. The obtained focal mechanism explains the observed motion toward the crater at stations STR1, STR2 and STR3, as well as the uplift and horizontal motion observed at the GPS station SDIC before the eruption onset (*Mattia et al.* (2004)). One of the nodal planes (strike 222 - 257°, dip 24 - 35°) of the double-couple solution is in agreement with the dike orientation retrieved by the inversion of GPS data (*Mattia et al.* (2004)), the other is in agreement with the most likely orientation of the effusive fissure 2 that opened a channel between the feeder dike and the SDF (strike 42 - 77°,
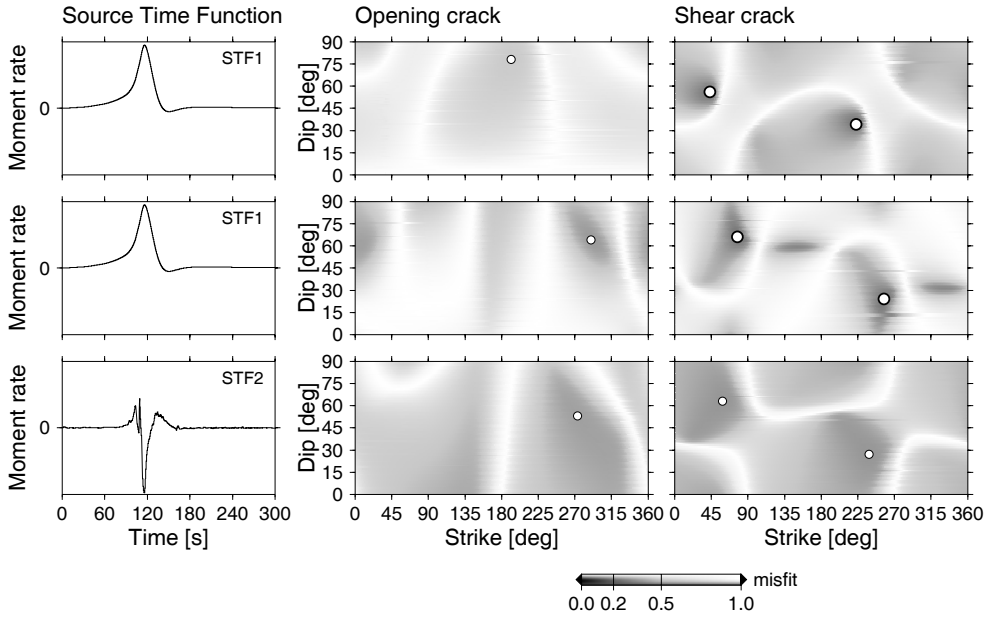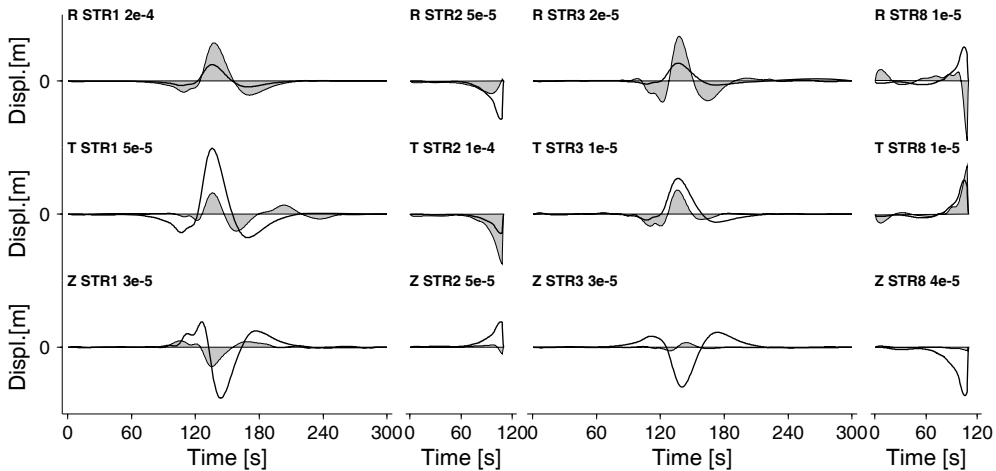
Figure 8.4: *Results of the inversion for the ULP event. (a) Normalized source time functions and plots of the corresponding misfit estimations (grey scale) for different orientations of tensile and shear cracks. Best solutions in each case are indicated by circles; the largest circle corresponds to the absolute best solution. Three sets of models are tested: modelling only displacement (top), modelling tilt and displacement using STF1 (centre) and STF2 (bottom). (b) Comparison of the observed (thick black lines) and synthetic (thin lines, grey areas) displacements related to the best solution of case (a); amplitudes are normalized by factors indicated for each station. Time windows begin at 7:11:37 UTC.*

dip 55 - 66°). The discrimination between the two fault planes is not possible from seismogram analysis, but the integrated interpretation indicates that plane 1 was the rupture plane (see discussion below). The rupture area of plane 1 can be roughly estimated in the range of $1.5 \times 10^5 \ m^2$, based on the results of *Mattia et al.* (2004), the source location and Stromboli topography. The usage of an average crustal value for the shear modulus, $4.41 \times 10^{10} \ Pa$ (*Udias* (1999)), or a value based on rheological parameters used for the forward modelling (*Chouet et al.* (2003)), $1.4 \times 10^{10} \ Pa$, leads to a slip estimation (e.g., Eq. 15.23 in *Udias* (1999)) of $0.01 - 0.02 \ m$ and $0.45 - 1.41 \ m$, respectively for the model with and without tilt; the last estimations are comparable with the dislocation retrieved by the inversion of GPS data.

The STFs plotted in Fig. 8.4a (left) show that slip, and thus the release of energy, was extremely slow, with dominants period of about 50 to 100 s. This is untypical for tectonic earthquakes, but has been observed for slow slip events in subduction zones (*Hirose et al.* (1999); *Ozawa et al.* (2001); *Dragert et al.* (2001)). The slow slip events are thought to be influenced or controlled by the movement of fluids in the fault plane (*Obara* (2002); *Melbourne and Webb* (2003)). The slow slip pulse and the possible role of fluids will be discussed below. The slow slip can also explain the fact that the signal was not recorded at more distant stations, e.g., on the Italian coast.

8.6 Inversion of the high-frequency C2 signal

The same inversion code and the same GFs could be used to study the high-frequency C2 signal. This signal may be related to the climactic blast observed by *Calvari et al.* (2006), and therefore a different source mechanism is expected. Although seismic signals do not present linearized particle motions, we assume the source location to be unchanged. The choice of this location, with a shallow depth beneath the craters, seems reasonable for the eruptive source.

In addition, the source location is in good agreement with those retrieved for eruptive sources at Stromboli (*Chouet et al.* (2003)).

To avoid the superposition of the waveform related to the ULP signal, time traces are band-passed in the range between 0.1 and 2 Hz, in agreement with the dominant frequency of 0.8 Hz of the phase we want to model. In this frequency range, effects from scattering due to topography and medium heterogeneities become significant. This is probably responsible for the waveform complexity of the signal observed after the onset of the phase. For this reason, it is difficult to separate the STF and wave propagation effects a priori. Therefore, the STF has not been constrained before the inversion. Additionally, we cannot exclude the existence of SF components during the explosion (fast mass movement), so that all nine possible components were inverted. Owing to the larger number of
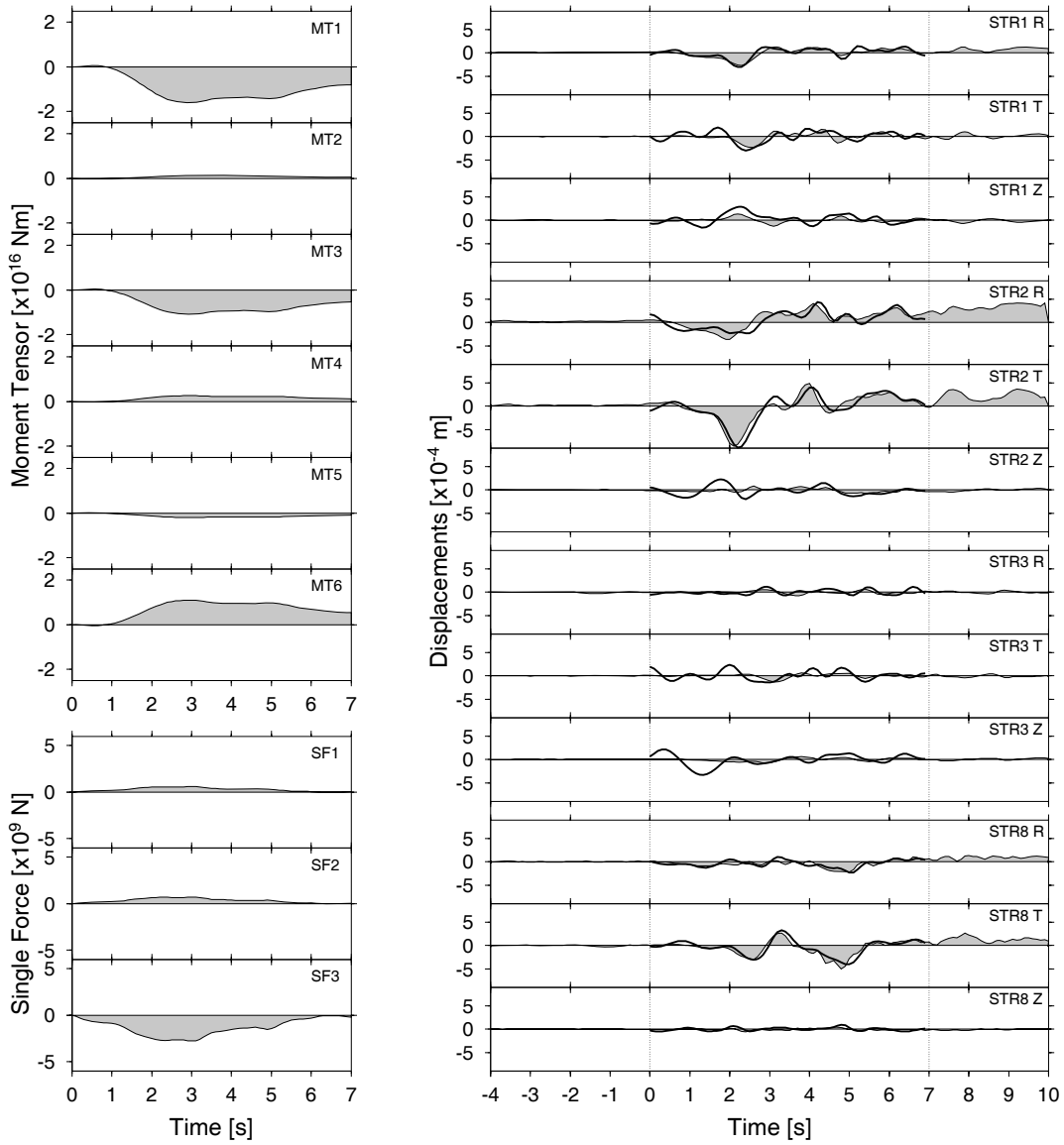
Figure 8.5: *Results of the inversion for the blast signal (C2). Left: inverted time-dependent source components (grey areas). Right: comparison of observed (continuous lines) and synthetics (dashed lines) displacements for the retrieved solution. Time windows assume a reference time at 7:13:34 UTC; inversion windows correspond to the interval between 0 and 7 s (7:13:34 - 7:13:41 UTC).*

unknowns and the fact that wave scattering becomes important and cannot be adequately modelled with a homogeneous volcano model, the inversion results have to be interpreted with more caution. During the inversion, we apply the constraint to have a common time dependency for each MT component and a second common time behaviour for SF components (*Ohminato et al.* (1998)). The retrieved time-dependent source components are shown in Fig. 8.5, together with the comparison between synthetic and observed seismograms. Seismogram fit is very good, especially for those traces (e.g., STR1 radial, STR2 transversal) which have larger amplitudes. Despite the expected difficulties, results indicate a quite simple STF with a major pulse-like moment release with a 2 to 3 s duration at the beginning of the explosion. During this time, almost all the total moment is released. The source mechanism is represented by a MT and a nearly vertical SF component, pointing downward. The MT corresponds to a simple vertical compensated linear vector dipole (CLVD), associated with a minor isotropic component (25%). Such mechanism would be able to reproduce the physical phenomenon following the sudden opening of a nearly vertical conduit, including the ejection of material along the vertical direction and simultaneous relaxation of the conduit walls. The estimated equivalent scalar moment (*Silver and Jordan* (1982)) for this signal is 0.61×10^{15} Nm, corresponding to an equivalent moment magnitude $M_w = 3.7$. The vertical force (2.8×10^9 N) is interpreted as the response of the medium to the upward ejection of material from the upper conduit.

8.7 Interpretation of the eruptive process

The unrest of Stromboli volcano started with the flank eruption of December 28, 2002, and ended with the large paroxysmal explosion on April 5, 2003. Our results from the analysis of broadband seismic data are used together with the information provided by previous studies to define a realistic model for the entire eruption process. The main phases are summarized in Fig. 8.6 and discussed below.

(a) After the flank eruption of December 28, 2002, lava flows were observed at SDF slope. The most active effusive fissure was located at about 500 m altitude. At this time the upper conduit to the crater region and the three vents were blocked (*Calvari et al.* (2005)). The existence and filling of a feeder dike are obvious from the observation, but its orientation has not been constrained.

(b) On February 15, 2003, the lava flow from the 500 m fissure was interrupted. The effusive activity, however, concentrated at a fracture located at 760 m (fissure 2). The upper conduit to the crater region was still blocked *Calvari et al.* (2005). The migration of the effusive activity to higher levels is
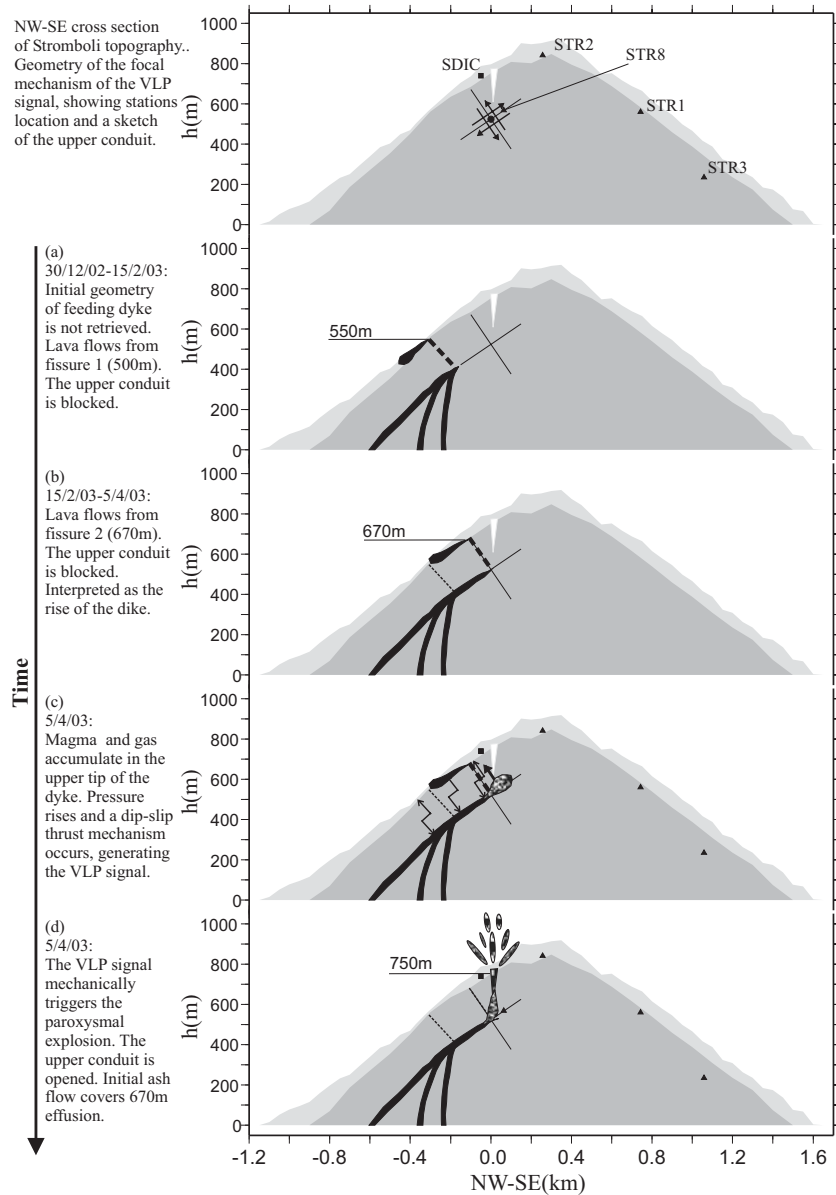
Figure 8.6: *Top: representation of the derived fault planes and focal mechanism (ULP signal) with respect to the NW - SE cross-section of Stromboli topography (dark grey) and island profile from SW (light grey). Broadband seismic stations (triangles) and SDIC GPS station (square) are also shown. Bottom: schematic representation of four modelled phases of the volcanic crisis and the eruptive process: (a) December 30, 2002 - February 15, 2003; (b) February 15, 2003 - April 5, 2004; (c) April 5, 2003, precursor dip-slip thrust mechanism associated to the ULP seismic signal; (d) April 5, 2003, paroxysmal eruption associated to the large amplitude seismic signal.*

interpreted in terms of the rising magma in the feeder dike and the formation of new fissure cracks within the SDF. The orientation of fissures 1 and 2 is most likely perpendicular to the free surface of the SDF to fulfil the free shear stress boundary condition at the free surface.

(c) On April 1, 2003, the upper conduit to the crater was still blocked, no information is available for the following days (*Calvari et al.* (2006)). On April 5, 2003, the pressure in the feeder dike possibly starts to increase, due to the accumulation of lighter material such as gas in the upper part of the blocked feeder. Evidence for the presence of gas is given by the blast which followed. The increasing pressure in the upper tip of the feeder dike most likely changed the stress field in the region of the future seismic source. We assume that shear stress accumulated along the existing crack planes of fissures 1 and 2. It is then likely that the accumulated stress was released by a shear dislocation along one of the pre-existing fissures, e.g., fissure 2 in 670 m a.s.l. ($\varphi = 42 - 77°$, $\delta = 55 - 66°$, $\lambda = 90°$). The slow slip caused the observed ULP seismic signal and the measured deformations and uplift. The direction of slip (thrust type) is in very good agreement with the expected stress field caused by the pressurized feeder dike tip. The orientation of this nodal plane is approximately perpendicular to the free surface at SDF and its projection on the SDF surface is consistent with the location of fissure 2. The interaction between the magma body and the shear crack, and the viscosity of the magma may have slowed down the rupture and slip velocity of the shear dislocation, similarly to what is predicted for fluid-filled tensional cracks (e.g. *D'Auria et al.* (2006)).

(d) We suggest that the slow dip-slip thrust precursor is responsible for triggering the paroxysmal eruption. The first seismic onset (C1) is observed shortly after the beginning of the ULP signal. After the onset C1, a continuous sustained seismic signal is observed until the blast occurs (C2). This observation indicates a relation between the ULP signal and the increase of seismic activity. The estimated moment (and slip) of the slow thrust event must have caused a significant stress change in the nearby region of the blocked feeder dike. Since the shear event released shear stress, but not released efficiently magma pressure, the reopening of the upper conduit could bring to a large blast through the crater vents (*Calvari et al.* (2006)); another possibility is that the shear event has also released pressure, triggering degassing and thus the large explosion. In any case, the timing of seismic onsets supports our interpretation of the ULP as trigger for the paroxysm: the blast signal (e.g., Fig. 8.1, top) is occurring almost at the same time as the change in sign of the velocity seismogram of the ULP signal. This time corresponds to the recording of the maximal absolute displacement and thus with the maximal rupture velocity. When the explosion occurs, shear stress and pressure re-

duce more quickly, and consequently also the rupture velocity decreases. The reopening process of the upper conduit can allow during a few seconds the emission of ash only (*Calvari et al.* (2006); *Rosi et al.* (2006)), which is then followed by a large blast through the crater vents (*Calvari et al.* (2006)).

The source mechanism retrieved from high-amplitude seismic phase C2 is dominated by a CLVD component with a vertical dipole plus a downward vertical force, a reasonable source mechanism for the observed blast, which occurred from a nearly vertical conduit situated above the upper tip of the feeder dike.

8.8 Conclusions

An exhaustive study of the April 5, 2003, explosion at Stromboli volcano, Italy, has been carried out by analyzing available seismic data, comparing them with other available geophysical data, and modelling the main features of the volcanic source behaviour and eruption dynamics. A synoptic analysis of the published geophysical data indicated a clear correlation, with similar phases of the eruptive process being identified, between GPS measurements, infrared data and visual observations of the climactic explosion and seismic data. The beginning of different phases shows a permanent time offset, indicating that GPS signals first recorded a change in the volcano's behaviour; the associated variation in temperature always shows a short delay (about 2 s). At last, eruptive phases are observed in terms of climactic emissions. The analysis of the seismic signals allowed the identification of some of these eruption phases. In some cases they are marked by clear seismic onsets (R3). More often, they are simply associated to an increase of the seismic signals amplitudes (R4) or a variation in the frequency content (R2). The beginning of phase R1 could not be associated with any change in the seismic data, while we observe an additional seismic onset, C1, which cannot be related to other geophysical observations. These two observations could be related, under the assumption of a slow process of ash venting (R1), which only starts generating significant seismic signal after a delay of about 10 s (C1).

Two main features of the seismic data have been identified. The first is an ultra long period signal with major frequency content below 0.1 Hz, characterized by a linear polarization in the direction of the crater area, with the first motion toward the crater. The second is a higher frequency signal (dominant frequencies in the range 0.7 – 1.1 Hz), associated to the observed climactic blast. A seismic source has been derived for the two signals, using a frequency domain inversion technique and including tilt modelling for the ULP signal; different constraints on the seismic source were assumed, depending on data characteristics. Results indicate a dip-slip thrust as source for the ULP signal, while the source retrieved for the blast signal is related to a vertical CLVD and a vertical force. Moment

magnitudes derived from these inversions are equal to $M_w = 3.0$ and $M_w = 3.7$, respectively. Eruption dynamic is modelled here in the framework of the whole volcanic crisis, which started in December 2002, providing evidence for the progressive rise of a dike beneath SDF. Dike propagation is in agreement with the observed migration of effusive vents along SDF. The derived model for the April 5, 2003, paroxysmal explosion suggests that the eruptive process could have been mechanically triggered by a slow slip movement along a pre-existing fracture; this mechanism would be responsible for the precursor ULP signal. The retrieved geometry of the fault system, and the consequent radiation pattern, can explain the polarities of observed low-frequency seismic signals, as well as the initial uplift at SDIC station (GPS data). As a consequence of the slip along this fracture, the upper conduit could have been reactivated, resulting in the initial ash emission and the following blast. From the analysis of seismic data, we have derived important information about the source characteristics of the April 5, 2003, explosion at Stromboli volcano. Unless the complexity of the eruption dynamics and the problems arising by the damaging of the seismic stations, it has been shown how the proposed approach still supports important additional information to better understand the behaviour of Stromboli volcano when larger explosions occur. The method proposed to model tilt effects also constitutes a new step toward a more detailed modelling of seismic waveforms at volcanic areas. While in this study its application was limited by the data amount and quality, this methodology may be of interest for future applications.

Chapter 9

Laboratory experiments

9.1   Introduction

In order to study the eruption dynamics of volcanoes and the properties of magma under controlled laboratory conditions, the University of Würzburg hosts since 1991 the Physical Volcanological Laboratory (PVL). A German group, consisting of volcanologists, physicists and engineers realized since the eighties experiments on hot melt in ad hoc-laboratory. In the so-called **T**hermal **E**xplosion **E**xperiments (TEE), remelted rocks (ultrabasic to andesitic composition) with an entrapped gas/water volume were used to study the dynamics of different eruption styles as (i) the blow-out mechanism and (ii) the interaction of hot melt and water (**M**olten **F**uel **C**oolant **I**nteraction – MFCI) (*Zimanowski et al.* (1986), *Zimanowski et al.* (1991), *Zimanowski et al.* (1995); *Büttner et al.* (1997); *Zimanowski et al.* (1997); *Büttner and Zimanowski* (1998); *Zimanowski* (1998)).

9.2   Setup and description of the laboratory experiments

In order to study the seismic signals radiated during volcanic explosions of the Strombolian type, we performed the first time seismic measurements during controlled and reproducible blow-out experiments with a gas volume entrapped in basaltic melt.

For this purpose the following experimental setup was used (figures 9.1, 9.2): The inductively heated steel crucible (1) was installed onto a substructure, consisting of a cooler block with two ceramic plates (black) and a radiation screen. A force transducer was mounted between the cooler block and the base plate. The injection tube (2), the single piston pump (3), the linear drive (4), the submersion unit (6) were mounted onto the injection unit, designed for positioning and submersion of the injection tube and release of both, fluids and gases.
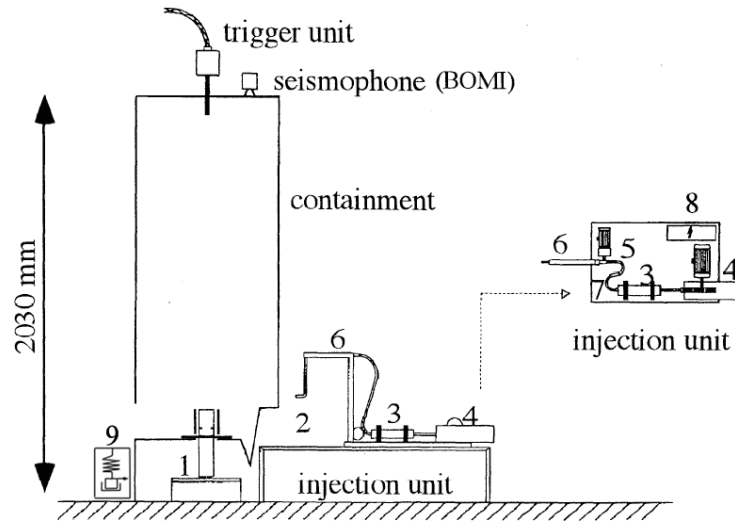
Figure 9.1: *Cross section of the experimental setup. (1) the inductively heated steel crucible, (2) the injection tube, (3) the single piston pump, (4) the linear drive, (5) the submersion drive, (6) the submersion unit with the solenoid valve (7), and the electronic box (8). (9) indicates the position of the seismometer (modified from Zimanowski et al. (1997)).*

The vertical seismic sensor (9) was installed on the laboratory floor, 20 cm beside the substructure. The passive seismometer of russian production (Type SM3) had an eigenfrequency of $f_{SM3} = 1.0\ Hz$ and a seismometer constant of $G_{SM3} = 200\ Vs/m$.

A volume of $\approx 150\ cm^3$ of granulated volcanic rock-material (Hohen – Stoffeln olivine – melilitite Hegau/F.R.G.) was filled in a cylindrical steel-crucible (diameter 5 cm) and inductively heated to 1653 K. The melt was fragmented by a pressurized gas volume released through an injection tube at pressures up to 100 bar at the inner bottom of the crucible. The chemical composition and the physical properties of the melt are summarized in table 9.1.
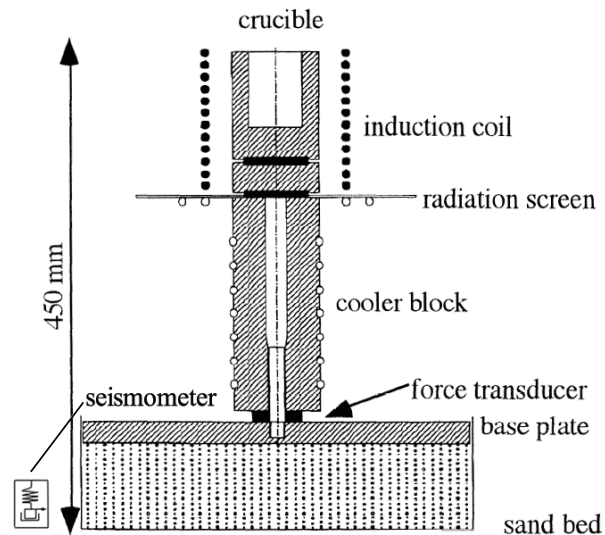
Figure 9.2: *Cross section of the substructure. Note the position of the seismometer (modified from Zimanowski et al. (1997)).*

Chemical analysis (XRF)		Physical properties	
Oxide	Wt. %		
SiO_2	38.12	temperature	$1653K$
TiO_2	2.91	viscosity	$1.3Pa \cdot s$
Al_2O_3	10.42	T_g	$1233K$
Fe_2O_3	5.90	T_m	$1620K$
FeO	8.32	c_p	$2.8J/(gK)$
MnO	0.25	λ	$1W/(mK)$
MgO	13.40	ρ	$2880kg/m^3$
CaO	14.92		
Na_2O	2.68	phenocrysts	$\approx 10vol.\%$
K_2O	1.21	vesicularity	$\approx 3vol.\%$
P_2O_5	1.76		

Table 9.1: *Composition and physical properties of the test melt. Data represents melt at experimental conditions (from Zimanowski, 1998). T_g: glass transition temperature; T_m: mush transition temperature.*

Although the rock chips are carefully selected, some inclusions and veins of altered rock can not be avoided. Thus, to achieve a homogeneous melt, at least one hour of constant heating at 1650 K is necessary for dehydration and degassing of excess H_2O. Following this procedure a subliquidus melt-mass of $\approx$ 0.4 kg (correspondent to a melt volume of 140 cm^3) is generated. The resulting melt phenocryst-gas system is used for the MFCI-experiments (*Zimanowski* (1998)). Altogether 19 laboratory experiments have been run. Considering the long preparation and heating time for the single experiment, between three and five blow-outs per day could be realized.

The seismic signals generated during this type of laboratory magmatic explosions were recorded at an sampling interval of 520 ms ($\approx$ 1923 Hz) and 175 ms ($\approx$ 5714 Hz), respectively, resulting in a typical record length of $t_{rec} <$1 s, and a signal duration of $t_{sig} \approx$ 0.5 s.

Additionally the dynamics of the laboratory explosions were documented by simultaneous high speed cinematography, force- and pressure recordings, a seismophone (a soil microphone, used originally by the police force of the Ex-German Democratic Republic for surveillance of possible "illegal" abscondence of GDR-refugees) and measurements of the electrostatic field. The pressurized gas experiment was repeated several times, varying the gas pressure between 15 and 100 bar.

9.3 Physics of the blow-out experiments

In order to rapidly release the gas volume beneath the melt, the injection tube is first horizontally moved on top of the crucible and then slowly lowered into the melt ((3) in figure 9.3, (2) in figure 9.1). After the opening of the solenoid valve ((7) in figure 9.1) the pressurized argon is injected laterally on the base of fluid.

If a gas volume is released in a fluid, in the ideal case the two plane-parallel layers (gas-fluid) are in equilibrium; e.g. the lateral injection of air into water, blows up vertically the entire water plug.

Also in the case of an immiscible fluid, as e.g. magma, the lateral inflow of the gas at the base of the melt crucible forms an air cushion, but here the slightest perturbation leads to release of potential energy, as the heavier magma moves down under the gravitational field, and the lighter material is displaced upwards. The surface tension forces are exceed and, as the instability develops, downward-moving irregularities are quickly formed, so that it becomes distorted into waves (*Wohletz* (1986); *Morrissey et al.* (2000)). This physical phenomenon is known as Rayleigh – Taylor instability.

It leads to a rapid fragmentation, that is dependent on the crucible dimensions. *Büttner et al.* (1997) and *Zimanowski et al.* (1997) state that the amplitude of the electrical signal generated during the volcanic explosion, is proportional to the surface enlargement by the fragmentation.

Figure 9.3: *Scheme of the entrapment configuration: (1) melt, (2) gas, (3) gas injection tube (modified from Zimanowski (1998))*

The longer the crucible length, the longer is the dwell time of the magma plug inside the crucible and hence the time for the development of the Rayleigh – Taylor instability. Therefore the magma plug ejected from a short crucible becomes less fragmentated and the recorded electrical signal is smaller.

Applied to a real volcano this result could be translated in the hypothesis: assuming a constant gas pressure, a deeper magma level (longer conduit) causes a stronger fragmentation.

Figure 9.4: *Cartoon of Rayleigh-Taylor fragmentation in a tube geometry. (a) A liquid (grey) is accelerated by gas vertically upward. (b) A certain wave length is stimulated and amplified. (c) Once the amplitudes reach a critical value, fragments of the liquid detach from the interface (Zimanowski (1998)).*

9.4 Seismic measurements during the blow-out laboratory experiments

9.4.1 Frequency response of the experimental setup

In order to account for the transfer function of the experimental setup, a delta-pulse like excitation was realized, hitting the melt crucible simply with a hammer. The centre and lower trace in figure 9.5 shows the impulse response (vertical component) of the melt crucible before and after heating, the upper trace shows the seismogram of a blow-out run at 75 *bar*.
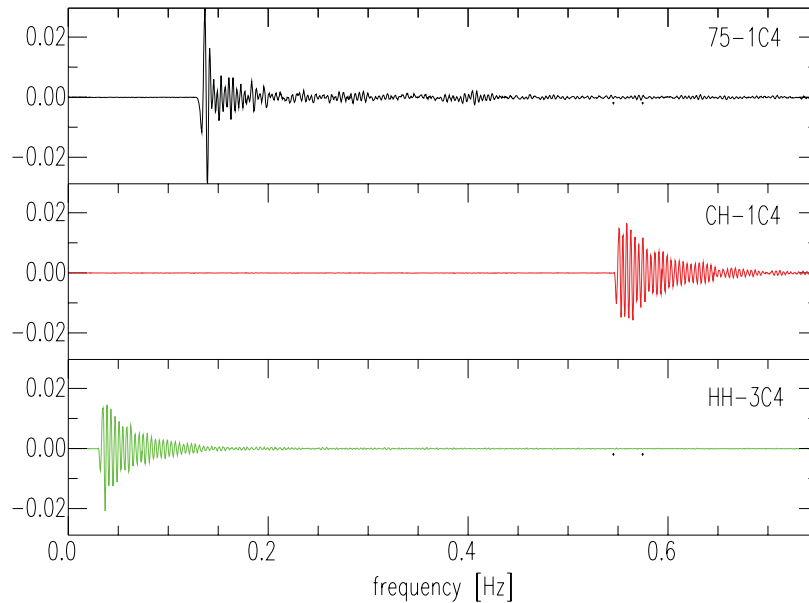
Figure 9.5: *Comparison of seismic signal recorded during a blow-out run (up) and the excitation of the experimental setup with a hammer: cold crucible response (centre), hot crucible response (down).*

Figure 9.6 illustrates the respective amplitude spectra of the traces from figure 9.5. The main resonance peak of the whole system is observed at $f_{sys} = 252\ Hz$. The seismic energy radiated during a blow-out run lies in a frequency band between $70 - 220\ Hz$, and thus below the eigen-frequency of the experimental setup. This can be well observed in figure 9.7, where the grey shaded area depicts the spectral energy contribution of a blow-out run at 75 *bar*.
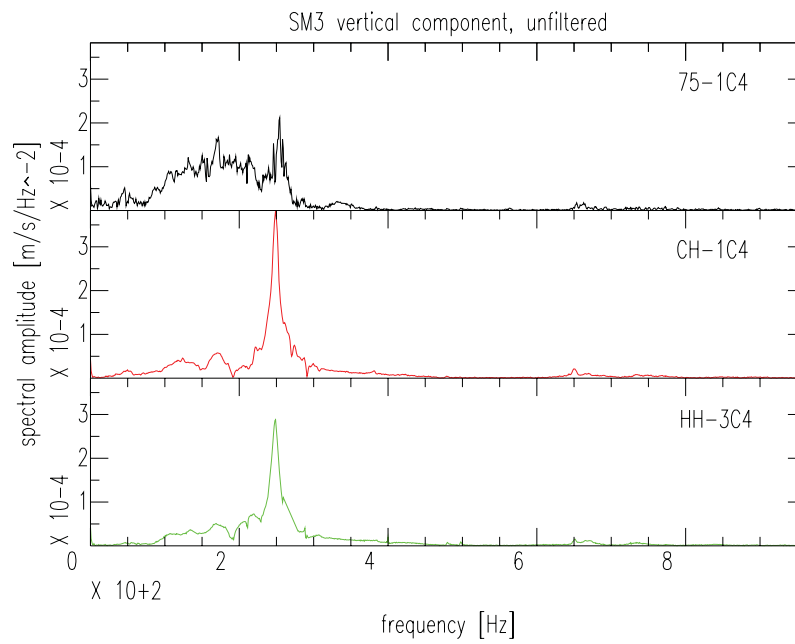
Figure 9.6: *Frequency spectra of signals from figure 9.5: blow-out (up), cold crucible response (centre), hot crucible response (down).*
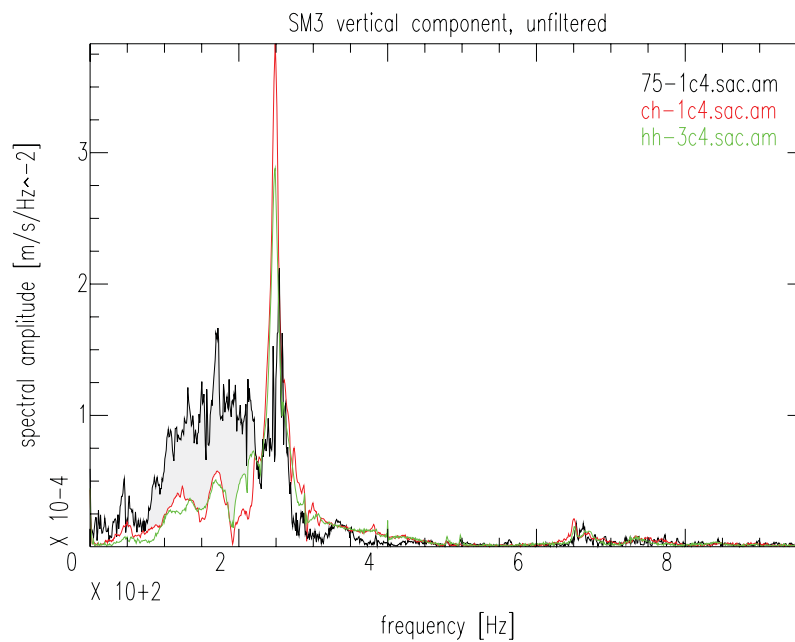
Figure 9.7: *Same as figure 9.6, illustrated as overlay plot. The grey shaded area indicates the spectral energy contribution of the blow-out run.*

9.4.2   Seismic waveforms as function of the heating time

As already introduced, the preparation and heating time before a single blow-out experiment is relatively long and can last up to two hours. Therefore, in the course of one day generally not more than five experimental runs could be realized, using always the same melt crucible.

In order to study how this fact reflects in the seismic data, three blow-out runs, each with the same driving pressure have been compared. Figures 9.8 and 9.9 show the seismic vertical traces and the corresponding amplitude spectra recorded during three 100 *bar* blow-outs, performed in the same crucible after a heating time of 2 *h* (black), 4 *h* (red), 6 *h* (green), respectively.
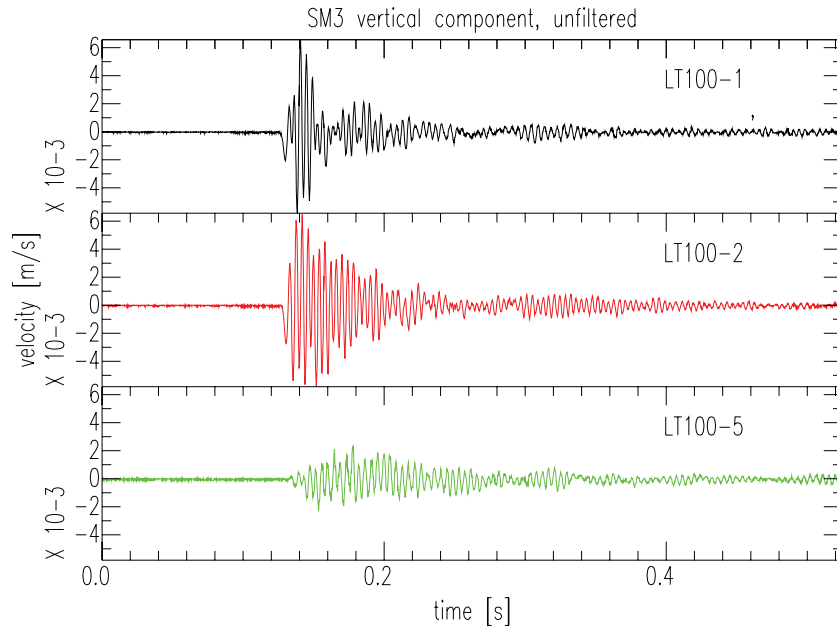
Figure 9.8: *Seismic vertical traces recorded during three 100 bar blow-outs, performed in the same crucible after a heating time of 2 h (black), 4 h (red), 6 h (green), respectively.*

It can be noted, that with progressive heating time, the seismic signals change significantly. The seismic record of the first blow-out run after a 2 *h* heating time shows a relatively broadband signal with the main spectral energy radiated in a frequency band between 150 − 230 *Hz*. However, the red and the green seismogram, respectively recorded after 4 *h* and 6 *h* heating, show that the coupling conditions had changed in time. As confirmed by the (red) amplitude spectrum (figure 9.9) the high amplitudes are due to resonance effects of the experimental setup, even if the eigen-frequency shifted slightly below the $f_{sys} = 252$ *Hz*, determined *a-priori* during the calibration runs (see chapter 9.4.1). The last blow-out exper-

iment (green traces) confirmed the same trend: after 6 h of heating the seismic amplitudes became still more monochromatic and even smaller and the resonance frequency continued to shift to lower frequencies (225 Hz).
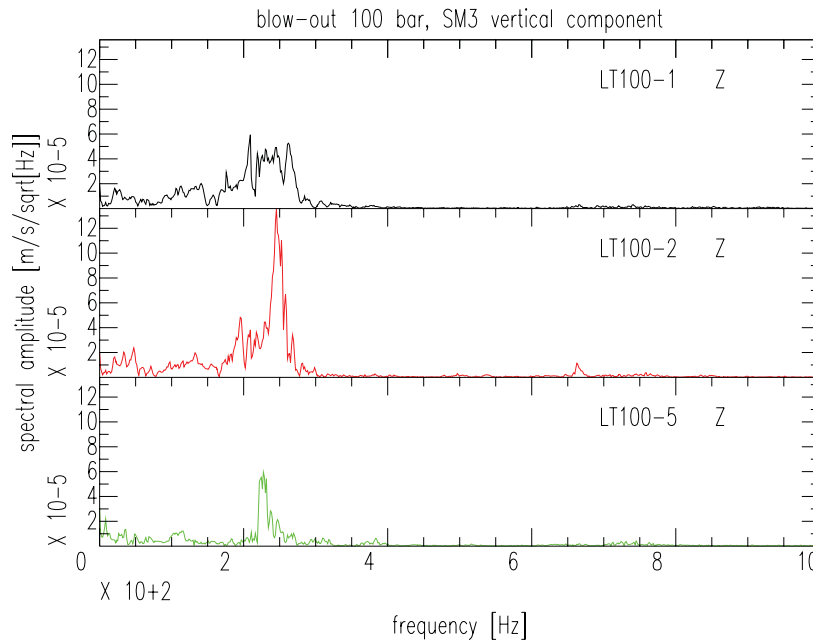
Figure 9.9: *Amplitude spectra of seismic signals from figure 9.8.*

Therefore in the course of the day the continuous heating process $(8 - 10\ h)$ leads to a progressive corrosion of the melt crucible and a diminution of the wall dimension. The seismic coupling becomes weaker, and hence the seismic signal assumes a more monochromatic character and smaller amplitudes.

This an important observation, as also inside a real volcano the contact zone between magma and the feeding system does not represent a distinct solid-fluid boundary as in the laboratory case (steel – magma), but rather a transition zone between the *solidus* and the *liquidus* point.

Concluding, it can be stated, that seismic signals with a broadband frequency content indicate a rupture in a more brittle regime, whereas a monochromatic signal, called usually *low-frequency event*, suggests a blow-out in a more ductile environment.

9.4.3 Variation of the crucible dimensions

A further experimental series addressed the question about the influence of the crucible dimension on the seismic waveforms. For this purpose two crucibles (diameter of 5 *cm*) with a length of 8 *cm* and 12 *cm* were available.

Three blow-out runs for each crucible have been realized. Figure 9.10 and 9.11 show the corresponding seismograms (vertical component) of three 100 *bar* blow-outs, realized each in the 8 *cm*, as well as in the 12 *cm* crucible.
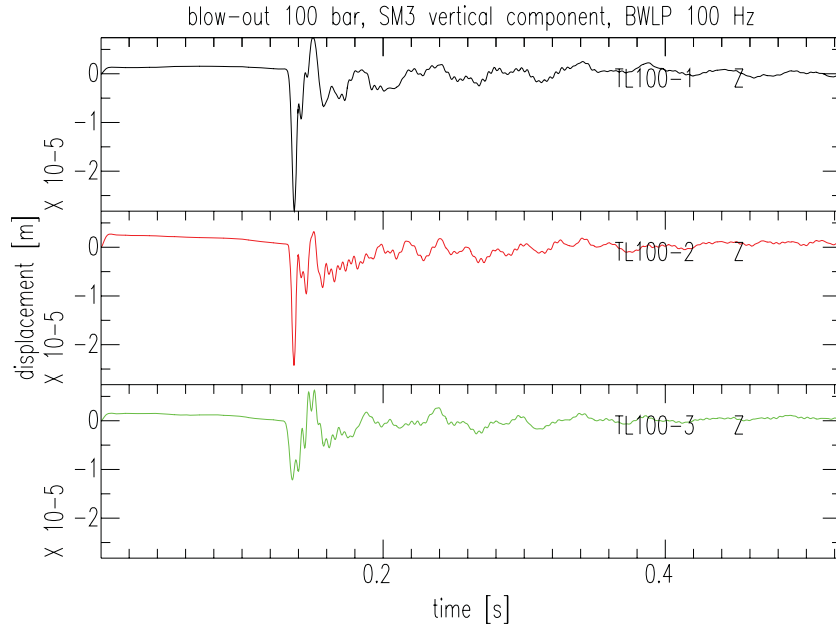
Figure 9.10: *Seismic records of three 100 bar blow-outs, realized in a melt crucible of 8 cm length.*

The dependence of the signal on the heating period influenced our measurements also in this experimental set up, as previously found (figures 9.10 and 9.11). In fact, the later the experiment was run in the course of the day, and the longer the crucible was exposed to the inductive heating, the lower and more monochromatic were the affected frequencies.

Concerning the amplitudes of the 100 *Hz* low-pass filtered signals, it can be observed that the blow-outs realized in the 8 *cm* crucible show a peak-to-peak amplitude two times larger than for the 12 *cm* crucible. Therefore, blow-outs in longer crucibles generate weaker seismic signals. The deeper fragmentation level corresponds to a longer fragmentation duration and the blow-out energy is converted rather in fragmentation than in seismic energy. Nevertheless, a high fragmentation level results in a stronger recoil and consequently generates stronger seismic signals.
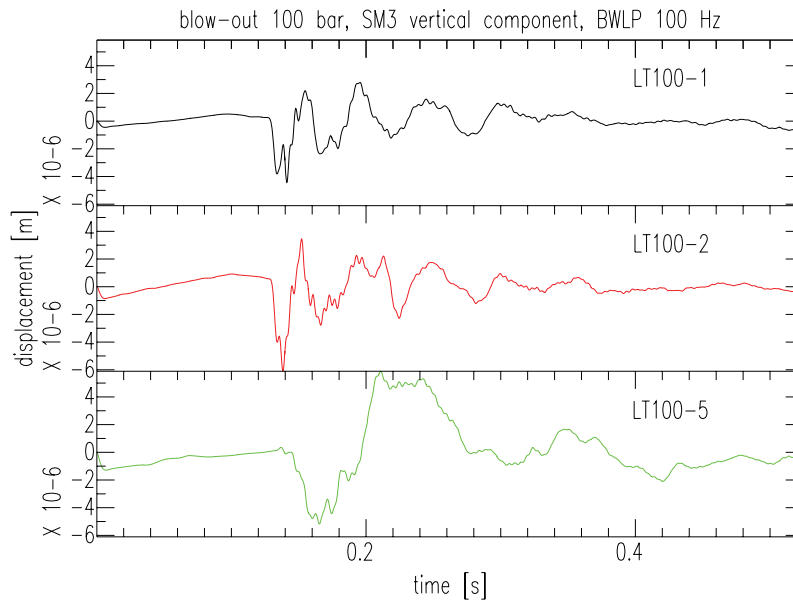
Figure 9.11: *Seismic records of three 100 bar blow-outs, realized in a melt crucible of 12 cm length.*

9.4.4   Variation of the blow-out pressure

A series of experiments were performed to evaluate the seismic signals recorded during blow-out runs under different air-pressure condition. Figure 9.12 shows the velocity-proportional signals for the pressure values of 15 *bar*, 30 *bar*, 50 *bar*, 75 *bar*, 100 *bar* (from top to bottom). The following graphs illustrate the integration (displacement [*m/s*]) of the five original seismograms (figure 9.13) and the respective low-pass filtering at 50 *Hz* (figure 9.14).

Even if the volume, the temperature and the chemical composition of the melt are exactly known and controlled, the experiences described in chapter 9.4.2 show, that the influence of the heating time on the crucible impedes a perfect reproducibility of the experiments. Contrary to the expectations, it can be generally stated that a higher blow-out pressure generates a longer signal duration, rather than a higher amplitude. This is obvious for the 50 *bar* (centre trace) and the 100 *bar* run (lower trace). Here the unfiltered velocity (figure 9.12) and the displacement seismogram (figure 9.13) show a strong monochromatic component and a longer signal duration with respect to the seismograms recorded during the lower blow-out pressures. The 50 *Hz* low-pass filtered seismogram (figure 9.14) shows that – except for the 15 *bar* run – the peak-to-peak amplitudes are similar. This indicates a sort of saturation and shows that a gas pressure of 30 *bar* is sufficient to push out the complete magma volume from the crucible with maximal exit velocity.
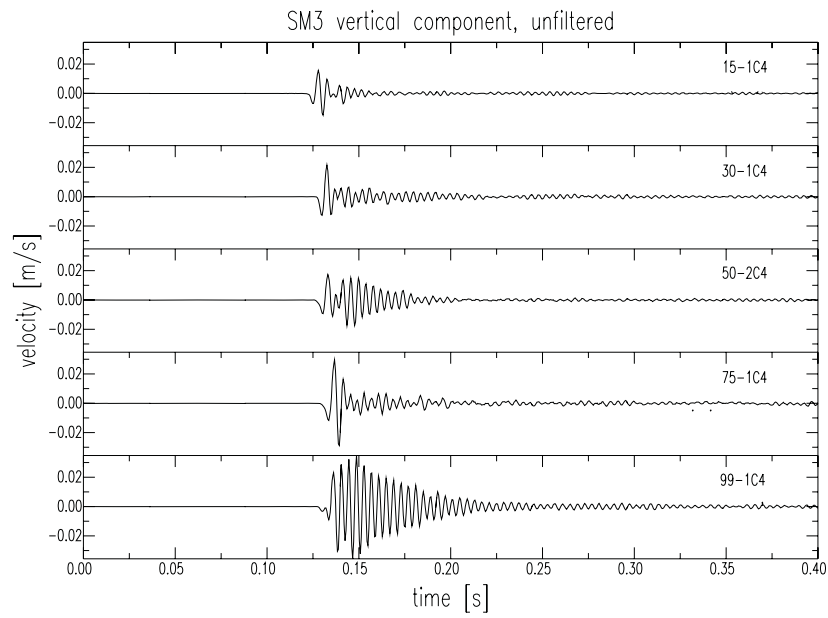
Figure 9.12: *Velocity proportional registration (vertical component) performed during five blow-out runs with different air pressures: 15 bar, 30 bar, 50 bar, 75 bar, 100 bar (from upper to lower trace).*
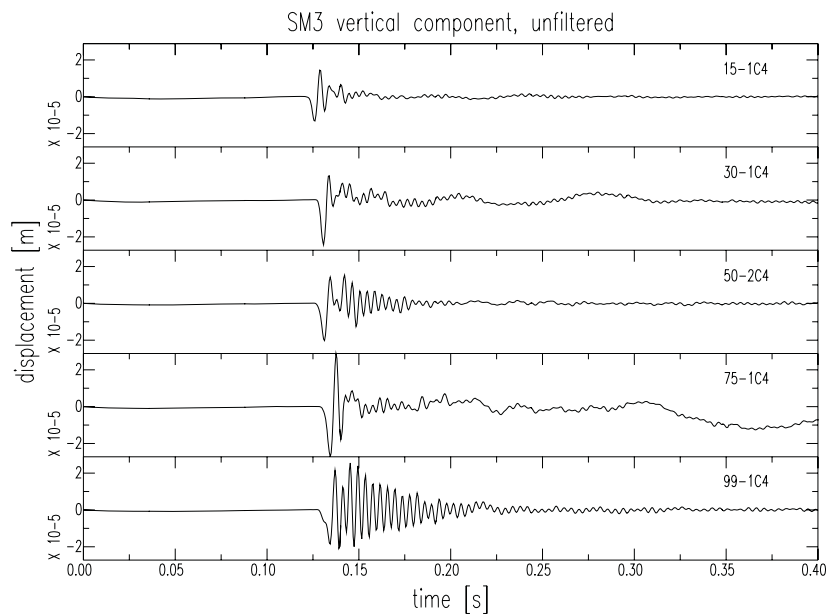
Figure 9.13: *Integration of seismic signals from figure 9.12.*

An increase in the gas pressure results in a stronger fragmentation, but not in a higher ejection velocity of the plug, and not in a stronger seismic signal. This is true, both for the 8 *cm*-crucible as well as for the 12 *cm*-crucible. Possibly, melt crucibles with significantly larger dimensions and a higher capacity could lead to higher seismic amplitudes. Hence, the decisive parameter determining the seismic waveform is not gas pressure, but the heating time of the crucible and the corresponding seismic coupling conditions between magma and conduit wall.
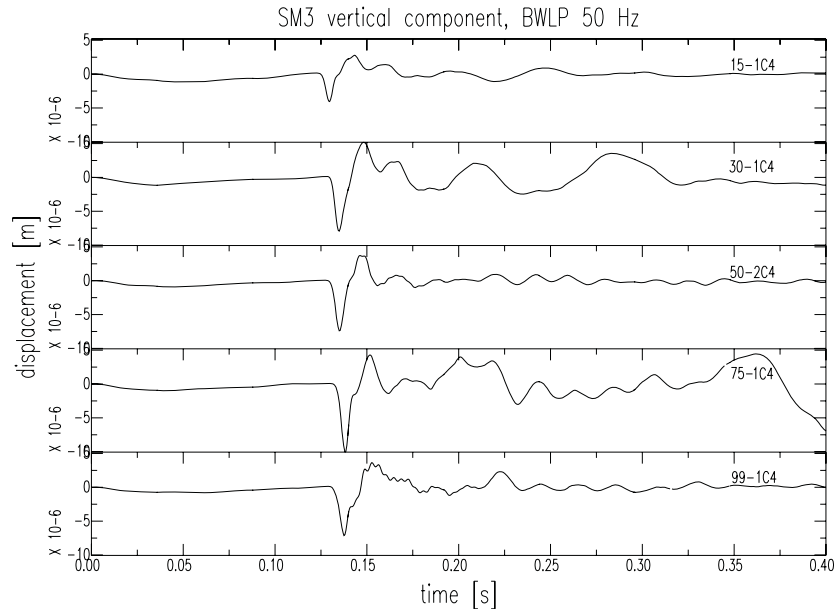
Figure 9.14: *Same as figure 9.13, low-pass filtered at 50 Hz.*

Increase of the driving gas pressures does not generate necessarily larger seismic amplitudes. In particular, beyond a threshold high blow-out pressures do not increase the energy radiation of seismic source, due to coupling problems of the blow-out source.

In order to compare the seismic signals with those recorded by the force transducer mounted between the cooler block and the base plate (figure 9.2), the amplitudes of the signals recorded by the force transducer $[N]$ have been plotted against the absolute signal amplitude of the velocity seismograms $[m/s]$. For this purpose not only the blow-out runs have been used (blue triangles in figure 9.15), but also the *hammer*-calibrations applied to the cold (red triangles) and the pre-heated melt crucible (green diamonds). Figure 9.15 illustrates well the proportionality to a square root law of all values. Up to 1500 N the relation between force and velocity seems nearly linear, but for higher forces the graph shows only a slight increase in the seismic velocities (saturation).
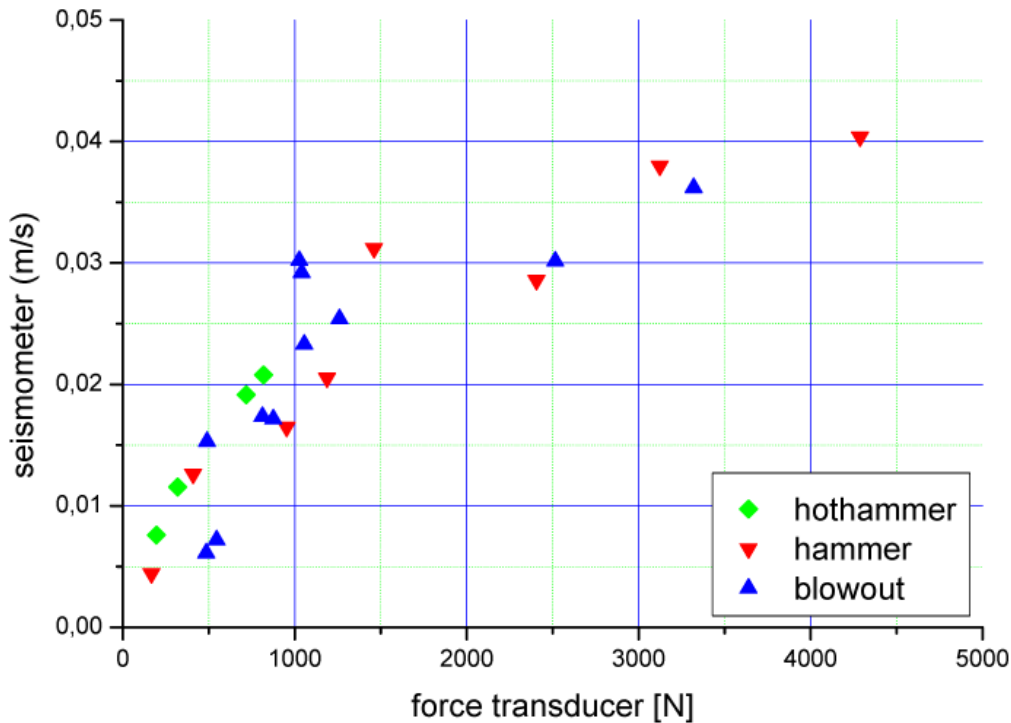
Figure 9.15: *Relationship between the amplitudes recorded by the force transducer (abscissa) and the seismic velocity (ordinate) recorded during the blow-outs (blue triangles) and the calibration (red triangles and green diamonds).*

9.5 Conclusions

Finally some comments on the relevance for the *real case* of the seismic laboratory measurements will be considered. Therefore, seismograms measured during the blow-out experiments are compared with seismic traces recorded at Stromboli during typical strombolian activity.

Büttner et al. (2000) performed laboratory experiments on the fragmentation and expansion of magmatic melt using remelted volcanic rock at magmatic temperatures as simulant. A specially designed DC-amplifier in combination with high speed data recording was used to detect short-time electrostatic field effects related to the fragmentation and expansion history of the experimental system.

Generally three physical mechanisms have been experimented: (i) the thermohydraulic explosion (MFCI – water in magma), (ii) the blow-out (gas in magma) and (iii) injection of a gas volume in a crucible filled with volcanic ash. Parallel electrical measurements revealed that all mechanisms generate completely different magnitudes of electrostatic field gradients, depending on the degree of fragmentation: (i) 10^4 V/s for the MFCI, (ii) 10^2 V/s for the blow-out and (iii) 10^0 V/s for

the already *a-priori* fragmentated volcanic ash expansion.

Similar measurements realized at Stromboli volcano with a 0.8 *m* rod antenna revealed comparable results for the two observed eruption mechanisms (gas expansion in magma and in ash). These measurements demonstrated that the blow-out run may be the most realistic laboratory experiment for simulating the typical strombolian activity (*Zimanowski*, pers. communication).

Only a qualitative comparison between the laboratory seismic measurements recorded during the blow-out experiments and those performed at Stromboli volcano can be given. The upper two traces of figure 9.16 show the seismogram of two 100 *bar* blow-outs recorded at a sampling rate of 5714 *Hz* (LT100-*). The lower trace illustrates the broadband seismogram of an *explosion-quake* recorded at a distance of ≈ 200 *m* by a *Le-3D/20s-seismometer* at a sampling rate of 125 *Hz* (STR1 Z).

All three traces are integrated (displacement), the amplitudes are normalized and the sampling rate of the blow-out experiments is 45 times higher, than for the Stromboli-registration. Even if the seismic traces cannot be directly compared, striking resemblance between the waveforms can be observed. The laboratory and the Strombolian seismograms show very similar wavelets: a first negative (double) impulse (green shaded), followed by weaker second positive movement (yellow shaded).

This confirms that the laboratory experiments represent a realistic simulation of a typical Strombolian explosion-quake, also from a seismic point of view.

Recapitulating, the following experiment results have been established:

- Seismic signals with a broader frequency content are an indicator for a rupture in a more brittle environment.

- More monochromatic signals suggest a blow-out in a more ductile regime.

- Blow-out in longer crucibles generate seismic signals with smaller amplitudes.

- A deeper fragmentation level corresponds to a longer fragmentation duration and the blow-out energy couples rather in the fragmentation, than in the seismic energy.

- A high fragmentation level results in a longer recoil and generates stronger seismic signals.

- An increase in pressure results in a stronger fragmentation, but not in a higher velocity of the ejected plug, hence not in a higher seismic amplitude.
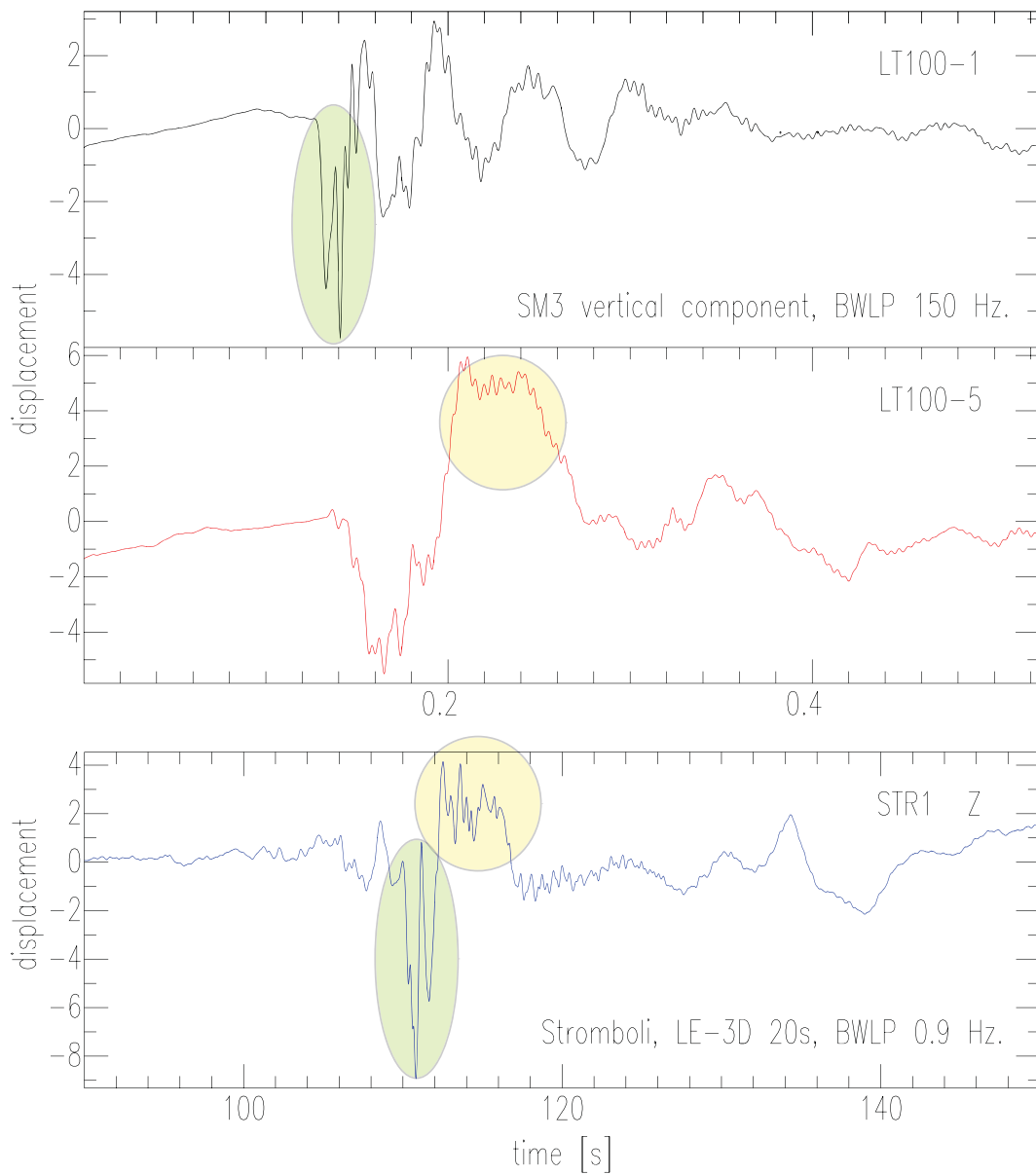
Figure 9.16: *Qualitative comparison of the vertical seismic traces of two 100 bar blow-out experiments (black and red) with a typical near-field seismogram of an explosion-quake recorded at Stromboli (blue). Note the different time scales and the waveform similarities.*

Translating the *learned lesson* to the real case *Stromboli* the following hypotheses can be formulated:

- As monochromatic signals indicate a blow-out in a more ductile regime, the corresponding low-frequency volcano events are generated in the deeper part of the conduit, where the continuous contact of magma with the conduit walls prevents a good seismic coupling.

- Seismic signals with a broader frequency content (including the air-wave) are probably generated closer the conduit mouth. In the terminal part of the conduit the magma is not continuously in contact with the conduit walls. This resembles the laboratory case where the crucible is exposed to a shorter heating time and the rupture occurs in a more brittle regime.

- Concerning the air-wave the following can be stated: the deeper the blow-out occurs inside the conduit, the weaker is the air-wave phase in the explosion-quake seismogram. As already reported by *Mori et al.* (1989), the amplitude of the air-wave onset may indicate the level of the explosion-quake inside the conduit. Assuming a constant blow-out pressure, the shallower (closer to the conduit mouth) the explosion-quake occurs, the stronger is the air-wave in the explosion-quake seismogram.

In conclusion, the laboratory blow-out experiments simulate very well the volcano-seismic signals recorded at Stromboli, in a frequency range between $0.05 - 20$ Hz. However it is obvious that very long period observations, like the tilt signal observed during the expansion phase of the terminal part of the volcanic edifice prior to the paroxysm of April 5, 2003 (see chapter 8, cannot be simulated in the laboratory. In contrast to the real volcano the pressure accumulation in the experimental laboratory setup occurs outside the melt crucible.

Bibliography

Aki, K., M. Fehler, and S. Das (1977), Source mechanism of volcanic tremor: Fluid driven crack models and their application to the 1963 Kilauea eruption., *J. Volcanol. Geotherm. Res.*, *2*, 259–287.

Auger, E., L. D'Auria, M. Martini, B. Chouet, and P. Dawson (2006), Realtime monitoring and massive inversion of source parameters of very long period seismic signals: an application to Stromboli volcano, Italy., *Geophys. Res Lett.*, *33*, doi:10.1029/2005GL024703.

Baldi, P., M. Fabris, M. Marsella, and R. Monticelli (2005), Monitoring the morphological evolution of the Sciara del Fuoco during the 2002-2003 Stromboli eruption using multi-temporal photogrammetry, *ISPRS J. Photogramm. Remote Sens.*, *59*(4), 199–211.

Benoit, J., and S. R. McNutt (1997), New constraints on source processes of volcanic tremor at Arenal Volcano, Costa Rica, using broadband seismic data, *Geophys. Res. Lett.*, *24*(4), 449–452.

Berckhemer, H., and B. Akasche (1966), Seismic ground noise and wind at the seismological observatory GRF, *Special Scientific Report 1, Univ. Frankfurt*, 1–26.

Braun, T., and M. Ripepe (1993), Interaction of seismic and air waves recorded at Stromboli volcano., *Geophys. Res. Lett.*, *20*, 65–68.

Braun, T., and M. Ripepe (1995), Untersuchung zur Ursache kurzperiodischer seismischer Signale am Vulkan Stromboli (Italien)., *DGG-Mitteilungen*, *1*(95), 23–41.

Braun, T., J. Neuberg, and M. Ripepe (1996), On the origin of the long-period volcanic tremor recorded at Stromboli volcano (Italy)., *Ann. Geofis.*, *39*(2), 311–326.

Brüstle, W., and G. Müller (1983), Moment and duration of shallow earthquakes from love-wave modelling for regional distances, *Phys. Earth Planet. Inter.*, *32*, 312–324.

Brüstle, W., R. Schick, and E. Wielandt (1993), Low-frequency seismic observations on Stromboli volcano., *Acta Vulcanol.*, *3*.

Büttner, R., and B. Zimanowski (1998), Physics of thermohydraulic explosions, *Phys. Rev.*, *57*(5), 5726–5729.

Büttner, R., H. Röder, and B. Zimanowski (1997), Electrical effects generated by experimental volcanic explosions, *Appl. Phys. Lett.*, *70*(14), 1903–1905.

Büttner, R., B. Zimanowski, and H. Röder (2000), Short-time electrical effects during volcanic eruption: experiments and field measurements, *J. Geophys. Res.*, *105*, 2819–2825.

Caloi, P. (1951), Sull'origine dei microsismi in particolare riguardo all'alto adriatico., *Ann. Geofis.*, *4*(4), 525–577.

Caloi, P., and P. Migani (1971), Microsismi da piccoli bacini chiusi, da mari interni, da oceani, *Ann. Geofis.*, *24*, 515–549.

Calvari, S., L. Spampinato, L. Lodato, A. J. L. Harris, M. R. Patrick, J. Dehn, M. R. Burton, and D. Andronico (2005), Chronology and complex volcanic processes during the 2002-2003 flank eruption at Stromboli volcano (Italy) reconstructed from direct observations and surveys with a handheld thermal camera., *J. Geophys. Res.*, *110*(B02201), 23 pp., doi:10.1029/2004JB003129.

Calvari, S., L. Spampinato, and L. Lodato (2006), The 5 April 2003 vulcanian paroxysmal explosion at Stromboli volcano (Italy) from field observations and thermal data., *J. Geophys. Res.*, *149*, 160–175.

Cardaci, C., and G. Lombardo (1988), Segnali sismici a Stromboli e loro caratteristiche., *Boll. GNV*, *4*, 164–173.

Cesca, S., and T. Dahm (2008), A frequency domain inversion code to retrieve time-dependent parameters of very long period volcanic sources, *Comput. Geosc.*, *34*, 235–246.

Cesca, S., T. Braun, E. Tessmer, and T. Dahm (2007), Modelling of the April 5, 2003 Stromboli (Italy), paroxysmal eruption from the inversion of broadband seismic data, *EPSL*, *261*, 164–178, doi:10.1016/j.epsl.2007.06.030.

Chouet, B. (1985), Excitation of a buried magmatic pipe: a seismic source model for volcanic tremor., *J. Geophys. Res.*, *90*, 1881–1893.

Chouet, B. (1988), Resonance of a fluid-driven crack: radiation properties and implications for a source of long-period events and harmonic tremor., *J. Geophys. Res.*, *93*, 4375–4400.

Chouet, B. (1992), A seismic model for the source of long-period events and harmonic tremor, *In: Gasparini, P. and Scarpa, R. and Aki, K. (eds): Volcanic seismology: International Association of Volcanology and Chemistry of the Earth's Interior (IAVCEI) Proceedings in Volcanology*, pp. 133–156, berlin, Springer-Verlag.

Chouet, B., N. Hamisevicz, and T. R. McGetchin (1974), Photoballistics of volcanic jet activity at Stromboli, Italy., *J. Geophys. Res.*, *79*, 4961–4976.

Chouet, B. A., P. Dawson, G. De Luca, M. Martini, G. Milana, G. Saccorotti, and R. Scarpa (1998a), Array analyses of seismic sources at Stromboli, *Acta Vulcanologica*, *8*(2), 367–382.

Chouet, B. A., P. Dawson, G. De Luca, M. Martini, G. Milana, G. Saccorotti, and R. Scarpa (1998b), Array analyses of seismic wavefields radiated by eruptive activity at Stromboli volcano, CNR - Gruppo Nazionale per la Vulcanologia, Felici Editori, Pisa, 158 pp.

Chouet, B. A., P. Dawson, T. Ohminato, M. Martini, G. Saccorotti, F. Giudicepietro, G. De Luca, G. Milana, and R. Scarpa (2003), Source mechanisms of explosions at Stromboli volcano, Italy, determined from moment-tensor inversion of very-long-period data., *J. Geophys. Res.*, *108*(B2019), 25 pp., doi: 10.1029/2002JB001919.

Crosson, R. S., and D. A. Bame (1985), A spherical source model for low-frequency volcanic earthquakes., *J. Geophys. Res.*, *90*, 10,237–10,247.

Dahm, T., G. Manthei, and J. Eisenblätter (1999), Automated moment tensor inversion to estimate source mechanisms of hydraulically induced micro-seismicity in salt rock., *Tectonophysics*, *306*, 1–17.

Dahm, T., M. Thorwart, E. Flüh, T. Braun, R. Herber, P. Favali, B. Beranzoli, G. D'Anna, F. Frugoni, and G. Smriglio (2002), Ocean bottom seismometers deployed in Tyrrhenian Sea, *EOS, Transactions, A.G.U.*, *83*(29), 309–315.

Darbyshire, J. (1950), Identification of microseismic activity with sea waves., *Proc. R. Soc. London Ser. A.*, *202*, 439–448.

D'Auria, L., F. Giudicepietro, M. Martini, and R. Peluso (2006), Seismological insight into the kinematics of the 5 April 2003 vulcanian explosions at Stromboli volcano (southern Italy), *Geophys. Res. Lett.*, *33*(L08308), 4 pp., doi:10.1029/2006GL026018.

Del Pezzo, E., I. Guerra, A. Lo Bascio, G. Luongo, G. Nappi, and R. Scarpa (1974), Microtremors and volcanic explosions at Stromboli (Aeolian Islands) - part 2., *Bull. Volcanol.*, *38*, 1023–1036.

Del Pezzo, E., C. Godano, A. Gorini, and M. Martini (1992), Wave polarisation and the localisation of the source of the explosion-quakes at Stromboli volcano., *In: Gasparini, P. and Scarpa, R. and Aki, K. (eds.): Volcanic Seismology*, springer Verlag.

Dragert, H., K. Wang, and T. S. James (2001), A silent slip event on the deeper Cascadia subduction interface., *Science*, *292*, 1525–1528.

Dreier, R., R. Widmer, R. Schick, and W. Zürn (1994), Stacking of broad-band seismograms of shocks at Stromboli, *Acta Vulcanol.*, *4*.

Fadeli, A. (1984), A study on the eruption mechanism of Stromboli (Italy)., *Inst. Geophys. Univ. Stuttgart*, *213*, 71 pp.

Falsaperla, S., and G. Neri (1986), Seismic monitoring of volcanoes: Stromboli (Southern Italy)., *Period. Min.*, *55*, 153–163.

Falsaperla, S., and A. Pellegrino (1988), Analisi dei transienti sismici dello Stromboli (isole eolie) del settembre 1987., *I.I.V. Catania (CNR)*, *28*(88), open file report.

Falsaperla, S., A. Montalto, and S. Spampinato (1989), Analysis of seismic data concerning explosive sequences on Stromboli volcano in 1989., *Boll. GNV*, *1*, 249–258.

Falsaperla, S., H. Langer, B. Martinelli, and R. Schick (1995), Seismic measurements on Stromboli volcano in a wide frequency range., *Acta Vulcanol.*, *5*, 173–178.

Ferrazzini, V., K. Aki, and B. Chouet (1991), Characteristics of seismic waves composing Hawaiian volcanic tremor and gas-piston events observed by a near source array., *J. Geophys. Res.*, *96*, 6199–6209.

Ferrick, M. G., A. Qamar, and W. F. St. Lawrence (1982), Source mechanism of volcanic tremor., *J. Geophys. Res.*, *87*, 8675–8683.

Gordeev, E. (1990), Generation of microseisms in the coastal area., *Phys. Earth Planet. Int.*, *63*, 201–208.

Gordeev, E. I., Y. Melnikov, S. V. I., and V. N. Chebrov (1989), Volcanic tremor of Kliuchevskoi volcano (1984 eruption), *In: Latter, J. H. (ed.): IAVCEI Proc. in Volcan. 1, Volcanic Hazards*, pp. 486–503, springer Verlag, Berlin Heidelberg.

Hagerty, M., S. Y. Schwartz, M. Protti, M. Garces, and T. Dixon (1997), Observation at Costa Rican volcano offers clues to causes of eruptions, *EOS Trans.*, *78*(49), 565–570.

Harjes, H.-P., and M. Henger (1973), Array Seismologie, *Zeitschr. f. Geophys.*, *39*, 865–905.

Hasselmann, K. (1963), A statistical analysis of the generation of microseisms., *Rev. Geophys.*, *1*(2), 177–210.

Haubrich, R. A., W. H. Munk, and F. E. Snowgrass (1963), Comparative spectra of microseisms and swell., *Bull. Seism. Soc. Am.*, *53*(1), 27–37.

Henkes, D. (1991), Arrayuntersuchung des meeresmikroseismischen Wellenfeldes unter besonderer Berücksichtigung seines stochastischen Charakters., Master thesis, Univ. Frankfurt, 96 pp.

Hirose, H., K. Hirakara, F. Kimata, N. Fujii, and S. Miyazaki (1999), A slow thrust slip event following the two 1996 Hyuganada earthquakes beneath the Bungo Channel, southwest Japan, *Geophys. Res. Lett.*, *26*, 3237–3240.

Imbò, G. (1945), Il parossismo vesuviano del marzo 1944, *Rend. Acc. Sc. Fis. Mat. di Napoli*, *IV*(13), 309–325.

James, M. R., S. J. Lane, and B. A. Chouet (2006), Gas slug ascent through changes in conduit diameter: Laboratory insights into a volcano-seismic source process in low-viscosity magmas, *J. Geophys. Res.*, *111*, B05201, doi: 10.1029/2005JB003718.

Jaupart, C., and S. Vergniolle (1988), Laboratory models of hawaiian and strombolian eruptions., *Nature*, *331*, 58–60.

Jaupart, C., and S. Vergniolle (1989), The generation and collapse of a foam layer at the roof of a basaltic magma chamber, *J. Fluid Mech.*, *203*, 347–380.

Kawakatsu, H., T. Ohminato, H. Ito, T. Kuwahara, Y. Kato, K. Tsuruga, S. Honda, and K. Yomogida (1992), Broadband seismic observations at the Sakurajima volcano, Japan., *Geophys. Res. Lett.*, *21*, 1959–1962.

Kedar, S., B. Sturtevant, and H. Kanamori (1996), The origin of harmonic tremor at old faithful geyser, *Nature*, *379*, 708–711.

Kieffer, S. W. (1977), Sound speed in liquid-gas mixtures: water-air and water-steam., *J. Geophys. Res.*, *82*, 2895–2904.

Koyanagi, R., B. Chouet, and K. Aki (1987), Origin of volcanic tremor in hawaii: Part i. data from the hawaiian volcano observatory, 1969-1985., *In: Decker, R.W. and Wright, T.L. and Stauffer, P.H. (eds.): Volcanism in Hawaii*, *1350*(2-45), 1221–1257, u.S. Geological Survey Professional Paper.

Lo Bascio, A., G. Luongo, and G. Nappi (1973), Microtremors and volcanic explosions at Stromboli., *Bull. Volcanol.*, *37*, 596–606.

Longuet-Higgins, M. S. (1950), A theory of the origin of microseisms, *Phil. Trans. Roy. Soc. London (A)*, *243*(A857), 1–35.

Mao, W., and D. Gubbins (1995), Simultaneous determination of time delays and stacking weights in seismic array beamforming, *Geophysics*, *60*(22), 491–502, doi:10.1190/1.1443786.

Mariotti, G. (1978), Caratteri sismici dell'attività vulcanica di Stromboli., Master thesis, Univ. Florence, 256 pp.

Martinelli, B. (1991), Fluidinduzierte Mechanismen für die Entstehung von vulkanischen Tremorsignalen, 1976, Diss. ETH. Zürich, 164 pp.

Mattia, M., M. Rossi, F. Guglielmino, M. Aloisi, and Y. Bock (2004), The shallow plumbing system of Stromboli islands as imaged from 1 Hz instantaneous GPS position., *Geophys. Res. Lett.*, *31*, 4 pp., doi:10.1029/2004GL021281.

McGreger, A. D., and J. M. Lees (2004), Vent discrimination at Stromboli volcano, Italy., *J. Volcanol. Geotherm. Res.*, *137*, 169–185.

McNutt, S. (2002), Volcano seismology and monitoring for eruptions, *In: Lee, W. H. K., and Kanamori, H. and Jennings, P. C. and Kisslinger, C. (eds.): International Handbook of Earthquake and Engineering Seismology*, elsevier, New York.

McNutt, S. R. (1986), Observations and analysis of B-type earthquakes, explosions and volcanic tremor at Pavlof volcano, Alaska., *Bull. Seismol. Soc. Am.*, *76*, 153–175.

Melbourne, T., and F. H. Webb (2003), Slow, but not quite silent., *Science*, *300*, 1886–1887.

Minakami, T. (1960), Fundamental research for predicting volcanic eruptions (1) - earthquakes and crustal deformations originating from volcanic activities., *Bull. Earthquakes Res. Inst. Tokyo Univ.*, *38*, 497–544.

Mohnen, J.-U., and R. Schick (1996), The spatial amplitude distribution of volcanic tremor at Stromboli volcano (Italy), *Ann. Geofis.*, *39*(2), 361–375.

Mori, J., H. Patia, C. McKee, P. Itikarai, P. Lowenstein, P. De Saint Ours, and B. Talai (1989), Seismicity associated with eruptive activity at Langila Volcano, Papua New Guinea., *J. Volcano. Geoth. Res.*, *38*, 243–255.

Morrissey, M., B. Zimanowski, K. Wohletz, and R. Büttner (2000), Phreatomagmatic fragmentation, *In: Sigurdsson, H. (ed.): Encyclopedia of volcanoes*, pp. 431–445, academic Press.

Nakano, M., and H. Kumagai (2005), Correction to waveform inversion of volcano seismic signals assuming possible source geometries., *Geophys. Res. Lett.*, *32*, 4 pp., doi:10.1019/2005GL024848.

Napoleone, G., M. Ripepe, G. Saccorotti, L. Totti, and A. Albianelli (1993), The strombolian activity presently recorded at Stromboli., *Acta Volcanol.*, *3*, 163–171.

Nappi, G. (1976), Recent activity at Stromboli., *Nature*, *261*, 119–120.

Neuberg, J., R. Luckett, M. Ripepe, and T. Braun (1994), Highlights from a seismic broadband array on Stromboli volcano., *Geophys. Res. Lett.*, *21*, 749–752.

Ntepe, N., and J. Dorel (1990), Observations of seismic volcanic signals at Stromboli volcano (Italy)., *J. Volcanol. Geotherm. Res.*, *43*, 235–251.

Obara, K. (2002), Non-volcanic deep tremor associated with subduction in Southwest Japan., *Science*, *31*, 1679–1681.

Ohminato, T., B. A. Chouet, P. B. Dawson, and S. Kedar (1998), Waveform inversion of very long-period impulsive signals associated with magmatic injection beneath Kilauea Volcano, Hawaii., *J. Geophys. Res.*, *103*, 23,839–23,862.

Okada, H., Y. Nishimura, H. Miyamachi, H. Mori, and K. Ishihara (1990), Geophysical significance of the 1988-1989 explosive eruptions of M. Tokachi, Hokkaido, Japan., *Bull. Volcanol. Soc. Japan*, *35*, 175–203.

Oliver, J., and M. Ewing (1957), Microseisms in the 11 to 18 second period range., *Bull. Seism. Soc. Am.*, *47*, 111–127.

Omer, G. C. (1950), Volcanic tremor, *Bull. Seis. Soc. Am.*, *40*, 175–194.

Omori, F. (1911), Report on the observation of pulsatory oscillations in japan, *Bull. Imp. Earthquake Inv. Comm.*, *5*(1), 109–137.

Ozawa, S., M. Murakami, and T. Tada (2001), Time-dependent inversion study of the slow thrust event in the Nankai through subduction zone, Southwestern Japan, *J. Geophys. Res.*, *106*, 787–802.

Press, F., and J. Oliver (1955), Model study of air-coupled surface waves., *J. Acoust. Soc. Am.*, *27*, 43–46.

PVOT - Pinatubo Volcano Observatory Team (1991), Lessons from a major eruption: Mt. Pinatubo, Philippines, *EOS*, *72*, 545–555.

Ripepe, M. (1996), Evidence for gas influence on volcanic seismic signals recorded at Stromboli, *J. Volcanol. Geotherm. R.*, *70*, 221–233, doi:10.1016/0377-0273(95)00057-7.

Ripepe, M., and T. Braun (1994), Air-wave phases in strombolian explosion-quake seismograms: a possible indicator for the magma level?, *Acta Vulcanologica*, *5*, 201–206.

Ripepe, M., M. Rossi, and G. Saccorotti (1993), Image processing of explosive activity at Stromboli., *J. Volcanol. Geotherm. Res.*, *54*, 335–351.

Ripepe, M., P. Poggi, T. Braun, and E. Gordeev (1996), The short-period tremor recorded at Stromboli volcano., *Geophys. Res. Lett.*, *23*(2), 181–184.

Ripepe, M., S. Cililberto, and M. Della Schiava (2001), Time constrained for modelling source dynamics of volcanic explosions at Stromboli, *J. Geophys. Res.*, *160*, 8713–8727.

Riuscetti, M., R. Schick, and D. Seidl (1981), Spectral parameters of volcanic tremors at Etna: a model for hydraulic origin, *Bull. Volcanol.*, *44*, 43–56.

Romagnoli, C., P. Kokellar, P. L. Rossi, and A. Sodi (1993), The submarine extension of Sciara del Fuoco feature (Stromboli Island): morphologic characterization., *Acta Vulcanol.*, *3*, 91–98.

Rosi, M., A. Bertagnini, A. J. L. Harris, L. Pioli, M. Pistolesi, and M. Ripepe (2006), A case history of paroxysmal explosion at Stromboli: timing and dynamics of the April 5, 2003 event., *Earth Planet. Sc. Lett.*, *243*, 594–606.

Saccorotti, G., B. Chouet, M. Martini, and R. Scarpa (1998), Bayesian statistics applied to the location of the source of explosions at Stromboli volcano, Italy, *Bull. Seis. Soc. Am.*, *88*(5), 1099–1111.

Sassa, K. (1935), Volcanic micro-tremors and eruption-earthquakes., *Mem. Coll. Sci. Univ. Kyoto A.*, *18*, 255–293.

Schick, R. (1981), Source mechanism of volcanic earthquakes., *Bull. Volcanol.*, *44*, 491–497.

Schick, R. (1988), Volcanic tremor-source mechanisms and correlation with eruptive activity., *Natural Hazard*, *1*, 125–144.

Schick, R., and W. Müller (1988), Volcanic activity and eruption sequences at Stromboli during 1983-1984, *In: Chi-Yu King & R. Scarpa (eds.): Modelling of Volcanic Processes*, pp. 120–139.

Schick, R., and M. Riuscetti (1973), An analysis of volcanic tremor at South Italian volcanoes., *Zeitschr f. Geophys.*, *39*, 247–262.

Seidl, D., and M. Hellweg (1991), Volcanic tremor recordings: polarization analysis., *In: Schick and Mugiono (eds.): Volcanic Tremor and Magma flow*, pp. 31–46.

Seidl, D., R. Schick, and M. Riuscetti (1981), Volcanic tremors at Etna: a model of hydraulic origin, *Bull. Volcanol.*, *44*, 43–56.

Seyfried, R., and A. Freundt (2000), Experiments on conduit flow and eruption behavior of basaltic volcanic eruptions, *J. Geophys. Res.*, *105*, 23,727–23,740.

Sieberg, A. (1914), *Einfuehrung in die Erdbeben - und Vulkankunde Sueditaliens.*, Verlag G. Fischer, Jena, 226 pp.

Silver, P. G., and T. H. Jordan (1982), Optimal estimation of scalar seismic moment., *Geophys. J. R. Astron. Soc.*, *70*, 755–787.

Steinberg, G. S., and A. S. Steinberg (1975), On possible causes of volcanic tremor., *J. Geophys. Res.*, *80*, 1600–1604.

Strobach, K. (1964), Entstehung und Charakter der Mikroseismik als Resultantschwingung zahlreicher seismischer Oszillatoren., *Zeitschr. f. Geophysik*, *30*, 192–208.

Strobach, K. (1965), Origin and properties of microseisms from the standpoint of oscillator theory., *Bull. Seis. Soc. Am.*, *55*(2), 365–390.

Tessmer, E., and D. Kosloff (1994), 3-D elastic modelling with surface topography by a Chebychev spectral method., *Geophysics*, *59*, 464–473.

Tessmer, E., D. Kosloff, and A. Behle (1992), Elastic wave propagation simulation in the presence of surface topography., *Geophys. J. Int.*, *108*, 621–632.

Tinti, S., A. Maramai, A. Armigliato, L. Graziani, A. Manucci, G. Pagnoni, and F. Zaniboli (2006), Observation of physical effects from tsunamis of December 30, 2002 at Stromboli volcano, Southern Italy., *Bull. Volcanol.*, *65*, 450–461.

Udias (1999), *Principles of Seismology*, Cambridge University Press, Cambridge.

Vergniolle, S., and G. Brandeis (1994), Origin of the sound generated by strombolian explosions., *Geophys. Res. Lett.*, *21*, 1959–1962.

Vila, J., J. Marti, R. Ortiz, A. Garcia, and E. M. Correig (1992), Volcanic tremor at Deception Island (South Shetland Islands, Antarctica), *J. Volcanol. Geotherm. Res.*, *53*, 89–102.

Wassermann, J. (1997), Locating the sources of volcanic explosions and volcanic tremor at Stromboli volcano (Italy) using beam-forming on diffraction hyperboloids., *Phys. Earth Planet. Int.*, *104*(1-3), 271–281.

Weill, A., G. Brandeis, S. Vergniolle, F. Baudin, J. Bilbille, J. Fèvre, B. Piron, and X. Hill (1992), Acoustic sounder measurements of the vertical velocity of volcanic jets at Stromboli volcano., *Geophys. Res. Lett.*, *19*, 2357–2360.

Wenzel, H.-G. (1994), ETGTAB - a computer program for the computation of earth tides, *Tech. rep.*, Geodätisches Institut, Universität Karlsruhe, Englerstr. 7, D-76128 Karlsruhe.

Wohletz, K. H. (1986), Explosive magma - water interactions: Thermodynamics, explosion mechanisms, and field studies., *Bull. Volcanol.*, *48*, 245–264.

Yuan, A. T. E., S. R. McNutt, and D. Harlow (1984), Seismicity and eruptive activity at Fuego volcano, Guatemala: february 1975 - january 1977., *J. Volcanol. Geotherm. Res.*, *21*, 277–296.

Zimanowski, B. (1998), Phreatomagmatic explosions, *In: Freundt, A. and Rosi, M. (eds.): Developments in Volcanology: From Magma to Tephra*, pp. 25–54.

Zimanowski, B., V. Lorenz, and F. G. (1986), Experiments on phreatomagmatic explosions with silicate and carbonatitic melts., *J. Volcanol. Geotherm. Res.*, *30*, 149–153.

Zimanowski, B., G. Fröhlich, and V. Lorenz (1991), Quantitative experiments on phreatomagmatic explosions., *J. Volcanol. Geotherm. Res.*, *48*, 341–358.

Zimanowski, B., G. Fröhlich, and V. Lorenz (1995), Experiments on vapour explosions by interaction of water with silicate melts., *Nucl. Eng. Des.*, *155*, 335–343.

Zimanowski, B., R. Büttner, V. Lorenz, and H. H.G. (1997), Fragmentation of basaltic melt in the course of explosive volcanism, *J. Geophys. Res.*, *102*, 803–814.

Appendix A

Curriculum vitae

PERSÖNLICHE DATEN

Name:	Thomas Braun
Geburtsdatum:	2. Mai 1963
Geburtsort:	Frankfurt am Main
Eltern:	Rosemarie Braun, geb. Mann, Sekretärin
	Hermann Braun, Beamter
Staatsangehörigkeit:	deutsch
Familienstand:	verheiratet mit Kirsten Wimmer
Kinder:	Joshua (1993), Laura (1995), Vivien (2000)

AUSBILDUNG

1969 – 1973	Grundschule, Frankfurt
1973 – 1982	Helmholtz-Gymnasium, Frankfurt mit Abschluss Abitur
1982 – 1990	Studium der Geophysik an der Johann-Wolfgang-Goethe-Universität, Frankfurt. Titel der Diplomarbeit: *Untersuchung einer Anomalie im tieferen Untergrund des Vogelsberges mit Hilfe teleseismischer Laufzeitresiduen*
April 1990	Diplom in Geophysik; Abschlussnote: *sehr gut*
seit Juni 1999	Promotionsstudium der Geowissenschaften an der Julius-Maximilians-Universität Würzburg

BERUFSWEG

1990 – 1991	wissenschaftlicher Angestellter am Institut für Geophysik der Johann -Wolfgang-Goethe-Universität, Frankfurt
1991 – 1995	Stipendiat der Landesgraduiertenförderung Baden-Württemberg, Auslandsaufenthalt am *Dipartimento di Scienze della Terra* der Universität Florenz (Italien) in Zusammenarbeit mit dem Institut für Geophysik der Universität Stuttgart
1993 – 1997	wissenschaftlicher Mitarbeiter am *Osservatorio Ximeniano* in Florenz (Italien)
1997 – 1999	Stipendiat am *Istituto Nazionale di Geofisica* in Rom
1999 – 2001	wissenschaftlicher Angestellter am *Istituto Nazionale di Geofisica* in Rom
seit 2001	wissenschaftlicher Angestellter am *Istituto Nazionale di Geofisica e Vulcanologia* in Arezzo und Leiter des dortigen Seismologischen Observatoriums